Faculty of Biology, Chemistry and
Earth Sciences
Micrometeorology Group
Professor Dr. Christoph Thomas

Master thesis

Simulating an extreme heat event in a mid-sized city in Europe with Large Eddy Simulation: investigating the impact of spatial resolution and validation with an observation network

Eva Späte

student of Global Change Ecology
matriculation number: 1699810
eva.spaete@uni-bayreuth.de

Supervisors:

Prof. Dr. Christoph Thomas
Dr. Wolfgang Babel

Bayreuth, March 31, 2023

Abstract

Urban citizens are known to be exposed to higher temperatures than rural citizens making urban citizens particularly vulnerable to extreme heat events. Large Eddy Simulation (LES) models can simulate micrometeorological heat transport and mixing processes by directly resolving large-scale turbulence. These models can also be used to evaluate urban development strategies aiming at mitigating the adverse effects of heat waves in cities by analyzing their influence on the urban microclimate. Despite their use in formulating recommendations for city planning, these models are often not validated with observed meteorological data. We here present results from conducting a model-observation comparison for a mid-sized city in Germany. Model simulations were computed with the LES model PALM-4U run at two different isotropic spatial resolutions (Δx,y,z = 5 and 20 m) and evaluated against observations from a network of microweather stations for a heat wave in 2019 reaching maximum near-surface air temperatures of 37 °C. During daytime, differences between observed and modeled near-surface air temperatures were small (–3.8 to 1.1 K, mean = 0.9 K), but much larger during nighttime and the early morning transition. The latter findings can be explained by an overestimated modeled ground heat flux resupplying too much energy to the surface. This offset the radiative cooling and led to overestimated modeled air temperatures of up to +9 K (mean = 5.3 K). For wind speeds, the results showed that in areas where the actual urban surface structure was reproduced well by the model resolution, differences between observed and modeled wind speeds were lower. Our findings indicate that a spatial resolution smaller than the height of most buildings produce more accurate model results for wind speeds. That the simulation was run without the spin-up mechanism of PALM-4U constitutes an uncertainty factor for the modeled output. We therefore recommend including a spin-up period for future runs to ensure a sufficient initialization of the surface layers' temperature and moisture content. To improve the simulation output, we further recommend reviewing the thermal diffusivity values of the surface layer, adjusting the boundary input of incoming shortwave radiation, and increasing the fixed water temperature in the model setup. To further explore model-observation differences and the impact of spatial resolution, we recommend analyzing the modeled advection which was out of the scope of this thesis.

Zusammenfassung

Die Bevölkerung ist in Städten höheren Temperaturen ausgesetzt als auf dem Land, weswegen sie besonders durch extreme Hitzeereignisse gefährdet sind. Large Eddy Simulation (LES) Modelle können mikrometeorologischen Wärmetransport und Mischungsprozesse simulieren, indem sie großräumige Turbulenzen direkt auflösen. Diese Modelle können auch zur Bewertung von Stadtentwicklungsstrategien verwendet werden, die darauf abzielen, die negativen Auswirkungen von Hitzewellen in Städten zu mildern, indem ihr Einfluss auf das urbane Mikroklima untersucht wird. Trotz ihrer Anwendung bei der Formulierung von Empfehlungen für die Stadtplanung werden diese Modelle oft nicht mit beobachteten meteorologischen Daten validiert. Wir stellen hier Ergebnisse aus dem Vergleich von modellierten und beobachteten meteorologischen Daten für eine mittelgroße Stadt in Deutschland vor. Die Modellsimulation wurde mit dem LES-Modell PALM-4U bei zwei verschiedenen isotropen räumlichen Auflösungen (Δx,y,z = 5 und 20 m) berechnet und mit Beobachtungen eines Netzwerks von Wetterstationen für eine Hitzewelle im Jahr 2019 mit Temperaturen von bis zu 37 ℃ validiert. Während die Unterschiede zwischen den beobachteten und den modellierten oberflächennahen Lufttemperaturen tagsüber gering waren (–3.8 bis 1.1 K, Mittelwert = 0.9 K), waren die Unterschiede in der Nacht und am frühen Morgen wesentlich größer. Letztere Ergebnisse lassen sich durch einen überschätzten modellierten Bodenwärmestrom erklären, der zu viel Energie an die Oberfläche transportiert. Dies führte zum Ausgleich der Strahlungskühlung und zu überschätzten modellierten Lufttemperaturen von bis zu +9 K (Mittelwert = 5.3 K). Die Ergebnisse für Windgeschwindigkeiten zeigten, dass in Gebieten, in denen die tatsächliche urbane Oberflächenstrukturierung durch die Modellauflösung gut wiedergegeben wurde, die Unterschiede zwischen beobachteten und modellierten Windgeschwindigkeiten geringer waren. Unsere Ergebnisse deuten darauf hin, dass mit einer räumliche Auflösung, die kleiner ist als die Höhe der meisten Gebäude, genauere Modellergebnisse für Windgeschwindigkeiten erzielt werden können. Dass die Simulation ohne den Spin-up-Mechanismus von PALM-4U berechnet wurde, stellt einen Unsicherheitsfaktor für die modellierten Ergebnisse dar. Daher empfehlen wir, zukünftige Simulationen mit eine Vorlaufzeit (spin-up period) zu berechnen, um eine hinreichende Initialisierung der Temperatur und des Feuchtigkeitsgehalts der Oberflächenschichten zu erreichen. Um die Simulationsergebnisse weiter zu verbessern, empfehlen wir außerdem, die Werte für die Temperaturleitfähigkeit der Oberflächenschicht anzupassen, die Modell-Inputdaten für die eingehende kurzwellige Strahlung anzupassen und

die Wassertemperatur in den Modelleinstellungen zu erhöhen. Um die Unterschiede zwischen Modell und Beobachtung und die Auswirkungen der räumlichen Auflösung weiter zu untersuchen, empfehlen wir, die modellierte Advektion zu analysieren, welche in dieser Arbeit nicht untersucht wurde.

Contents

List of figures

List of tables

List of symbols

symbol	description	unit
a	thermal diffusivity	10^{-6} m^2 s^{-1}
C	heat capacity	10^6 J m^{-3} K^{-1}
C_p	specific heat of air at constant pressure	J kg^{-1} K^{-1}
e	water vapor pressure	Pa
e_s	saturation water vapor pressure	Pa
F	flux density	W m^{-2}
i	index	
k	thermal conductivity	W m^{-1} K^{-1}
$K\downarrow$	incoming shortwave radiation	W m^{-2}
$K\uparrow$	outgoing shortwave radiation	W m^{-2}
$L\downarrow$	incoming longwave radiation	W m^{-2}
$L\uparrow$	outgoing longwave radiation	W m^{-2}
m	water vapor mixing ratio	g kg^{-1}
M	wind speed	m s^{-1}
p	air pressure	Pa
p_0	surface air pressure	Pa
q	specific humidity	g kg^{-1}
Q_S^*	net all-wave radiation flux	W m^{-2}
Q_E	latent heat flux	W m^{-2}
Q_F	anthropogenic heat flux	W m^{-2}
Q_G	ground heat flux	W m^{-2}
Q_H	sensible heat flux	W m^{-2}
R_d	gas constant for dry air	J kg^{-1} K^{-1}
R_v	gas constant of water vapor	J kg^{-1} K^{-1}
R^2	coefficient of determination	
rh	relative humidity	%
S_0	solar constant	W m^{-2}
t	time	s

symbol	description	unit
$T_{°C}$	temperature	°C
T_K	temperature	K
TKE	turbulent kinetic energy	$m^2\,s^{-2}$
u	east-west wind velocity component	$m\,s^{-1}$
u_i	wind velocity components ($u_1 = u$, $u_2 = v$, $u_3 = w$)	$m\,s^{-1}$
v	north-south wind velocity component	$m\,s^{-1}$
X	meteorological element	
w	vertical wind velocity component	$m\,s^{-1}$
x	horizontal east-west distance	m
x	grid cell location in the model domain (east-west direction)	
x_i	distance ($x_1 = x$, $x_2 = y$, $x_3 = z$)	m
y	horizontal north-south distance	m
y	grid cell location in the model domain (north-south direction)	
z	height / vertical distance	m
z	grid cell location in the model domain (vertical direction)	
z_{IBL}	internal boundary layer height	m
Δ	difference / change	
ΔQ_A	net heat advection	$W\,m^{-2}$
ΔQ_S	net heat storage	$W\,m^{-2}$
ϵ	emissivity	
μ_{BH}	mean building height	m
ϕ	scalar quantity	
ρ	air density	$kg\,m^{-3}$
ρ_v	absolute humidity	$kg\,m^{-3}$
σ_{SB}	Stefan-Boltzmann constant	$W\,m^{-2}\,K^{-4}$
σ_{BH}	standard deviation of the building height	m
θ	potential temperature	K

superscripts	description
$\overline{}$	time average / temporal mean
$'$	instantaneous deviation from mean

List of abbreviations

ABL	atmospheric boundary layer
AMSL	above mean sea level
BH	building height
BHH	building height heterogeneity
CEST	Central European Summer Time
CET	Central European Time
CFD	Computational Fluid Dynamics
COSMO-DE2	Consortium for small-scale modeling
DWD	Deutscher Wetter Dienst (German meteorological service)
EBG	Ecological Botanical Garden
ISL	inertial sublayer
IQR	interquartile range
LES	Large Eddy Simulation
MiSKOR	Minderung städtischer Klima- und Ozonrisiken
ML	mixed layer
MM station	meteorological measurement station
mod	modeled
MT	morning transition
NA	not available
NetCDF	Network Common Data Form
NBL	nocturnal boundary layer
obs	observed
RANS	Reynolds-average Navier Stokes
RSL	roughness sublayer
SCH	surface cover heterogeneity
SL	surface layer
TKE	turbulent kinetic energy in $m^2\,s^{-2}$
UBL	urban boundary layer

UCL	urban canopy layer
UHI	urban heat island
UTM	Universal Transverse Mercator
UTM E	UTM East
UTM W	UTM West

1 Introduction

Climate change greatly impacts the meteorological conditions in cities. A phenomenon called the urban heat island (UHI) describes that air temperatures in cities are higher than in surrounding rural areas (Geiger et al., 2009). Howard (1833) was the first to discover the UHI for the city of London (Mills, 2008), which since has been documented in several cities worldwide (Brandsma & Wolters, 2012; Jauregui, 1997; Robaa, 2003). Warming of up to 12 °C has been recorded (Hung et al., 2006). Climate change poses an additional driver for high temperatures in urban areas. Since 1850, the global surface temperature has increased by more than 1 °C and it is expected to increase further (IPCC, 2021). As global temperature is increasing, so are temperatures in urban areas (Stone et al., 2012). Furthermore, climate change causes heatwaves to occur with an increased frequency and intensity (IPCC, 2021). Studies have shown that, next to provoking extreme temperatures, heatwaves enhance the intensity of UHI even further because of the cities‘ higher heat storage capacity and heat conductivity compared to rural areas (Li & Bou-Zeid, 2013; Zhao et al., 2018). Although urban areas cover only 3 % of the world's land surface (Liu et al., 2014), more than 50 % of the global population lives in cites. Until 2050 this share is expected to increase to 68% (UN DESA, 2019). Increasing urbanization amplifies the UHI as urban area increases in density and size (Li et al., 2017). Rising numbers of urban citizens also entail that increasingly more people are exposed to high urban temperatures and subsequent health risks. At high air temperatures, the human body's thermoregulatory capacity fails to cool the body to a safe level. Especially older people are vulnerable to high temperatures as their ability to move themselves to cooler locations is reduced and their body's physiological mechanisms to cope with high temperatures are impaired (Meade et al., 2020). To protect human well-being today and in the future, it is crucial to better understand how to mitigate those temperature extremes in cities. UHI research is mostly focused on large cities (Graham, 1993; Jauregui, 1997; Kim & Baik, 2002; Robaa, 2003) while studies on small and mid-sized cities are rare. Nevertheless, smaller urban areas are as well impacted by UHI and human discomfort (Cardoso et al., 2017). In Germany, 30 % of the population lives in mid-sized cities between 20,000 and 100,000 citizens (BBSR, 2017). Therefore, it is crucial to extend the knowledge on meteorological processes and urban effects in mid-sized cities.

Numerical simulations of meteorological processes can be used to simulate urban development strategies aiming at mitigating the adverse effects of heat waves in cities. Since the

1990s, Computational Fluid Dynamics (CFD) models are popular in urban climate research (Toparlar et al., 2017), which can solve the Navier-Stokes equations, i.e., equations describing the motion of fluids, at fine scales, e.g., meters, over domains of a few hundred meters. A distinction of CFD models can be made between Reynolds-average Navier Stokes (RANS) and Large Eddy Simulation (LES) models. While RANS models parameterize all eddies and resolve only averaged motions, LES models directly resolve large-scale turbulence and only parameterize the smaller eddies. LES models are therefore known to require larger computing power than RANS models but also deliver more accurate results (Martilli & Santiago, 2009). Despite their use in formulating recommendations for city planning, these models are often not validated with observed meteorological data. Toparlar et al. (2017) found that many modeling studies of urban climate are not validated, despite validation being essential for the meaningfulness of modeling results. The authors explain this by a lack of required measurement data which is necessary for validation.

For the city of Bayreuth, Germany, this kind of in-situ measurement data is available. Up to 17 measurement stations at structurally different urban sites were implemented within the scope of the MiSKOR project (*Mi*nderung *s*tädtischer *K*lima- und *O*zon*r*isiken) to measure several meteorological elements between September 1, 2018, and September 30, 2020 (MiSKOR, 2021). This high availability of data points makes the city of Bayreuth an ideal location for thorough validation of meteorological simulations with observed data. The research project MiSKOR analyzed the meteorological conditions in Bayreuth aiming to extend the knowledge on meteorological processes and urban effects in mid-sized cities. Therefore, the city of Bayreuth in Bavaria, Germany, served as an example of a mid-sized city. Sungur (2021) set up the LES model PALM-4U to run a realistic replication of Bayreuth's cityscape. The author analyzed the impact of two urban development scenarios on different meteorological elements compared to a base run. In one scenario, the urban water surfaces were doubled in size, and for the other scenario, the vegetated surfaces were turned into bare soil simulating drought stress. The study period covered a 26-hours interval during a heat wave in July 2019 (2019-07-25 12:00 to 2019-07-26 14:00 CEST), which included the hottest day in 2019. This period was chosen because of the enhanced human health risks caused by high temperatures and the consequential need to mitigate such extreme heat events in cities through urban development strategies. Sungur (2021) concludes that the modeled base run can replicate the biophysical conditions in a mid-sized city. This assessment was reached by comparing the model output against the mean of 15 meteorological measurement stations within the study area. However, an explicit validation of the model has yet to be performed. Concerning the scenario runs, the results indicated that drought stress induces higher air temperatures within the city. The scenario of doubling the water surfaces did not show a clear effect on air temperature. The author concludes that a finer grid scale of 5 m or less would be necessary to observe small-scale effects due to urban infrastructure modification. An inner domain with a spatial resolution of 5 m covering 65 km^2, which is approximately the area of Bayreuth's city borders, was intended but not executed due to high computing power needs.

This thesis extends the work of Sungur's (2021). The PALM-4U simulation was validated with data from an observation network, and a model-model comparison of two different isotropic spatial resolutions (Δx,y,z = 5 und 20 m) was conducted. The aim of this thesis is to identify possible enhancements to the PALM-4U application. Thus, the results of future simulations can be improved and more tangible recommendations for urban development strategies can be formulated. This thesis is structured as follows: First, concepts and meteorological theories are explained in Chapter 2 as a background rationale for the proposed objectives and hypotheses in Chapter 3. The data and methods applied are presented in Chapter 4 and the results are displayed in Chapter 5. Finally, the findings of this thesis are discussed in Chapter 6 and Chapter 7 concludes this thesis.

2 Theory and state-of-the-art research

This chapter outlines the fundamental characteristics of urban meteorology necessary to understand this thesis' objectives, results, and discussion. The urban landscape is characterized by an exceptional heterogeneity in surfac structure and materials, which causes varying radiative, thermal, and moisture properties. Common urban surface materials are characterized by low albedo, high emissivity, and high thermal diffusivity values (Gartland, 2011). Furthermore, urban surfaces are typically impermeable while vegetated areas occupy a small fraction of the landscape. The urban surface structure is shaped by buildings of different sizes and shapes which form narrow alleys, wide street canyons or squares, causing a high surface roughness. In comparison to rural areas, vertical surfaces are common in urban areas. Additionally, cities are places of concentrated human actions like heating or cooling of buildings, traffic and pollution from industrial areas (Gartland, 2011). The influence of these distinct urban properties on the meteorological conditions within urban areas is explained below.

2.1 The urban boundary layer

The bottom layer of the troposphere above the Earth's surface which is influenced by the roughness, thermal mixing, and moisture conditions at the surface is called the atmospheric boundary layer (ABL). The lowest 10 % of the ABL is called the surface layer (SL) where flows are mainly influenced by friction with the Earth's surface. Within the mixed layer (ML), the top 90 % of the ABL, atmospheric properties are uniformly mixed by thermal and shear-driven turbulence creating typical vertical profiles of wind speed, potential temperature, and water vapor. The thermal turbulence comes to a hold by a capping inversion at the top of the ABL. Above the ABL is the free atmosphere, which is not impacted by the surface. During the night, when the surfaces cool, a stable nocturnal boundary layer (NBL) forms above the ground. The residual layer above the NBL contains the atmospheric properties, moisture, and pollution from the mixed layer of the previous day (Oke et al., 2017).

Above cities, the ABL is strongly influenced by the distinct urban surface properties. This part of the ABL is called the urban boundary layer (UBL) (Fig. 1). During the day, urban areas typically experience stronger heating than rural areas which causes stronger turbulent thermals and a deeper mixed layer compared to a rural mixed layer. The urban surface layer consists of the inertial sublayer (ISL) and the roughness sublayer (RSL). The RSL stretches from the surface to up to three times the height of the buildings. This layer is characterized by a substantial flow deflection due to the roughness of the urban elements. Part of the RSL is the urban canopy layer (UCL) which covers the area from ground level to the mean building height. The meteorological conditions in this layer are spatially highly variable because at each location it is influenced by the present heterogeneous surface properties and building geometry. Above the RSL lies the inertial sublayer which is less influenced by the surface roughness. During the night when the urban surfaces cool, the UBL shrinks (Fig. 1b). Cities are typically warmer during the night than rural areas leading to a comparably stronger mixed atmosphere in cities (Oke et al., 2017).

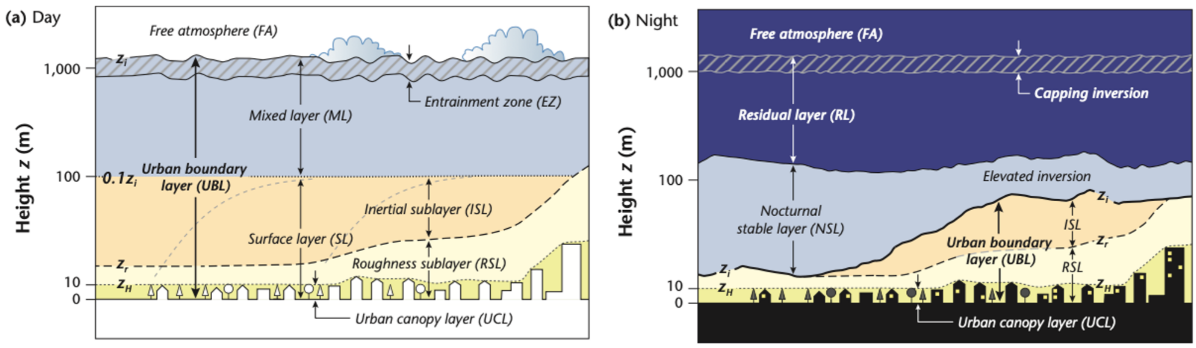

Figure 1: Sketch of the urban boundary layer structure (a) during the day and (b) during the night. The height scale on the y axis is logarithmic except near the surface. The figures were reprinted from Oke (2017, p. 31).

2.2 Radiation balance at urban surfaces

The main energy transfer occurs at the Earth's surface. The three fundamental types of energy transfer are radiation, convection, and conduction. The latter is the slowest form and is caused by transporting kinetic energy between adjacent molecules via vibration. Convection is the transport of energy via motion in a fluid. The fastest form of energy transfer is radiation which delivers almost all energy in the climate system. The surface radiation budged equation describes the balance between incoming and outgoing radiation (Eq. 1). The net all-wave radiation Q_S^* (W m^{-2}) at the Earth's surface is the sum of incoming $K\downarrow$ (W m^{-2}) and outgoing shortwave radiation $K\uparrow$ (W m^{-2}), and incoming $L\downarrow$ (W m^{-2}) and outgoing longwave radiation $L\uparrow$ (W m^{-2}) (Stull, 2017):

$$Q_S^* = K\downarrow + K\uparrow + L\downarrow + L\uparrow \ \ (\mathrm{W\,m^{-2}}). \tag{1}$$

Within cities with their heterogeneous surface structure and distinctive atmospheric properties, the components of the radiation budget equation vary spatially. Incoming shortwave radiation reaching the surface can be blocked by buildings casting shadows or can be diminished by air pollution which reflects or absorbs radiation. Many common urban pavement and roofing materials have low albedo values, resulting in high absorption rates of shortwave radiation in cities. The absorbed radiation is transformed into heat causing high surface temperatures in cities (Gartland, 2011). According to the Stefan-Boltzmann law, the emission of longwave radiation $L\uparrow$ (W m^{-2}) at a surface depends on its emissivity and its temperature (Oke et al., 2017):

$$L\uparrow = \epsilon \cdot \sigma_{SB} \cdot T_K^4 \;\; (\mathrm{W\,m^{-2}}). \tag{2}$$

The emissivity ϵ (dimensionless) describes the radiative efficiency between ϵ = 0 and ϵ = 1, where the latter indicates a perfect emitter. The Stefan-Boltzmann constant σ_{SB} is defined as σ_{SB} = 5.67 · 10^{-8} W m^{-2} K^{-4}, and T_K is the absolute temperature of the surface in Kelvin. According to Equation 2, the typical high temperatures of urban surfaces cause high emission of longwave radiation into the atmosphere.

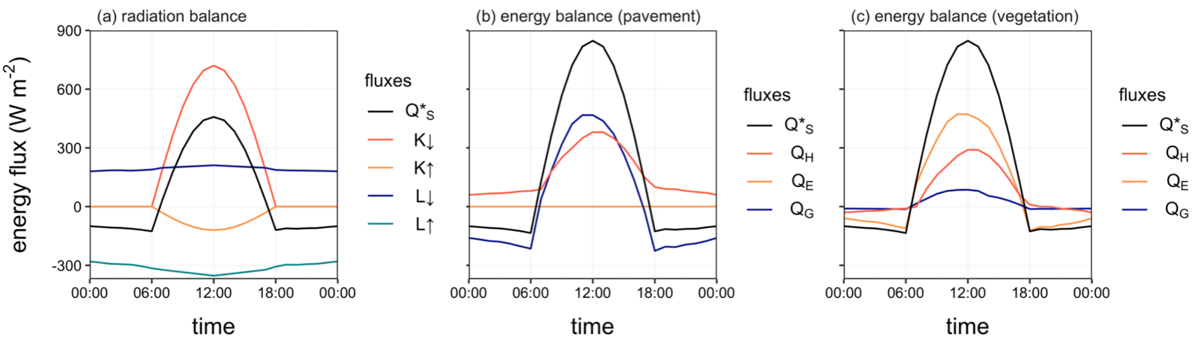

Figure 2: Schematic diurnal course of the (a) radiation balance, (b) energy balance above dry pavement, and (c) energy balance above vegetation cover at the Earth's surface during cloudless conditions. Q_S^* in W m^{-2} (black line) is the net all-wave radiation in all panels. The radiation fluxes in (a) are the incoming shortwave radiation $K\downarrow$ in W m^{-2} (red line), the outgoing shortwave radiation $K\uparrow$ in W m^{-2} (yellow line), the incoming longwave radiation in W m^{-2} $L\downarrow$ (blue line), and the outgoing longwave radiation in $L\uparrow$ W m^{-2} (green line). The energy fluxes in (b) and (c) are the sensible heat flux Q_H in W m^{-2} (red lines), the latent heat flux Q_E in W m^{-2} (yellow lines), and the ground heat flux Q_G in W m^{-2} (blue lines). Course and magnitude of the fluxes were adapted from Oke (2017, p. 152 & 186).

Shortwave incoming radiation $K\downarrow$ is zero during the night and increases after sunrise, peaking at noon, following a nearly sinusoidal curve (Stull, 2017) (Fig. 2a). With no incoming solar radiation, the outgoing shortwave radiation $K\uparrow$ is zero as well, while during the day it follows the course of the incoming radiation but at lower values. The ratio of outgoing shortwave radiation to incoming shortwave radiation is the albedo. Both longwave radiation fluxes $L\uparrow$ and $L\downarrow$ are different from zero during the whole diurnal cycle as they depend on the emissivity and absolute temperature of the emitting surface, which are both greater than zero. The surface temperature increases during the day as incoming shortwave radiation is absorbed leading to a larger outgoing longwave radiation flux during the day. During the night, the surface cools because it absorbs no shortwave radiation but still emits longwave radiation.

2.3 Energy balance at urban surfaces

The net all-wave radiation Q_S^* of Equation 1 represents the available energy at the Earth's surface which is divided into turbulent and molecular energy fluxes. The energy balance at the Earth's surface reads as follows (Oke et al., 2017):

$$-Q_S^* = Q_H + Q_E + Q_G + \Delta Q_S \ \ (\mathrm{W\,m^{-2}}), \tag{3}$$

where Q_H (W m^{-2}), Q_E (W m^{-2}), and Q_G (W m^{-2}) are the sensible, latent, and ground heat fluxes, respectively, and ΔQ_S (W m^{-2}) is the change in heat storage. The magnitude of the single components during the course of a day can vary greatly with the surface cover type, the available energy, and available moisture content (Fig. 2b,c). All fluxes are larger in magnitude during the day than at night as they are driven by the available net all-wave radiation Q_S^*, which provides a large energy surplus during the day and a smaller energy deficit during the night. The turbulent sensible heat flux Q_H is driven by the surface-air temperature differences and transports energy in form of heat from the surface into the atmosphere. At vegetated areas, the sensible heat flux is usually smaller because the available energy is converted into the latent heat flux Q_E if sufficient moisture is available. When water evaporates, latent heat gets hidden in the presence of water vapor. The latent heat flux transports energy without changing the air temperature. Therefore, air temperatures are typically lower above vegetated and water areas. Only when water vapor condenses again heat is released. The ground heat flux Q_G transfers sensible heat from the surface into the ground by conduction. How easily heat is conducted through the ground is described by the thermal diffusivity a (10^{-6} m^2 s^{-1}) (Oke et al., 2017):

$$a = \frac{k}{C} \ \ (10^{-6}\,\mathrm{m^2\,s^{-1}}), \tag{4}$$

which is the ratio of thermal conductivity k ($\mathrm{W\,m^{-1}\,K^{-1}}$), the ability of a material to conduct heat, to heat capacity C ($10^6\,\mathrm{J\,m^{-3}\,K^{-1}}$), the ability of a material to store heat. Materials of high thermal diffusivity, e.g., concrete, allow for fast temperature changes of the material, while materials with low thermal diffusivity, e.g., water, cause temperature changes to occur slower and only at the top layers of the material (Oke et al., 2017).

In urban areas, the components of the surface energy balance (Eq. 3) are altered. At dry urban areas, the latent heat flux can equal zero and all available energy is converted into the sensible and the ground heat flux (Fig. 2b). The turbulent sensible heat flux is typically strong and might also stay positive during the night, constantly transporting energy in form of heat from the surface into the atmosphere as seen in Figure 2b. This is caused by a comparably large heat storing capacity of urban materials and a subsequent increase in ΔQ_S during the day. During the night, the stored heat is then slowly released (Oke et al., 2017).

The energy balance at the urban surface can be extended by the anthropogenic heat flux Q_F ($\mathrm{W\,m^{-2}}$) and the net energy change due to advection ΔQ_A ($\mathrm{W\,m^{-2}}$) (Oke et al., 2017):

$$-Q_S^* + Q_F = Q_H + Q_E + Q_G + \Delta Q_S + \Delta Q_A \quad (\mathrm{W\,m^{-2}}). \tag{5}$$

The anthropogenic heat flux Q_F increases the available energy in cities on the left-hand side of Equation 5. It is caused by human activities such as combusting fuels, heating and cooling buildings, conversion of energy for cooking or lightning, and transportation (Oke et al., 2017). ΔQ_A is the net energy change due to advection, which is the transport of heat, mass, or momentum by the mean wind. Under the assumption of a fairly uniform building density, advection is often neglected. However, in areas of variable land use and three-dimensional surface structure, as it is the case for cities, horizontal exchanges must be included (Oke, 1987; Oke et al., 2017).

2.4 Air flow and turbulence in urban areas

Wind, the flow of air in the atmosphere, is generated in high altitudes by the pressure-gradient force from areas of high air pressure to areas of low air pressure. Other forces (e.g., Coriolis force, centrifugal force) influence wind speed and direction but do not create wind itself. The undisturbed air flow above the ABL, called the geostrophic wind, results from a balance between the Coriolis force and the pressure-gradient force. While affecting the general wind direction and speed, the geostrophic wind is slowed down and deflected by surface roughness elements and their geometry in the urban roughness sublayer (Oke et al., 2017; Stull, 2017). At the surface, the wind speed is zero and it increases with height in a roughly logarithmic profile (Fig. 3) (Stull, 2017):

$$M = \frac{u_*}{\kappa} \cdot \ln\left(\frac{z}{z_0}\right) \quad (\mathrm{m\,s^{-1}}), \tag{6}$$

with mean wind speed M (m s^{-1}), and friction velocity u_* (m s^{-1}), which is a measure of the drag force per unit surface area of the ground. κ is the von Kármán constant with κ = 0.4 (dimensionless), z (m) is the height, and z_0 (m) is the aerodynamic roughness length which quantifies the surface roughness (Stull, 2017).

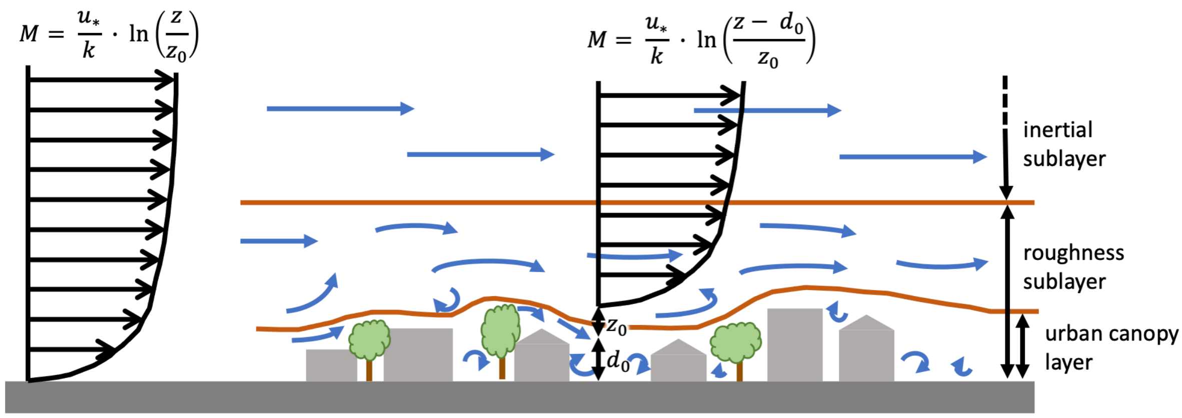

Figure 3: Sketch of the urban wind flow. The black arrows display the logarithmic wind profiles, and the blue arrows show the air flow in an urban area. The extents of the different sections of the urban boundary layer are indicated at the right. The figure was adapted from Palme & Salvati (2021, p. 199).

While the vertical profile of mean wind speed is well defined in the literature, the profile within cities remains an open question (Cheng & Castro, 2002; Palme & Salvati, 2021). Above the urban canopy layer, the mean wind speed M is described as (Oke et al., 2017):

$$M = \frac{u_*}{\kappa} \cdot \ln\left(\frac{z - d_0}{z_0}\right) \quad (\mathrm{m\,s^{-1}}). \tag{7}$$

Equation 7 extents Equation 6 by the displacement height d_0 (m) which describes the height of the effective surface below which the wind speed would be zero following the vertical wind profile (Cheng & Castro, 2002; Palme & Salvati, 2021).

Wind speed M (m s^{-1}) can be expressed with a 3D-vector $\vec{u} = (u_1, u_2, u_3)$ with two horizontal directions u_1 = u and u_2 = v and the vertical direction u_3 = w (Stull, 2017):

$$M = \sqrt{u_1^2 + u_2^2 + u_3^2} \ \ (\mathrm{m\,s^{-1}}). \tag{8}$$

According to the Reynold's Decomposition, the velocity for each direction is composed of the mean wind (indicated with an overbar) and the turbulent wind (indicated with a prime) (Oke et al., 2017):

$$u_i = \overline{u_i} + u_i' \ \ (\mathrm{m\,s^{-1}}), \tag{9}$$

with $i \in \{1, 2, 3\}$. The mean wind $\overline{u_i}$ (m s^{-1}) is the average of the wind measurements over time while the turbulent wind is the velocity deviation from the mean wind ($u_i' = u_i - \overline{u_i}$). Turbulence is described by eddies of different sizes and time scales usually smaller than 30 min, which rotate at a different velocity than the mean wind. The mean of the turbulence is zero by definition ($\overline{u_i'} = 0$). Turbulence can be produced either by thermal or mechanical processes. Thermal turbulence is typically caused by unevenly heated surfaces. The comparable warmer air above stronger heated surfaces is less dense and therefore rises, producing vertical thermal turbulence (compare turbulent heat fluxes in Chapter 2.3). Mechanical turbulence is caused by friction between air and the ground or obstacles, e.g., buildings, as a result of shear, which is defined as the velocity differences. If sufficiently large, the produced forces initiate eddies, which move slower or faster than the mean wind (Oke et al., 2017).

The intensity of turbulence is measured with the turbulent kinetic energy (TKE) per unit mass which is defined as half the sum of the variances of the velocity deviations (Oke et al., 2017):

$$TKE = 0.5 \cdot \left[\overline{(u')^2} + \overline{(v')^2} + \overline{(w')^2}\right] \ \ (\mathrm{m^2\,s^{-2}}). \tag{10}$$

u, v, and w are the wind velocity components in east-west, north-south, and the vertical direction, respectively. High intensities of turbulence cause the mixing of air of higher levels with air of lower levels and can therefore reduce vertical temperature or humidity gradients. Further, turbulence can cause faster eddies originating from higher levels, where wind is usually faster, to be carried downwards which are then experienced as gusts in lower levels (Oke et al., 2017).

2.5 Effects on meteorological elements

The specific processes described above have an effect on the meteorological conditions in urban areas, which are described by meteorological elements. This thesis has three elements in its focus: air temperature, atmospheric humidity, and wind speed. They were selected based on their importance for the human thermal comfort (Djongyang et al., 2010).

Below, the drivers for these three meteorological elements in urban areas are set out, using the Eulerian framework. The Eulerian framework describes an air parcel at a fixed position relative to the ground. The meteorological conditions within this air parcel change as flows pass through the parcel over time (Stull, 2017). This framework was chosen because, as meteorological measurement stations take measurements at a fixed location, it can be pictured that the measurement station's instruments are within an Eulerian air parcel. Further, the output of the PALM-4U model is given in grid boxes, each representing the meteorological conditions at a fixed position over time.

2.5.1 Air temperature

The Eulerian heat-budget equation describes the temperature change of an air parcel over time (Stull, 2017):

$$\frac{\Delta T_K}{\Delta t} = -\frac{1}{\rho \cdot C_p}\left[\frac{\Delta F_{x_1}}{\Delta x_1} + \frac{\Delta F_{x_2}}{\Delta x_2} + \frac{\Delta F_{x_3}}{\Delta x_3}\right] + \frac{\Delta S_0}{C_p \cdot \Delta t} \quad (\mathrm{K\,s^{-1}}), \tag{11}$$

with temperature T_K (K), time t (s), air density ρ (kg m^{-3}), specific heat of air at constant pressure C_p (J kg^{-1} K^{-1}), flux divergence ΔF (W m^{-2}) in the directions x_1 = x, x_2 = y, and x_3 = z (m), and additional internal heat sources $\frac{\Delta S_0}{C_p \cdot \Delta t}$ (K s^{-1}). The latter concerns temperature changes through direct release of anthropogenic or latent heat within the air parcel (Oke et al., 2017; Stull, 2017). The magnitude of anthropogenic heat release is expected to be small in mid-sized developed areas with no extensive use of air conditioning during the summer, as it is the case for this thesis' study area. Furthermore, the release of latent heat did not occur during the study period as the relative humidity in the study area stayed below 100 %. Thus, the term $\frac{\Delta S_0}{C_p \cdot \Delta t}$ can be neglected.

The flux divergence $\frac{\Delta F_{x_i}}{\Delta x_i}$ (W m^{-3}) with $i \in \{1, 2, 3\}$ can be caused by four processes: radiation, turbulence, advection, and conduction:

$$\frac{\Delta F_{x_i}}{\Delta x_i} = \left.\frac{\Delta F_{x_i}}{\Delta x_i}\right|_{rad} + \left.\frac{\Delta F_{x_i}}{\Delta x_i}\right|_{turb} + \left.\frac{\Delta F_{x_i}}{\Delta x_i}\right|_{adv} + \left.\frac{\Delta F_{x_i}}{\Delta x_i}\right|_{cond} \quad (\mathrm{W\,m^{-3}}). \tag{12}$$

Radiation implies shortwave radiation and longwave radiation. On the one hand, clear air is mostly unaffected by shortwave radiation. Thus, the amount of shortwave radiation entering the air parcel equals the amount of shortwave radiation exiting the parcel, resulting in a neglectable shortwave radiation flux divergence. On the other hand, air absorbs longwave radiation and re-radiates it according to the Stefan-Boltzmann law (Eq. 2). Typically, the horizontal longwave radiation flux divergence is negligible assuming weak horizontal temperature gradients. Vertically however, temperature decreases with height causing a vertical longwave radiation divergence $\frac{\Delta F_{z\,rad}}{\Delta z}$. The temperature of an air parcel can further change through turbulent mixing of heat. As for the radiation flux divergence, the turbulent flux divergence in horizontal directions is approximately zero due to negligible horizontal temperature gradients. Therefore, only the vertical turbulent heat flux divergence $\frac{\Delta F_{z\,turb}(\theta)}{\Delta z}$ with potential temperature θ has an influence. Next, air temperature can change through heat advection whereas vertical advection can be neglected (Stull, 2017), leaving horizontal advection ($i \in \{1, 2\}$):

$$\frac{\Delta F_{x_i\,adv}}{\Delta x_i} = u_i \cdot \frac{\Delta T_K}{\Delta x_i} \quad (\mathrm{W\,m^{-3}}), \tag{13}$$

where x_i (m) with $i \in \{1, 2\}$ are the horizontal directions and $u_1 = u$ and $u_2 = v$ ($\mathrm{m\,s^{-1}}$) are the respective mean wind speeds. $\frac{\Delta T_K}{\Delta x_i}$ ($\mathrm{K\,m^{-1}}$) are the temperature gradients in the respective directions. Finally, temperature change of an air parcel via molecular conduction can be neglected because molecular conductivity for air is small (Stull, 2017). By inserting the discussed flux-gradient approximations into the heat-budget equation (Eq. 11), the change of air temperature over time of a volumetric air parcel can be described by the following equation:

$$\left.\frac{\Delta T_K}{\Delta t}\right|_{x,y,z} = -\frac{1}{\rho \cdot C_p} \cdot \left[\underbrace{\frac{\Delta F_{zrad}}{\Delta z}}_{\text{radiation}} + \underbrace{\frac{\Delta F_{zturb}(\theta)}{\Delta z}}_{\text{turbulence}} + \underbrace{\left(u \cdot \frac{\Delta T_K}{\Delta x} + v \cdot \frac{\Delta T_K}{\Delta y}\right)}_{\text{advection}}\right] \quad (\mathrm{K\,s^{-1}}). \tag{14}$$

The processes causing temperature change in an air parcel described by this equation are visualized graphically in Figure 4a. As indicated, negative flux gradients cause a positive temperature change. If the in-going flux in x_i (m) direction exceeds the outgoing flux of the air parcel, the term.

$$\frac{\Delta F_{x_i}}{\Delta x_i} = \frac{\Delta F_{x_i\, eastside} - \Delta F_{x_i\, westside}}{\Delta x_{i\, eastside} - \Delta x_{i\, westside}} \quad (\mathrm{W\,m^{-3}}) \tag{15}$$

is negative for $x_{i\, westside} < x_{i\, eastside}$ (Stull, 2017).

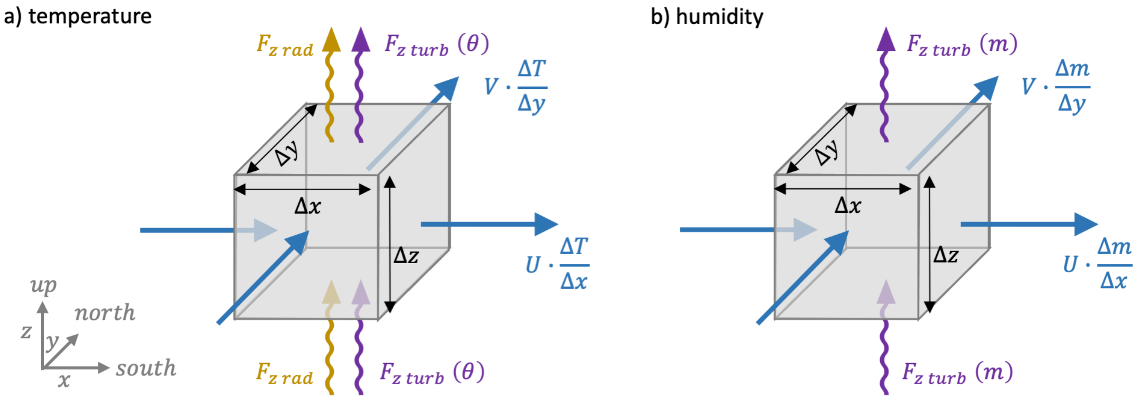

Figure 4: Sketch of the drivers of (a) temperature and (b) humidity changes within an Eulerian air parcel. The yellow arrows represent radiation, purple arrows represent turbulent fluxes, and blue arrows represent advection. θ is the potential temperature, and m is the water vapor mixing ratio. The figures were conceptualized after Oke et al. (2017) and Stull (2017).

Next to air temperature, potential temperature was analyzed in this thesis. Potential temperature θ is a conserved meteorological element which stays constant for adiabatic processes, i.e., no heat or mass transport between the air parcel and its environment. It is calculated with air temperature T_K (K), air pressure p (Pa), and surface pressure p_0 (Pa):

$$\theta = T_K \cdot \left(\frac{p_0}{p}\right)^{R_d/C_p} \quad (\mathrm{K}), \tag{16}$$

where R_d (J kg^{-1} K^{-1}) is the gas constant for dry air, C_p (J kg^{-1} K^{-1}) is the specific heat of air at constant pressure, and R_d/C_p = 0.286 (Stull, 2017).

2.5.2 Atmospheric humidity

The atmospheric humidity of a volumetric air parcel changes also over time due to flux divergences as it was seen for air temperature in Equation 11. Molecular conduction, vertical advection, and horizontal turbulence can also be neglected for humidity for the same reasons as explained above for temperature. Further, humidity changes due to precipitation can be neglected if no precipitation occurs like it was the case during the study period of this thesis. The change of total water content of the air inside the parcel over time, neglecting precipitation, is therefore defined as

$$\frac{\Delta m}{\Delta t} = -\frac{1}{\rho}\left[\underbrace{\left(u \cdot \frac{\Delta m}{\Delta x} + v \cdot \frac{\Delta m}{\Delta y}\right)}_{\text{advection}} + \underbrace{\frac{\Delta F_{zturb}(r)}{\Delta z}}_{\text{turbulence}}\right] \quad (\mathrm{g\,kg^{-1}\,s^{-1}}), \tag{17}$$

with water vapor mixing ratio m ($\mathrm{g\,kg^{-1}}$), time t (s), air density ρ ($\mathrm{kg\,m^{-3}}$), horizontal advection caused by wind components u ($\mathrm{m\,s^{-1}}$) and v ($\mathrm{m\,s^{-1}}$), the turbulent total-water flux $F_{zturb}(m)$, and direction differences Δx, Δy, and Δz, respectively. According to Equation 17, the water content of an air parcel changes due to advection or turbulence. If the in-going turbulent flux is larger than the outgoing flux, the water content increases. It increases also if the water content entering the parcel through advection is larger than the water content leaving the parcel. Figure 4b describes the processes of Equation 17 graphically.

The two humidity types analyzed in this thesis are specific humidity q and water vapor mixing ratio m. Both meteorological elements are conservative and do not change with changing pressure or temperature. Specific humidity q ($\mathrm{g\,kg^{-1}}$) is mass water vapor per mass moist air. It is calculated with air pressure p (Pa) and water vapor pressure e (Pa) (Foken, 2017):

$$q = 0.622 \cdot \frac{e}{p - 0.378e}\,\frac{1}{1000} \quad (\mathrm{g\,kg^{-1}}). \tag{18}$$

The water vapor mixing ratio m ($\mathrm{g\,kg^{-1}}$) is mass water vapor per mass dry air and is calculated with air pressure p (Pa) and water vapor pressure e (Pa) (Foken, 2017):

$$m = 0.622 \cdot \frac{e}{p - e}\,\frac{1}{1000} \quad (\mathrm{g\,kg^{-1}}). \tag{19}$$

2.5.3 Wind speed

Within the roughness sublayer, wind speed is heavily influenced by roughness elements such as buildings and vegetation, causing air flow to be spatially heterogeneous and three-dimensional (Palme & Salvati, 2021). Compared to rural areas, the mean wind speed is decreased by friction while turbulence in cities is increased. Due to the high surface roughness, mechanical turbulence dominates in the RSL (Oke et al., 2017). Depending on the exact location and wind direction, wind speed can vary greatly in urban areas. Directly behind buildings, wind speeds can be calm as the building serves as shelter (Oke et al., 2017). On the contrary, wind speeds can be high near the base of tall buildings which can deflect down high wind speeds from above (Stull, 2017). Concluding, wind speed at a certain location within the urban canopy layer depends highly on the assembling of the surrounding roughness elements (Fig. 3).

3 Objectives and hypotheses

This master's thesis extends the work of Sungur (2021), who run a meteorological simulation in the city of Bayreuth, Germany, during a heat wave in 2019 (2019-07-25 12:00 to 2019-07-26 14:00 CEST) using the LES model PALM-4U. Building on Sungur (2021), her simulation was re-run including a nested inner domain at a 5 m spatial resolution. The aim of this thesis is to disclose possible enhancements to the PALM-4U application and therefore improving results of future simulations. The objectives of this thesis can be summarized as follows:

1. Validating the PALM-4U model of the city of Bayreuth with observed meteorological data by conducting a model-observation comparison and
2. analyzing the relevance of the model's spatial resolution by conducting a model-model comparison of two different spatial resolutions (5 and 20 m).

The validation and analysis focus on the meteorological elements air temperature, atmospheric humidity, and wind speed to represent three crucial elements for the human well-being (Oke et al., 2017). Based on the current state of knowledge, this thesis aims to support the following hypotheses:

Objective 1

1. The differences between modeled and observed air temperature and between modeled and observed specific humidity are larger during the day than during the night.

   Rationale: The influencing factors of air temperature, such as radiation, conduction, and convection, are larger and more complex during the day than during the night (compare Chapter 2.2 and 2.3, and Fig. 2). Nighttime air temperature is mostly influenced by the thermal capacities of the buildings which are expected to be simulated more precisely than the pronounced fluxes during the day. Likewise, evaporation, the driving factor of atmospheric humidity, is larger and more distinctive during the day, as it is fueled by solar radiation. Varying water availability due to high urban surface heterogeneity causes large variability in evaporation and therefore spatially variable urban humidity especially during the day. Due to the larger day-time fluxes and complexity, a higher error possibility in the model is assumed and therefore it is hypothesized that the nighttime values are more precise.

2. The differences between modeled and observed wind speeds are larger in areas of high building-height heterogeneity than in less variable areas.

   Rationale: Urban wind speeds can vary greatly spatially because of the heterogeneous urban structure and varying building heights (compare Chapter 2.4 and 2.5.3). The wind speed at a specific location can drastically differ to the wind speed a few meters away e.g., around a building corner. Areas of large building height heterogeneity are expected to be less well represented in the model causing larger model-observation differences.

3. Across air temperature, atmospheric humidity, and wind speed, the differences between the modeled and observed values are larger for the 20 m than the 5 m spatial resolution.

   Rationale: Urban climate is spatially highly variable due to the heterogeneous urban structure. The heterogeneity influences radiation, convection, and turbulence in the urban boundary layer, which in turn influences the meteorological elements. The heterogeneity of urban surface structure and materials is responsible for a variability of the meteorological elements. A finer spatial resolution of processes within the model is therefore expected to result in modeled data which is in closer agreement with the observations than for a coarser spatial resolution.

<u>Objective 2</u>

4. The differences between the data modeled at the 5 m and the data modeled at the 20 m spatial resolution are larger for areas with greater building height and surface cover heterogeneity than at more homogeneous areas.

   Rationale: Cities are characterized by their heterogeneity such as varying building height and differences in building materials which influence the urban meteorological conditions. Thus, especially in areas of high heterogeneity, cities experience meteorological conditions which are spatially highly variable. It is hypothesized that a finer spatial resolution of the urban structure and meteorological processes in these areas will create results that deviate from a coarser spatial resolution. Contrary, in more homogeneous areas where the variability of meteorological conditions is lower the change in spatial resolution is expected to have a lower impact.

5. The differences between the data modeled at the 5 m and the data modeled at the 20 m spatial resolution are larger in the urban roughness sublayer than at higher layers of the urban boundary layer.

Rationale: In the urban roughness sublayer, the influence of urban structures on meteorological conditions is largest and it declines with altitude. In higher layers, more mixing occurs and therefore horizontally more uniform conditions exist. The effect of decreasing the model's spatial resolution from 20 to 5 m should therefore be largest at the roughness sublayer and diminish with height.

4 Methods and materials

This chapter describes the data and methods used in this thesis. It starts with an overview of the study area and the study period followed by a description of the observed data derived from measurement stations. Thereafter, the PALM-4U model used for the simulations is described. Finally, the data processing for the individual objectives and hypotheses is explained.

4.1 Study area and study period

The study area was the city of Bayreuth in northern Bavaria, Germany (Fig. 5), a medium-sized town covering 67 km^2 with nearly 75,000 citizens (LfStat, 2019). Surrounded by several hills, the city of Bayreuth is located in a wide valley. The main water feature of Bayreuth is the river Rotmain which crosses the city from east to west. The root domain of this study extended over 218 km^2 and covered the whole city of Bayreuth and its surrounding (Fig. A.1 in the appendix). The root domain served as an adjustment zone for the LES nesting of the inner domain. The inner domain was nested inside the root domain, and covered a 2×2.4 km site including the city center of Bayreuth (Fig. 5c). This inner domain is referred to as the *study area* in the following. The study area covered the whole inner city, the city park Hofgarten, the lake Röhrensee in the south, the green finger at the Mistel river in the west, the industrial area Spinnerei in the north and another green finger at the Rotmain river in the west. 24 % of the study area was covered by buildings, 46 % by vegetation (mainly short grass), 29 % by pavement (mainly asphalt/concrete and stone), and 1 % of the surface was covered with water. The lowest elevation point of the study area was located the Rotmain river basin in the northwest corner of the study area at 328.4 m above mean sea level (AMSL). The highest elevation was found at 358.2 m AMSL in St. Georgen in the northeast of the study area. High buildings were mainly located in the city center, west of the city center and at the industrial area Spinnerei. The tallest building was the city hall with 52 m. Other tall buildings were a residential building west of the Röhrensee (45 m) and the Graf Münster school east of the Hofgarten (40 m) which were both located on elevated parts of the city.

The study period covered a 26-hour interval between 2019-07-25 12:00 to 2019-07-26 14:00 CEST. In the following, *day one* refers to the time steps on 2019-07-25 and *day two* to the time steps on 2019-07-26. The study period was characterized by an anticyclonic Fennoscandian high leading to clear-sky conditions. The meteorological measurement station in the Ecological Botanical Garden (EBG) of Bayreuth, which serves as a reference measurement station according to international standards since 1994 (MiSKOR, 2021), measured a maximum daytime air temperature of 36.9 °C during the study period. This was the hottest air temperature measured at this station in 2019. The minimum nighttime air temperature was 14.8 °C and no precipitation was measured during the study period. The average annual air temperature in Bayreuth is 8.6 °C (1991 – 2020) and the average annual precipitation is 718 mm (1991 – 2020) (Thomas, 2023).

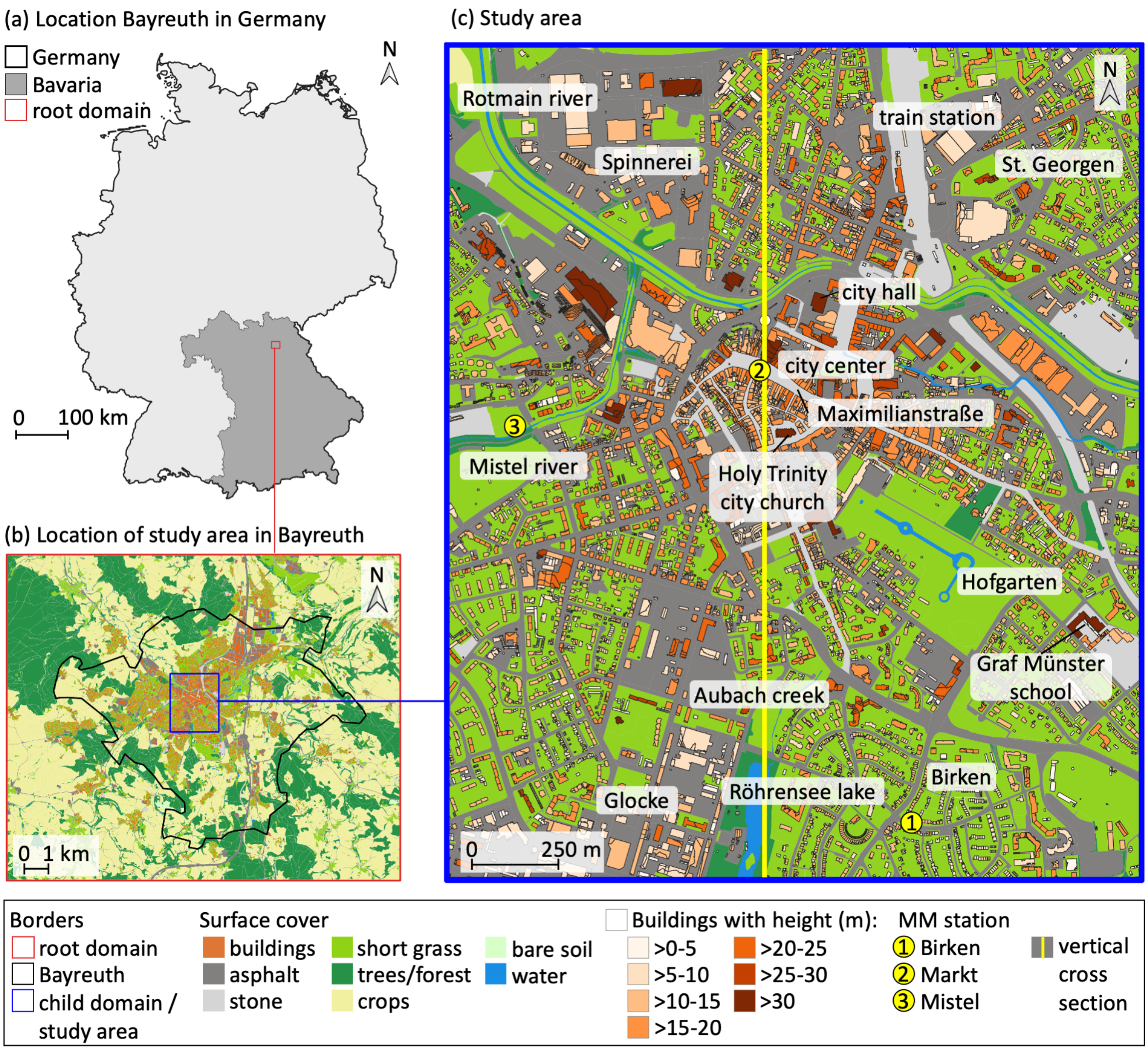

Figure 5: Geographic locations of (a) the city of Bayreuth within Germany, (b) the study area (32 5534206 N 683744 E to 32 5536606 N 685744 E) within Bayreuth, and (c) features within the study area. Map (c) shows the location of the meteorological measurement (MM) stations of the MiSKOR project as of July 2019 in yellow. Relevant areas and locations mentioned in the text are indicated. The vertical yellow line displays the location of the vertical cross section. Shapefiles originate from ©GeoBasis-DE/BKG (2022) ©Bayerische Vermessungsverwaltung (2018).

4.2 Observations

As part of the MiSKOR project, a network of measurement stations was set up in July 2018 (MiSKOR, 2021). The stations were installed at up to 17 locations throughout the city of Bayreuth representing different structural urban areas varying in terms of sealing density, building height, and proximity to main traffic axes as well as to parks and water areas. The all-in-one measurement stations were firmly installed micro weather stations (ATMOS-41, Metergroup U.S.A.) with data logger (EM60G), mounted in 3.5 m height above the surface. They measured the following meteorological elements with a temporal resolution of 5 min averaging intervals: absolute humidity (%), air pressure (hPa), air temperature (°C), incoming shortwave radiation ($\mathrm{W\,m^{-2}}$), precipitation (mm), wind direction (°), and wind speed ($\mathrm{m\,s^{-1}}$). The instruments were meteorologically examined by Thomas et al. (2019) and thereafter updated by the manufacturer (MiSKOR, 2021). Before installation, a side-by-side comparison of all instruments was conducted over 17 days, detecting a mean average deviation of 0.1 Kelvin for air temperature, and 0.06 $\mathrm{m\,s^{-1}}$ for wind speed.

For this study, the measurement stations Birken, Markt, and Mistel were selected and are introduced in Table 1. These three measurement stations were located in distinctively different urban structures at which dissimilar meteorological conditions were observed according to a multi-resolution decomposition by Spies (2019). Figure 6 and 7 show the distribution of building height and surface cover surrounding the measurement stations, respectively. The Birken station represented a lightly built-up area in the south of Bayreuth with spread out family homes smaller than 20 m and surrounded by vegetated areas. Representing a densely built-up area with mostly sealed surfaces, the Markt station was located on the main shopping street Maximilianstraße in the city center of Bayreuth. The surrounding of this measurement station was further characterized with a high building height heterogeneity and tall buildings of up to 52 m. The Mistel station was located close to the Mistel river in the west of Bayreuth and was surrounded with vegetation and only a few close-by buildings.

Table 1: Overview of the measurement stations Birken, Markt, and Mistel. The table shows their UTM coordinates and the height (m AMSL), a photo of the installation of the measurement instruments, and the surface cover and building height in a square with a side length of 260 m centered at the measurement station. Photos by J. Luers. Shapefiles originate from ©GeoBasis-DE/BKG (2022).

	Birken	Markt	Mistel
Location			
coordinates (UTM)	32 5534370.96 N 685082.62 E	32 5535666.41 N 684645.31 E	32 5535503.86 N 683943.30 E
height (AMSL)	340.51 m	342.60 m	351.81 m
Installation of measurement devices (photo)			
			
Surface cover and building height surrounding the stations (square with 260 m inradius)			
buildings with height (m) >0-5 >5-10 >10-15 >15-20 >20-25 >25-30 >30 asphalt cobblestone short grass trees/forest water station cd border	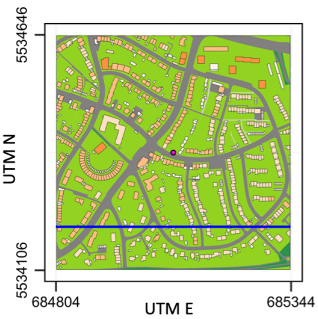	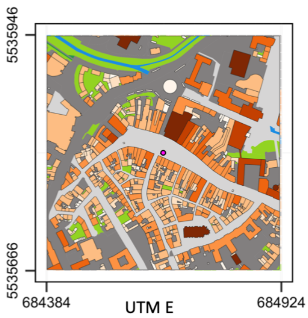	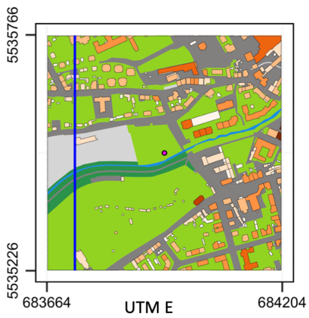

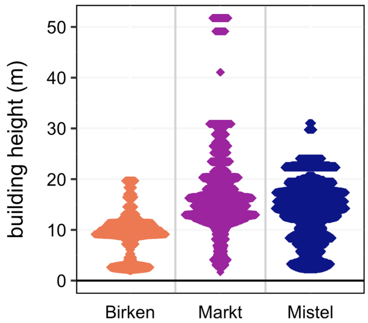

Figure 6: Height (m) distribution of the buildings surrounding each measurement station in a square with a side length of 260 m centered at the measurement station.

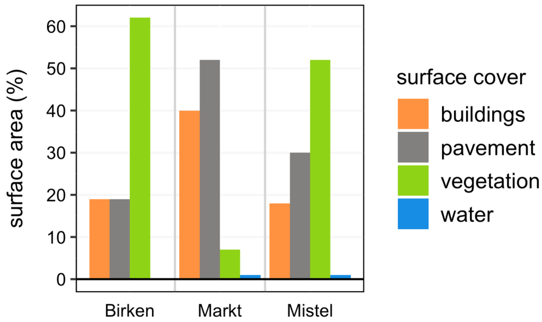

Figure 7: Share of surface cover types surrounding each measurement station in a square with a side length of 260 m centered at the measurement station (in %).

The size of the area, which was considered for describing the measurement stations' surroundings, was chosen based on the internal boundary layer height. An internal boundary layer (IBL) forms when a wind profile is formed above a surface, which is influenced by the surface properties like temperature and roughness. The wind profile is shifted downwind by the mean wind speed creating a layer of discontinuity called the internal boundary layer (Fig. 8) (Foken, 2017). This means that the exchange of energy and matter at a certain height is affected by the surface properties of the downwind area.

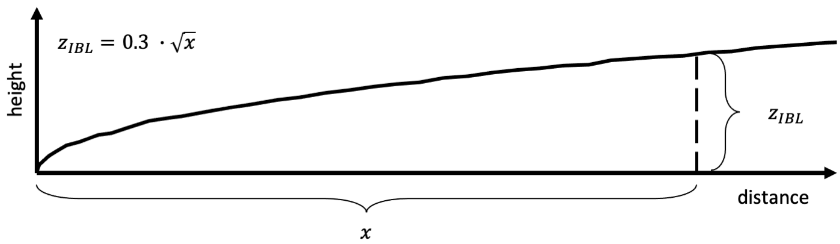

Figure 8: Sketch of the internal boundary layer and the relation between internal boundary layer height z_{IBL} (m) and distance x (m) after Raabe and Foken (2003).

This internal boundary layer height z_{IBL} (m), below which the processes are affected by the wind profile resulting from the surface property at distance x (m), can be described by the following equation (Raabe & Foken, 2003):

$$z_{IBL} = 0.3 \cdot \sqrt{x} \ \ (\mathrm{m}). \tag{20}$$

The internal boundary layer height at the measurement location was equivalent to the installation height of the measurement devices with z_{IBL} = 3.5 m. Therefore, the distance x within which the atmospheric processes at the measurement station were influenced by the surface cover was

$$x = \left(\frac{z_{IBL}}{0.3}\right)^2 = 136 \text{ m}. \tag{21}$$

To cover the relevant area within a radius of x = 136 m, while also matching the squared grid shape of the PALM-4U model, a square with a side length of 260 m was chosen for describing the measurement stations' surroundings (Fig. 9). The shortest distance from the measurement location to the edges of the square was 130 m, and the longest distance to the corners of the square was 183 m. This area matched the PALM-4U grid well as it had the dimension of 13 × 13 m 20 m grid cells with the center grid cell covering the measurement station.

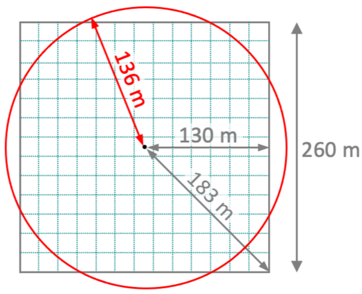

Figure 9: Sketch of the square with a side length of 260 m centered at a measurement station (black dot) at which the atmospheric processes at the measurement location are approximately influenced by the surrounding surface cover. The red circle marks the distance of the internal boundary layer in every direction according to Equation 20 with a boundary layer height of z_{IBL} = 3.5 m at the measurement station. The dotted green squares are the 20 m grid cells in this area with the center grid cell covering the measurement station.

4.3 Simulation with the LES model PALM-4U

The modeled data was simulated with the PALM model system 6.0 which was developed at the Institute of Meteorology and Climatology of the Leibniz University Hannover, Germany, to study atmospheric and oceanic boundary layers (Maronga et al., 2020; Maronga et al., 2015). As an LES model, the PALM model solves the Navier-Stokes equations while separating large-scale turbulences which are directly resolved from small-scale turbulences which are fully parameterized. Besides the core components, the PALM model offers the urban application module PALM-4U which is used to research atmospheric flows, temperature, and humidity in urban environments (Maronga et al., 2019). The setup of the model for this study followed the approach of Sungur (2021) who set up the PALM-4U model for the city of Bayreuth and its surrounding by designing a static and dynamic driver build from data of the local land surveying office and a steering parameter namelist. The original root domain of Sungur (2021) was kept with an area of 218 km^2 (Fig. A.1 in the appendix) and at a spatial resolution of 20 m. However, only the output within the study area as described above was considered in this study. To carry forward Sungur's (2021) thesis, an inner child domain with the spatial resolution of 5 m was successfully nested within the root domain. A smaller extent of the child domain was chosen as originally intended by Sungur, which reduced the computational effort. The child domain in this study spread over 4.8 km^2 and covered exactly the extent of the study area described above. For the detailed setup of the model please refer to Sungur (2021). The final modeled study area is shown in Figure 10. The domain covers an area of 2000 $\times$ 2400 $\times$ 300 m which equals 100 $\times$ 120 $\times$ 15 20 m grid cells and 400 $\times$ 480 $\times$ 60 5 m grid cells, respectively.

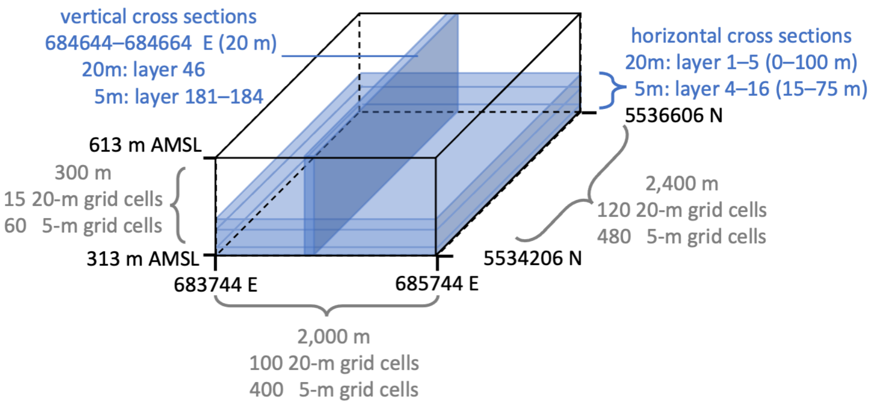

Figure 10: 3D sketch of the model domain. The blue layers represent the selected vertical and horizontal cross sections.

For the synoptic forcing conditions during the study period, the output of the high-resolution regional model Consortium for small-scale modeling (COSMO-DE2), which was designed by the German meteorological service (DWD), was taken as dynamic driver input. The hourly COSMO-DE2 model output included velocity components, specific humidity, potential temperature, perturbation pressure, soil moisture, and soil temperature. As source for the incoming shortwave radiation served data from the measurement station in the EBG in Bayreuth. The data of these meteorological elements were integrated as initial boundary data at the borders of the root domain.

Topography and building information for the model stemmed from a rasterized and voxelized file with a layout matching the modeled domain and grid size in the x and y direction. The height information was given in meters AMSL. The bottom domain bound was set by PALM-4U at the lowest topography height entered (313 m AMSL). The topography and building shapes were approximated by PALM-4U to the nearest grid cell to fit the grid. Therefore, grid cells in PALM-4U were either 100 % fluid or 100 % obstacle. While obstacle grid cells were excluded from calculations, the output quantities of fluid grid cells were defined according to an Arakawa staggered C-grid depicted in Figure 11. Scalar quantities were specified at the center of each grid cell while velocity components were defined at the center of the respective edges of the grid cell (Maronga et al., 2015). If a fluid grid cell was located next to an obstacle gird cell like a building, the velocity components at this side were zero.

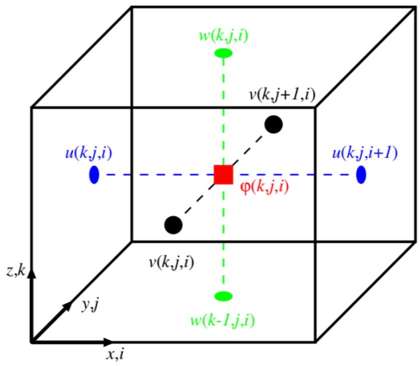

Figure 11: Sketch of the Arakawa staggered C-grid. The grid cells in x, y, and z direction are indicated by the indices i, j, and k, respectively. Scalar quantities (φ) are specified at the center of each grid cell while velocity components (u, v, w) are defined at the center of the respective edges of the grid cell. The figure is reprinted from Maronga et al. (2015, Fig. 2, p. 2519).

The output of the model consisted of several NetCDF files containing data of the selected quantities in a 20 m as well as a 5 m spatial resolution. Table 2 lists all relevant output quantities for this study including the respective output files. The output files most relevant for this thesis contained horizontal or vertical two-dimensional temporally averaged data by 10 min of each grid cell of the selected cross sections (DATA_2D). The 26-hour simulation resulted in 156 time steps for the whole study period. The selected cross sections in z direction were layers 1 to 5 for the 20 m spatial resolution and layers 4 to 15 for the 5 m spatial resolution (Fig. 10). In the y direction, layer 382 for the 20 m spatial resolution and layers 180–183 for the 5 m spatial resolution were selected. Thereby, a vertical 20 m wide transection from the south to the north end of the study area was selected (Fig. 5c), as well as all horizontal cross sections close to the surface (Fig. 10).

Table 2: Relevant output quantities of the PALM-4U model (PALM RP, 2023). The first column gives the name of the output quantity, the second column gives the quantity denotation within the PALM-4U model, and the third column gives the unit. Quantities marked with an asterisk in the PALM-4U denotations were only output at a fictitious first grid level above the horizontal surface, i.e., the first 100 % fluid grid cell for each horizontal grid position. The fourth column indicates the name of the NetCDF output files. The output file DATA_2D contained data of the selected horizontal or vertical two-dimensional cross sections. The output files DATA_1D_PR contained horizontally averaged vertical profiles. All output data was temporally averaged by 10 min.

quantity name	**PALM-4U denotation**	**unit**	**NetCDF output files**
air pressure	hyp	hPa	DATA_1D_PR
ground heat flux	ghf*	$\mathrm{W\,m^{-2}}$	DATA_2D
incoming longwave radiation	rad_lw_in*	$\mathrm{W\,m^{-2}}$	DATA_2D
incoming shortwave radiation	rad_sw_in*	$\mathrm{W\,m^{-2}}$	DATA_2D
latent heat flux	qsws*	$\mathrm{W\,m^{-2}}$	DATA_2D
net all-wave radiation	rad_net*	$\mathrm{W\,m^{-2}}$	DATA_2D
outgoing longwave radiation	rad_lw_out*	$\mathrm{W\,m^{-2}}$	DATA_2D
outgoing shortwave radiation	rad_sw_out*	$\mathrm{W\,m^{-2}}$	DATA_2D
potential temperature	theta	K	DATA_2D
relative humidity	rh	%	DATA_2D
sensible heat flux	shf*	$\mathrm{W\,m^{-2}}$	DATA_2D
surface temperature	tsurf*	K	DATA_2D
u-component of the velocity	u	$\mathrm{m\,s^{-1}}$	DATA_2D
v-component of the velocity	v	$\mathrm{m\,s^{-1}}$	DATA_2D
water vapor mixing ratio	q	$\mathrm{kg\,kg^{-1}}$	DATA_2D
wind direction	wdir	°	DATA_2D
wind speed	wspeed	$\mathrm{m\,s^{-1}}$	DATA_2D

For this study, the term *modeled surface height* was defined as the height of the first grid level above the surface, i.e., the first 100 % fluid grid cell. For the 20 m spatial resolution, only four different surface heights were present (Fig. 12a). Therefore, the topography of the study area was only roughly visible and only a few tall buildings were seen which reached a higher layer. On the contrary, the cityscape of Bayreuth was apparent for the 5 m spatial resolution and showed single buildings and structures (Fig. 12b).

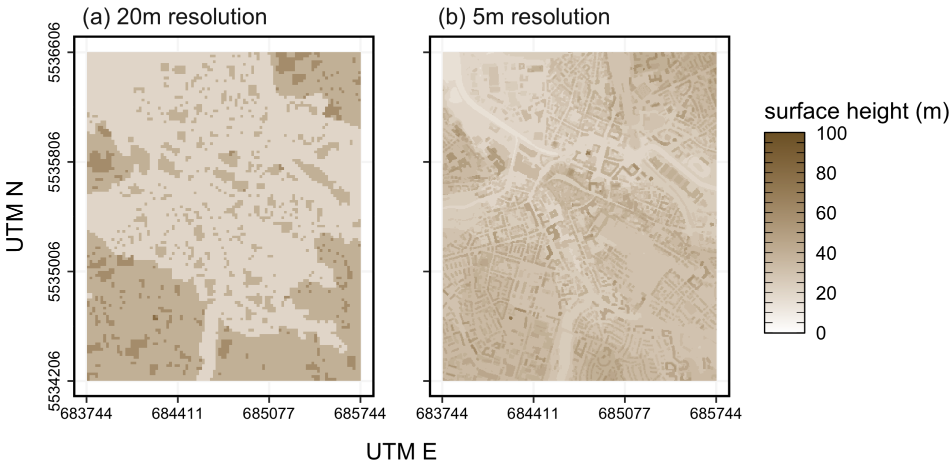

Figure 12: Horizontal cross section of the study area showing the modeled surface height (m), i.e., the height of the first 100 % fluid grid cell, for (a) the 20 m and (b) the 5 m spatial resolution.

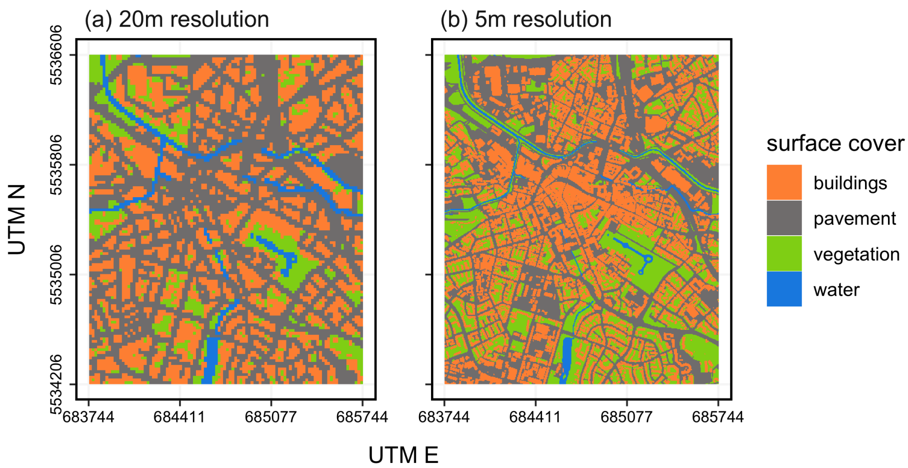

Figure 13: Horizontal cross section of the study area showing the modeled surface cover types for (a) the 20 m and (b) the 5 m spatial resolution.

The surface cover information originated from shapefiles which were transformed into NetCDF files, and which then were adjusted to fit the grid. A surface grid cell was filled with information as soon as it was touched within the origin shapefile. During rasterization, each surface cover type underwent an all-touched approach as grid cells cannot be partly filled (Sungur, 2021). For the 5 m spatial resolution, the PALM-4U-default prioritization scheme, i.e., buildings are prioritized over water, pavement, and finally vegetation, was kept. For the 20 m spatial resolution, the scheme was altered to water, pavement, buildings, and finally vegetation. Otherwise, buildings would have dominated most street canyons and water bodies, which are crucial for urban climate simulations (Sungur, 2021). As a result, the cityscape was apparent for both spatial resolutions, with the 5 m spatial resolution showing more details expectedly (Fig. 13, Tab. 3). Table 3 gives an overview of the selected measurement stations and their surroundings within the simulated environment. The surface beneath the Birken station was covered with asphalt and beneath the Markt station it was covered with stone. At the Mistel station, the surface cover differed between the spatial resolutions: at the 20 m spatial resolution it was a water surface and at the 5 m spatial resolution it was a vegetation cover (short grass).

Table 3: Overview of the measurement stations (Birken, Markt, and Mistel) and their surroundings in a square with a side length of 260 m centered at the measurement station from the model's perspective. It includes the domain position of the grid cells, which cover the location of the respective measurement stations, and a horizontal cross section showing the surrounding surface cover types at both spatial resolutions.

	Birken	Markt	Mistel
Location			
grid cell in the PALM-4U model	20 m: x = 67; y = 9; z = 3 5 m: x = 268; y = 33; z = 5	20 m: x = 46; y = 74; z = 2 5 m: x = 181; y = 293; z = 3	20 m: x = 10; y = 65; z = 2 5 m: x = 40; y = 260; z = 3
Surface cover and building height surrounding the stations (square with 260 m inradius)			
buildings with height (m) >0-5 >5-10 >10-15 >15-20 >20-25 >25-30 >30 pavement vegetation water NA station cell (20m)	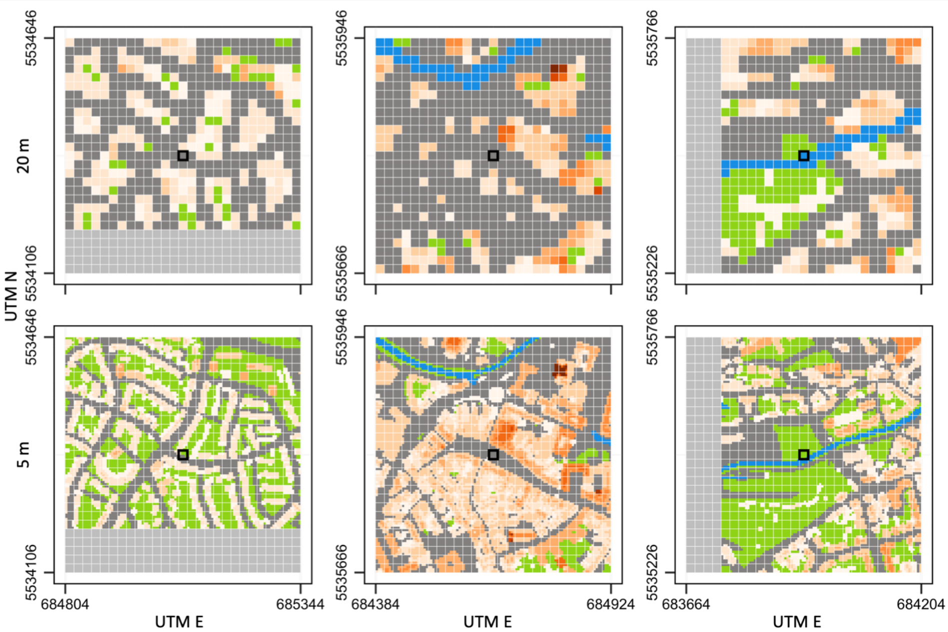		

4.4 Data processing

For the first objective, the observed data at the measurement stations was compared with the respective modeled data at two spatial resolutions (20 and 5 m). For the second objective, modeled data at the 20 m spatial resolution was compared with data at the 5 m spatial resolution for the whole study area. Because of the different data sets involved, this chapter describing the data processing was split into model-observation comparison (objective 1) and model-model comparison (objective 2).

4.4.1 Model-observation comparison

The observed data was taken from the selected measurement stations Birken, Markt, and Mistel for the respective time of the study period. The instruments recorded the data in Central European Time (CET) with a temporal resolution of 5 min averaging intervals. The data was transformed to 10 min averaging intervals by calculating the mean of two consecutive time steps, resulting in 156 time steps for the whole study period. For a more straightforward interpretation of the data, the time zone was converted to Central European Summer Time (CEST), which coincides with the time zone of the study area during the study period. Of the three relevant meteorological elements, air temperature $T_{°C}$ (°C) and horizontal wind speed M (m s^{-1}) were directly measured at the measurement stations. Observed specific humidity q (g kg^{-1}) was calculated as follows:

$$q = 0.622 \, \frac{\rho_v \cdot R_v \cdot T_K}{p - 0.378 \, \rho_v \cdot R_v \cdot T_K} \, \frac{1}{1000} \;\; (\mathrm{g\,kg^{-1}}) \, , \tag{22}$$

with the gas constant of water vapor R_v = 461.5 J kg^{-1} K^{-1}, absolute humidity ρ_v (kg m^{-3}), air temperature T_K (K), and air pressure p (Pa). All variables of Equation 22 were directly measured at the measurement stations.

The modeled data was extracted from of the grid cells covering the location of the measurement stations. The output was given in CET and converted into CEST to coincides with the time zone of the study area during the study period and with the time format of the observed data. Modeled air temperature $T_{°C}$ (°C) was calculated from potential temperature θ (K) with the rearranged Equation 16:

$$T_{°C} = \left(\theta \Big/ \frac{p_0}{p}\right)^{0.286} - 273.15 \;\; (°C). \tag{23}$$

The surface air pressure p_0 = 1013.25 hPa equaled the air pressure at the lowest layer of the root domain. 273.15 was subtracted to obtain air temperature $T_{°C}$ in °C. Modeled specific humidity q was calculated according to Equation 18. Water vapor pressure e (Pa) was calculated with relative humidity rh (%), a direct model output, and saturation water vapor pressure e_s

(Pa) (Foken, 2017):

$$e = \frac{rh \cdot e_s}{100\%} \ \text{(Pa)}. \tag{24}$$

Saturation water vapor pressure e_s (Pa) was defined with Magnus' equation (Foken, 2017):

$$e_s = 6.112^{\frac{17.62 T_K}{243.12 + T_K}} \ \text{(Pa)}, \tag{25}$$

where air temperature T_K is given in K. Finally, the horizontal wind speed M (m s^{-1}) was directly taken as an output quantity of the model. For the 5 m spatial resolution, the gird cell covering the Markt station (x = 181, y = 193, z = 3, compare Tab. 3) was located directly east of a solid grid cell (x = 180, y = 193, z = 3). As described in Chapter 4.3, velocity components are defined at the edges of each grid cells and are zero if the edge is next to a solid grid cell. Therefore, the aggregated wind speed values of the neighboring grid cells north (x = 181, y = 194, z = 3) and east (x = 182, y = 193, z = 3), which were not bordering any solid grid cells, were taken as wind speed values for the Markt station at the 5 m spatial resolution. The time series of the single observed and modeled meteorological element at each measurement station were plotted in Figures 15, 16, and 17.

The difference (Eq. 26) and the absolute difference (Eq. 27) between the observed (obs) and the modeled (mod) values at the measurement stations were calculated for each meteorological element $X \in \{T_{°\mathrm{C}}, q, M\}$:

$$\Delta_{obs-mod}\, X = X_{obs} - X_{mod} \,. \tag{26}$$

$$|\Delta_{obs-mod}\, X| = |X_{obs} - X_{mod}| \,. \tag{27}$$

For this thesis, the *night period* was defined as the time with an incoming shortwave radiation below 10 W m^{-2} to account for possible measurement inaccuracies of the pyranometer (WMO, 2021). This definition resulted in 54 night period steps (2019-07-25 21:00 to 2019-07-26 05:50 CEST). Angevine et al. (2001) point out the relevance of the morning transition (MT) period in which the nocturnal stable boundary layer shifts to a daytime convective boundary layer. Therefore, the *MT period* was included as a third time period in this study. It was defined as the time between sunrise and the sign change of the sensible heat flux (Beare, 2008).

For the study period of this thesis, the MT period started with the first time step after sunrise and ended when the modeled sensible heat flux at most measurement stations and spatial resolutions experienced a sign change. Figure A.2 in the appendix shows the detailed timing of the modeled sign changes of the sensible heat fluxes for each measurement station and spatial resolution. Hence, the MT period lasted from 2019-07-26 06:00 till 2019-07-26 08:00 CEST encompassing 13 time steps. The remaining 89 time steps were assigned to the *day period*.

For hypothesis 3, the spatial resolution differences were compared to the building height heterogeneity at the measurement stations. The building height heterogeneity was defined as the standard deviation of the building height σ_{BH} (m) in a square with a side length of 260 m centered at the measurement station:

$$\sigma_{BH} = \sqrt{\frac{1}{(n-1)} \sum_{i=1}^{n} (BH_i - \mu_{BH})^2} \ \ (\mathrm{m}), \tag{28}$$

where BH was the building height of each square meter i within a squared area, n was the total amount of square meters which was covered by a building, and μ_{BH} (m) was the mean building height in the square.

To compare the model-observation differences $\Delta_{obs-mod}$ at the different time periods for hypothesis 1, box plots were created (Fig. 18, Fig. 19). To answer hypotheses 2 and 3, box plots of the model-observation differences at the three measurement stations were plotted in Figure 20.

4.4.2 Model-model comparison

The second objective was solely concerned with the modeled data. The output of the 20 m spatial resolution was compared with the 5 m spatial resolution over the whole extent of the study area. For hypothesis 4 the horizontal spatial resolution differences near the surface were analyzed, whereas for hypothesis 5 the spatial resolution differences of the vertical cross section were examined.

4.4.2.1 Hypothesis 4

To analyze the output near the horizontal surface, the grid cells at the surface level were identified first. A new horizontal layer consisting of the first 100 % fluid grid cell for each horizontal grid position was created. It had the dimension of 100 × 120 grid cells for the 20 m spatial resolution and 400 × 480 grid cells for the 5 m spatial resolution covering the whole study area. For the 5 m spatial resolution, 15 grid cells were interpolated because the first 100 % fluid grid cells laid on a vertical layer higher than layer 15, which was not selected as a cross section. To analyze the differences between the 20 m and the 5 m spatial resolution, the dimension of the 20 m spatial resolution data was transformed to the dimension of the 5 m spatial resolution. For this purpose, each 20 m grid cell was split in 16 5 × 5 m grid cells. Each new grid cell was assigned the same output values of the original 20 m grid cell. The new 20 m grid had the same dimension has the 5 m grid (400 × 480 grid cells). The temporal mean difference (Eq. 29) and the absolute temporal mean difference (Eq. 30) between the spatial resolutions was calculated for each relevant meteorological element $X \in \{\theta, m, M\}$:

$$\Delta_{5-20m}\,\overline{X} = \frac{1}{156}\sum_{i=1}^{156}(X\_5m_i - X\_20m_i), \tag{29}$$

$$|\Delta_{5-20m}\,\overline{X}| = \frac{1}{156}\sum_{i=1}^{156}(|X\_5m_i - X\_20m_i|), \tag{30}$$

with time step $i \in \{1:156\}$. The results were plotted in a heat map (Fig. 21).

The building height heterogeneity was defined in Equation 28 as the standard deviation of the building height. In contrast to objective 1, the considered areas here were not 260 m squares surrounding each measurement station. Rather the whole study area was divided into 100 × 100 m squares, resulting in a new coarser grid of 20 × 24 cells. The building height heterogeneity of each of these coarser grid cells was then calculated using Equation 28 with n = 100·100 = 10,000 m^2. The results were shown in Figure 22. To analyze the relation between the building height heterogeneity σ_{BH} and the spatial resolution difference Δ_{5-20m} of the meteorological elements, the spatial resolution difference of the coarser 20 × 24 grid cells was aggregated by taking the mean over all spatial resolution differences of the corresponding smaller grid cells (Fig. A.3 in the appendix). Finally, a regression was performed for each meteorological element (Fig. 24).

The surface cover heterogeneity was defined by the number of distinct surface cover types (buildings, pavement, vegetation, water) within each 100 × 100 m grid cell. The categories were named *low heterogeneity* for two surface cover types, *medium heterogeneity* for three, and *high heterogeneity* for all four surface cover types within one 100 × 100 m grid cell (Fig.

23). To analyze the relation between the surface cover heterogeneity and the spatial resolution difference, box plots were created for each meteorological element (Fig. 25).

4.4.2.2 Hypothesis 5

For hypothesis 5, the selected vertical cross section of the 20 m spatial resolution (layer 382, compare Fig. 10) and the selected cross sections at the 5 m spatial resolution (layers 180–183) were compared. Just like for the horizontal surface layer, the dimension of the 20 m spatial resolution was transformed to match the dimension of the 5 m spatial resolution by splitting each 20 m grid cell into 16 5×5 m grid cells with the same values (Fig. 14c,d). The four selected 5 m vertical cross sections were aggregated into one cross section by taking the mean of the four corresponding grid cells (Fig. 14b). The result were two cross sections, one from the 20 m spatial resolution (Fig. 14c) and one from the 5 m spatial resolution (Fig. 14b), which both had the dimension of280×60 grid cells in y and z direction respectively. In parallel to hypothesis 4, the temporal mean difference (Fig. 14a) and absolute temporal mean difference were calculated with Equations 29 and 30.

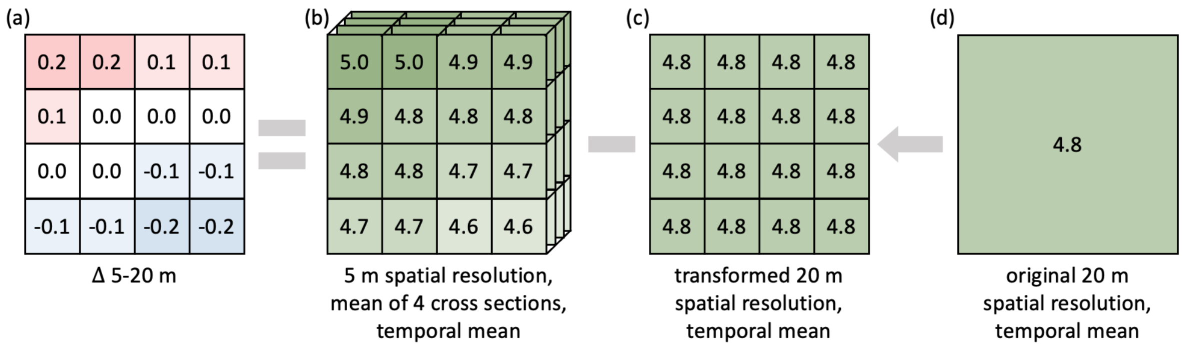

Figure 14: Sketch of the data processing for hypothesis 5. The temporal mean values are example values of wind speed ($m\,s^{-1}$). The panels are to be read from right to left. Panel (d) shows one grid cell of the vertical cross section of the 20 m spatial resolution. This grid cell was split into 16 5×5 m grid cells with the same value (panel (c)). Panel (b) shows 16 grid cells of the vertical cross section of the 5 m spatial resolution for which the mean of the four selected vertical cross sections was calculated. The values in panel (a) display the difference between the values in panel (b) and the values in panel (c). Positive differences are colored red, and negative differences are colored blue.

The spatial distribution of the differences was then displayed in Figure 26. This method led to a stripy pattern in the vertical cross sections which was an artefact of the chosen comparison method. For the 20 m spatial resolution, the values were constant within each 20 m height step (Fig. 14c), while for the 5 m spatial resolution (Fig. 14b) the values were gradually increasing or decreasing with every 5 m height step depending on the meteorological element. Therefore, the calculated differences at the bottom of one 20 m height step were negative while the calculated differences at the top were positive (Fig. 14a) producing a stripy pattern in Figure 26.

The roughness sublayer was calculated as three times the mean building height (Oke et al., 2017), which resulted in a top boundary of the roughness sublayer at 60 m above the bottom domain boundary. To analyze the spatial resolution difference between the roughness sublayer and higher layers of the UBL, a box plot for each meteorological element was created (Fig. 27).

5 Results

The results and evaluation of the hypotheses are presented in this chapter. Striking findings were summarized in Figure 28, which is displayed at the beginning of the subsequent Chapter 6. All hypotheses were framed in the format *"the differences of data set A are larger than the differences of data set B"*. For a proper comparison, most hypotheses were evaluated with box plots. Box plots are graphical representations of a data set's distribution and are well suited to compare data. A data set's 25th and 75th percentiles are located at the lower and upper border of the box, also known as the interquartile range (IQR). The lower and upper ends of the whiskers mark the smallest and the largest value of the data set, respectively. A hypothesis was not rejected if data set A was *decisively* larger than data set B. For this thesis, it was defined that two data sets are *decisively different* if their respective IQRs did not overlap, i.e., the 75th percentile of one data set B was below the 25th percentile of the other data set A. In this case, at least 75 % of the data points of data set A were higher than 75 % of the data points of data set B. In cases of no decisive difference between the data sets or a decisively larger data set B, the hypothesis was rejected. This definition does not take absolute differences into account which means that two data sets whose IQR do not overlap but have small absolute differences between the data points would be defied as decisively different by this definition. However, the advantage of this definition is that is easy to interpret, and it is a straightforward way to identify whether the two data sets cover the similar value range or not.

5.1 Model-observation comparison

The results and evaluation of the first three hypotheses under objective 1 are jointly described because they are based on the same data sets. For this objective, the observed air temperature, specific humidity, and wind speed at the three measurement stations Birken, Markt, and Mistel were compared with the modeled output for the grid cell covering the respective measurement station for both spatial resolutions (20 and 5 m).

5.1.1 Time series data

For air temperature (Fig. 15), observed and modeled values followed a similar course during the day period, and they deviated greater over night. All time series peaked in the afternoon of day one and decreased over night while the modeled values underestimated the nighttime decrease by up to 9.4 K. The observed air temperature at all measurement stations started increasing with sunrise at 2019-07-26 05:50 CEST while the increase in modeled air temperature was delayed by two hours and started at around 2019-07-26 08:00 CEST, the end of the morning transition (MT) period. During day two, the modeled air temperature was mostly lower than the observed temperatures by up to –3.8 K. Over all measurement stations and both spatial resolutions, the average differences ($\Delta_{obs-mod}\ T_{°C}$) during the day period was –0.9 K with maximum differences of –3.8 K while during the night period the average differences were 5.3 K with maximum differences of 9.4 K.

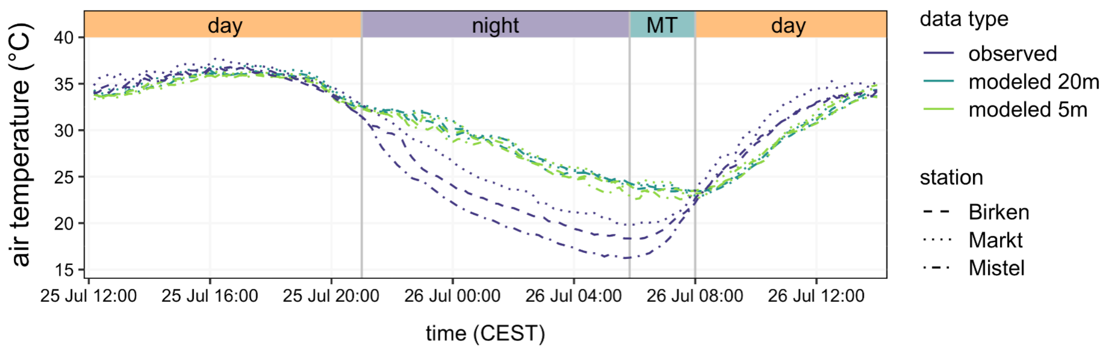

Figure 15: Time series of air temperature (°C) at the measurement stations Birken (dashed line), Markt (dotted line), and Mistel (dotted-dashed line). Observed values are purple and measured at a height of 3.5 m. Modeled values of the respective grid cell at the 20 m spatial resolution are dark green, and modeled values of the respective grid cell at the 5 m spatial resolution are light green. The three time periods are indicated at the top: day (2019-07-25 12:00 to 20:50 CEST and 2019-07-26 08:10 to 14:00 CEST), night (2019-07-25 21:00 to 2019-07-26 05:50 CEST), and morning transition (MT) (2019-07-26 06:00 to 08:00 CEST).

For the specific humidity (Fig. 16), both, observed and modeled values decreased at the beginning of the study period. While the observed specific humidity reached its minimum at 2019-07-25 19:40 CEST and then constantly increased over night until the late morning, the modeled specific humidity reached its low point already between 2019-07-25 16:10 and 16:30 CEST and then fluctuated. At the beginning of the night period both, the observed and modeled specific humidity increased but the modeled specific humidity peaked at around 2019-07-26 03:00 CEST and decreased afterwards while the observed data continued to increase. With the main exception of the time between 2019-07-25 17:20 and 20:20 CEST, the model underestimated the specific humidity by up to 3.2 g kg^{-1}. The model-observation differences of specific humidity ($\Delta_{obs-mod}\ q$) did not follow a distinctive diurnal course as it has been found for air temperature (Fig. 15). Differences were largest during the night period when the modeled specific humidity decreased after midnight while the observed specific humidity continued to slightly increase.

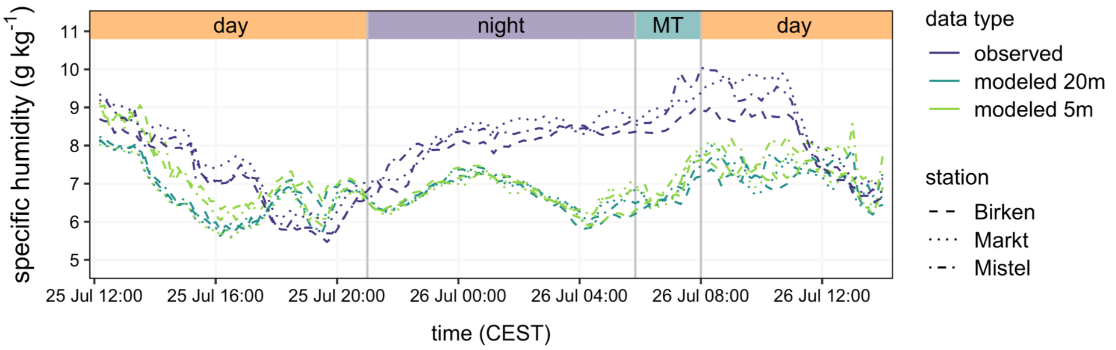

Figure 16: Time series of specific humidity (g kg^{-1}) at the measurement stations Birken (dashed line), Markt (dotted line), and Mistel (dotted-dashed line). Observed values are purple and measured at a height of 3.5 m. Modeled values of the respective grid cell at the 20 m spatial resolution are dark green, and modeled values of the respective grid cell at the 5 m spatial resolution are light green. The three time periods are indicated at the top: day (2019-07-25 12:00 to 20:50 CEST and 2019-07-26 08:10 to 14:00 CEST), night (2019-07-25 21:00 to 2019-07-26 05:50 CEST), and morning transition (MT) (2019-07-26 06:00 to 08:00 CEST).

The values for wind speed differed between the measurement stations and are therefore shown for each station separately in Figure 17. Highest observed wind speeds were measured during the day period of day one. 1.8 m s^{-1} was the maximum wind speed measured at the Birken station. With the sunset, the observed wind speed decreased at all three measurement stations and stayed below 0.7 m s^{-1} during the night period. After the MT period, the observed wind picked up again and increased slightly until the end of the study period. Maximum observed wind speed on day two was 1.2 m s^{-1} at the Birken station. The modeled wind speeds exceeded the observed wind speeds. Especially for the 20 m spatial resolution at the Birken station and both spatial resolutions at the Mistel station, modeled wind speeds exceeded the observed speeds by up to six times ($\Delta_{obs-mod}\ M$ = 3.8 m s^{-1}). Noticeable was also an increase in modeled wind speed between 2019-07-25 22:00 and 2019-07-26 03:00 CEST which was not seen in the observed data. For the modeled 5 m spatial resolution at the Birken station and both modeled spatial resolutions at the Markt stations, the modeled wind speeds followed the course and magnitude of the observed wind speeds more closely than at the other measurement stations and spatial resolutions. For all measurement stations and spatial resolutions, the differences between observed and modeled wind speeds were smaller in the second half of the time series from 2019-07-26 04:40 CEST on. During this period, the average model-observation difference over all measurement stations and spatial resolutions was 0.1 m s^{-1}. Overall, the modeled wind speeds at the 20 m spatial resolution showed larger differences to the observed wind speeds than the modeled wind speeds at the 5 m spatial resolution. A detailed list of descriptive values for Figures 15, 16, and 17 are found in Table A.1 in the appendix.

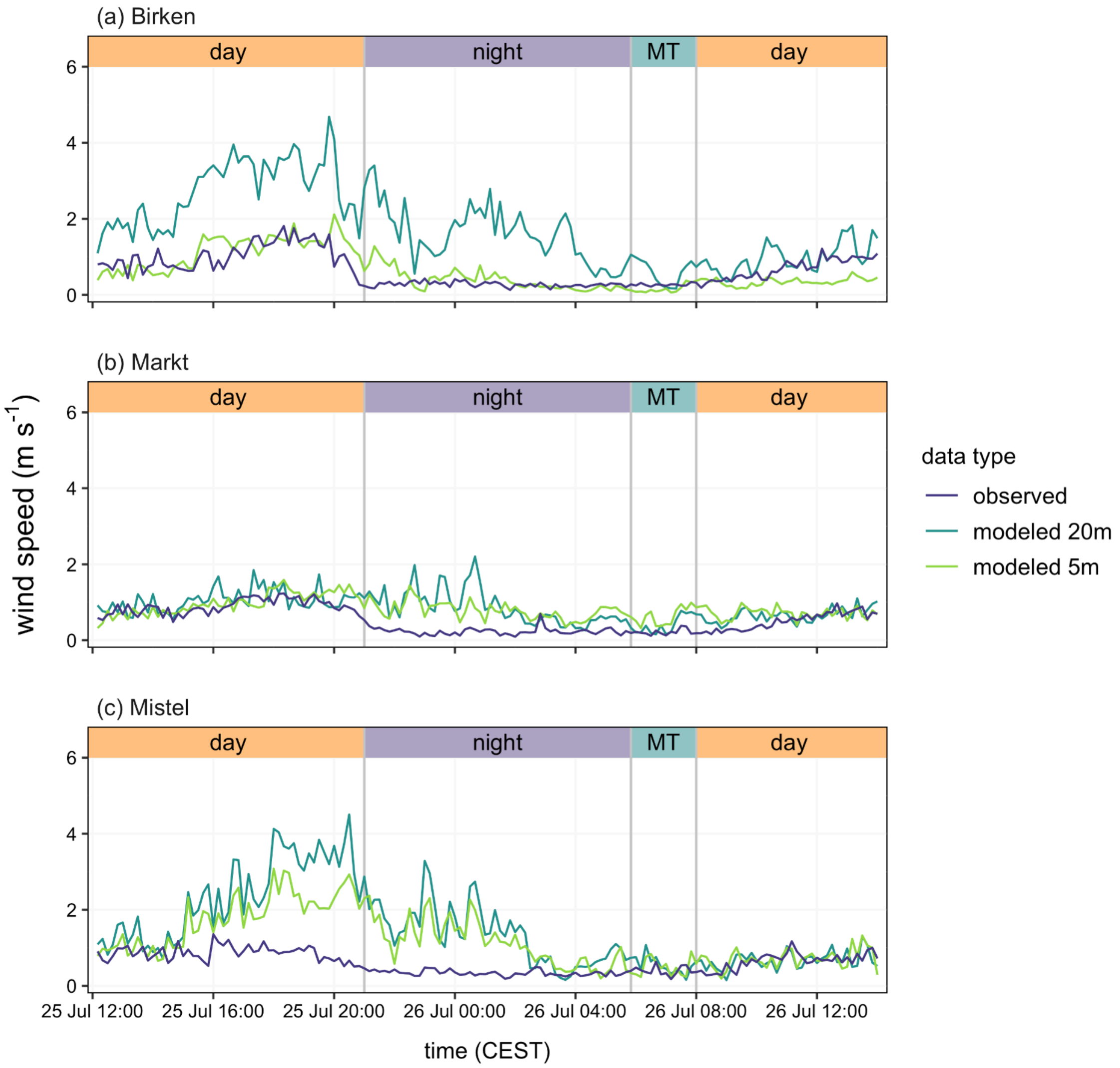

Figure 17: Time series of wind speed ($m\,s^{-1}$) at the measurement stations (a) Birken, (b) Markt, and (c) Mistel. Observed values are purple and measured at a height of 3.5 m. Modeled values of the respective grid cell at the 20 m spatial resolution are dark green, and modeled values of the respective grid cell at the 5 m spatial resolution are light green. The three time periods are indicated at the top: day (2019-07-25 12:00 to 20:50 CEST and 2019-07-26 08:10 to 14:00 CEST), night (2019-07-25 21:00 to 2019-07-26 05:50 CEST), and morning transition (MT) (2019-07-26 06:00 to 08:00 CEST).

5.1.2 Evaluating hypotheses 1 to 3

Hypotheses 1 to 3 were concerned with the model-observation differences. Box plots of the absolute differences between the observed and modeled data ($|\Delta_{obs-mod}\ X|$) were created for each meteorological element $X \in \{T_{°C}, m, M\}$ (Fig. 18, Fig. 19, Fig. 20). Hypothesis

1 stated that the model-observed differences of air temperature and specific humidity were larger during the day than during the night. For air temperature (Fig. 18), the IQR of the day period differences ($|\Delta_{obs-mod}\ T_{°C}|$) did not overlap with the IQR of the night period for any measurement station or spatial resolution. As defined above, this indicates a decisive difference between the periods in all cases. For the Birken and the Mistel stations, decisive differences were also found between the day and the MT period. The differences between the MT and night period were decisive at the Birken and Mistel station for the 20 m spatial resolution and the Mistel station for the 5 m spatial resolution while in the other cases the IQR overlapped, i.e., the differences were not decisive. Following this analysis, hypothesis 1, i.e., the differences in modeled and observed air temperature are larger during the day period than during the night period, was rejected for air temperature. Actually, the differences between modeled and observed air temperature are decisively larger during the night period than during the day period.

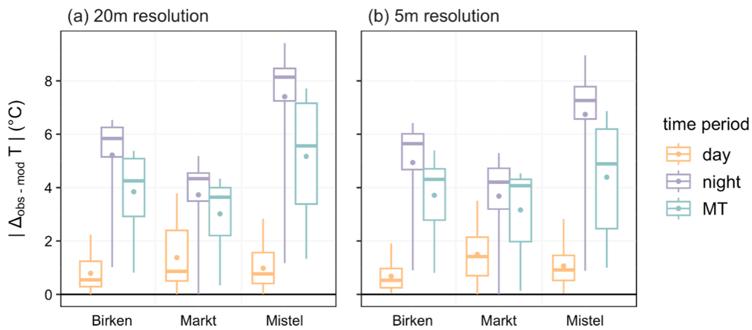

Figure 18: Box plots of the absolute difference between observed and modeled air temperature in °C ($|\Delta_{obs-mod}\ T_{°C}|$). Panel (a) shows the difference to the modeled data at the 20 m spatial resolution and panel (b) to the 5 m spatial resolution. For each measurement station Birken, Markt, and Mistel, the data was divided into three subsets representing the different time periods day (yellow), night (purple), and morning transition (MT) (green). The upper and lower border of the boxes mark the 75th and 25th percentile, respectively. The lowest and highest values are depicted at the bottom and top end of the whiskers, respectively. The horizontal line in each box represents the median and the dot is the position of the data set's mean.

For specific humidity (Fig. 19), the differences between the three time periods were not pronounced as already seen in Figure 16. The IQR between the day and night period did not overlap at any measurement stations or spatial resolutions. Therefore, the model-observation differences between the day and the night period are non-decisive across all measurement stations and spatial resolutions. Thus, hypothesis 1 was rejected for specific humidity, as well.

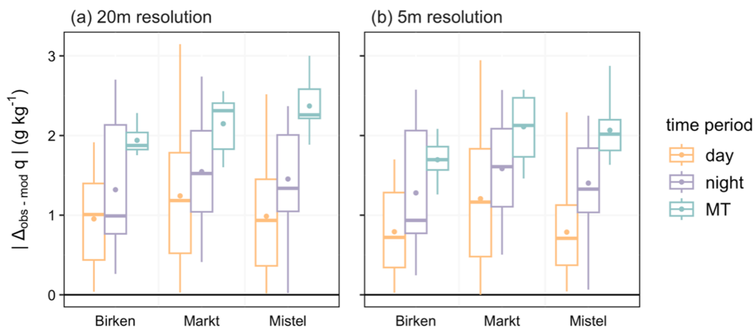

Figure 19: Box plots of the absolute difference between observed and modeled specific humidity in g kg^{-1} ($|\Delta_{obs-mod}\, q|$). Panel (a) shows the difference to the modeled data at the 20 m spatial resolution and panel (b) to the 5 m spatial resolution. For each measurement station Birken, Markt, and Mistel, the data was divided into three subsets representing the different time periods day (yellow), night (purple), and morning transition (MT) (green). The upper and lower border of the boxes mark the 75th and 25th percentile, respectively. The lowest and highest values are depicted at the bottom and top end of the whiskers, respectively. The horizontal line in each box represents the median and the dot is the position of the data set's mean.

Hypothesis 2 stated that the difference between the modeled and observed wind speed was larger in areas of high building-height heterogeneity than in less variable areas. The building height heterogeneity at each measurement station was defined in Equation 28 as the standard deviation of building height σ_{BH}. The highest building height heterogeneity was found at the Markt station with σ_{BH} = 11.7 m, followed by the Birken station with σ_{BH} = 5.5 m, and the Mistel station which σ_{BH} = 4.1 m. The box plots of the 20 m spatial resolutions (dark green) were overlapping, showing no decisive differences between the measurement stations (Fig. 20c). Identical results were found for the 5 m spatial resolution (light green boxes). Hypothesis 2 was therefore rejected.

Hypothesis 3 was concerned with the spatial resolution differences of the meteorological elements at the individual measurement stations and stated that the model-observed differences were larger for the 20 m spatial resolution than the 5 m spatial resolution. For the differences in air temperature and specific humidity at all measurement stations, the 20 and 5 m IQR were clearly overlapping in Figure 20 a and b, respectively, indicating non-decisive differences between the spatial resolutions. For wind speed in Figure 20c, the 20 and 5 m IQR were overlapping for the Markt and Mistel station but they were not overlapping for the Birken station. Therefore, hypothesis 3 was rejected except for wind speed at the Birken station where decisive differences between the spatial resolutions were found.

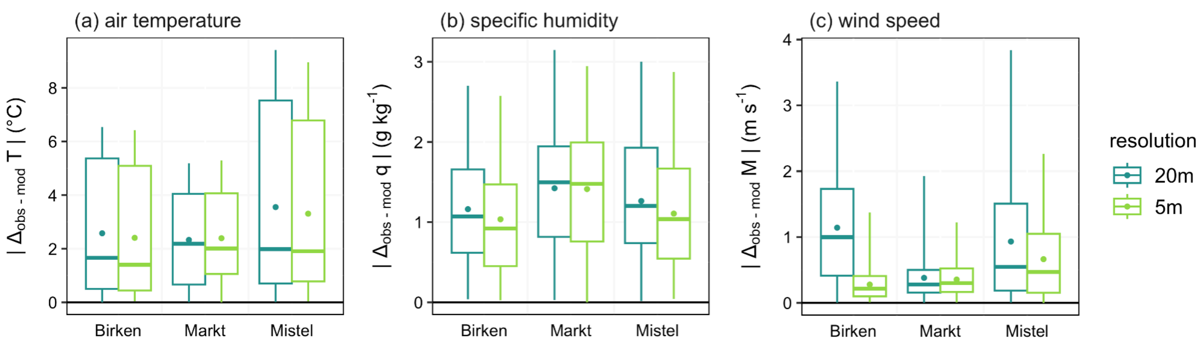

Figure 20: Box plots of the absolute difference between observed and modeled (a) air temperature in °C ($|\Delta_{obs-mod}\ T_{°C}|$), (b) specific humidity in g kg^{-1} ($|\Delta_{obs-mod}\ q|$), and (c) wind speed in m s^{-1} ($|\Delta_{obs-mod}\ M|$). For each measurement station Birken, Markt, and Mistel, the left box plot shows the difference to the modeled data at the 20 m spatial resolution and the left box plot shows the difference to the 5 m spatial resolution data. The upper and lower border of the boxes mark the 75th and 25th percentile, respectively. The lowest and highest values are depicted at the bottom and top end of the whiskers, respectively. The horizontal line in each box represents the median and the dot is the position of the data set's mean.

5.2 Horizontal model-model comparison

Hypothesis 4 of objective 2 was concerned with the differences between the modeled spatial resolutions at the first grid level above the surface, i.e., the first 100 % fluid grid cell, across the whole study. It stated that the differences between the data at the 5 m and the data at the 20 m spatial resolution were larger at more heterogeneous areas than at more homogeneous areas in terms of building height and surface cover.

5.2.1 Horizontal spatial data

For potential temperature (Fig. 21a), 94 % of the grid cells showed a difference between –0.5 and 0.5 K. The maximum difference was located above the Rotmain river in the northeast where the potential temperature was up to 6.9 K lower at the 5 m spatial resolution than the 20 m spatial resolution. At the 5 m spatial resolution, most potential temperature values were lower above water and green areas, e.g., at lake Röhrensee and the Mistel river area, and slightly warmer of up to 2.1 K over build up areas, e.g., at the city center, at Spinnerei and in St. Georgen, compared to the 20 m spatial resolution. The locations of the mentioned urban features are presented in Figure 5.

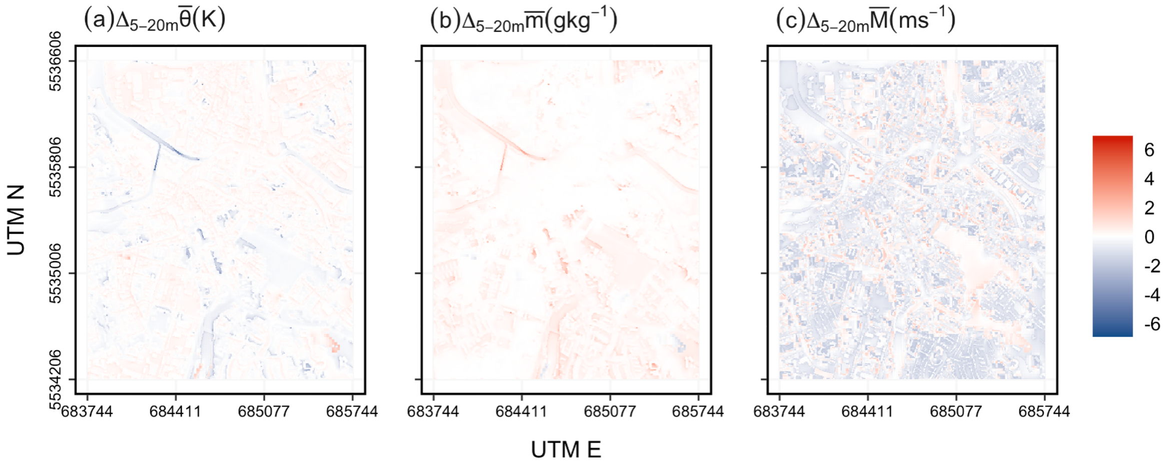

Figure 21: Horizontal cross section of the first grid level above the surface, i.e., the first 100 % fluid grid cell, covering the study area. Each grid cell shows the temporally averaged spatial resolution differences of (a) potential temperature in K ($\Delta_{5-20m}\ \overline{\theta}$), (b) water vapor mixing ratio in g kg^{-1} ($\Delta_{5-20m}\ \overline{m}$), and (c) wind speed in m s^{-1} ($\Delta_{5-20m}\ \overline{M}$). The color scale applies to all three plots in their respective units. Red grid cells indicate higher values for the 5 m spatial resolution and blue values indicated lower values for the 5 m spatial resolution.

Similarly, for the water vapor mixing ratio (Fig. 21b), most grid cells had small differences between the spatial resolutions. 83 % of the grid cells showed a difference between −0.3 and 0.3 g kg^{-1}. The majority (87 %) of the grid cells had higher values of up to 4.3 g kg^{-1} higher at the 5 m spatial resolution than 20 m spatial resolution with the highest differences above water and green areas. Only 13 % of the grid cells showed a lower water vapor mixing ratio at the 5 m spatial resolution of up to 1.5 g kg^{-1} lower. For the wind speed (Fig. 21c), lower spatial resolution differences were found over water and green areas like the lake Röhrensee, the Hofgarten, the Mistel river area, and the Rotmain river. These areas of lower spatial resolution differences could also be characterized as open-field areas which were not covered by buildings. Also, the train tracks in the north, which constitute also an open area, showed low differences. 52 % of the grid cells showed a difference between −0.5 and 0.5 m s^{-1}. Most of the grid cells (71 %) showed slower wind speeds for the 5 m spatial resolution of up to −2.5 m s^{-1} lower while 30 % of the grid cells showed up to 2.3 m s^{-1} higher wind speeds for the 5 m spatial resolution.

5.2.2 Evaluating hypothesis 4

To evaluate hypothesis 4, the heterogeneity of the study area in terms of building height and surface cover was analyzed. Hypothesis 4 stated that the spatial resolution differences were larger at areas with greater building height and surface cover heterogeneity than at more homogeneous areas. Building height heterogeneity was defined as the building height standard deviation (Eq. 28). The highest building height heterogeneity (σ_{BH} = 20.5 m) was found in the 100 × 100 m grid cell covering the city hall which is the tallest building within the study area (Fig. 22). Other high building height heterogeneity areas were located at other tall buildings, e.g., the Graf Münster high school east of Hofgarten, the city church of the Holy Trinity, and a multi-purpose building at Spinnerei. In general, the city center was characterized by a greater building height heterogeneity while the grid cells towards the edges of the study area showed a lower building height heterogeneity. Areas at the Hofgarten, the Mistel river, the Rotmain river and other open areas showed very low or no heterogeneity as they were covered by very few or no buildings.

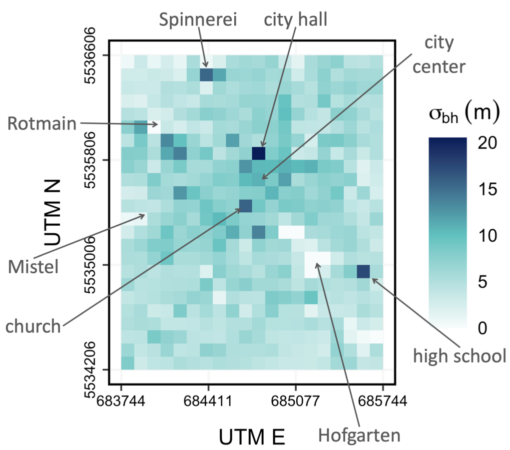

Figure 22: Building height heterogeneity (σ_{BH}) of each 100 × 100 m grid cell of the study area. Darker shades indicate higher heterogeneity. The location of features mentioned in the text are marked with grey arrows.

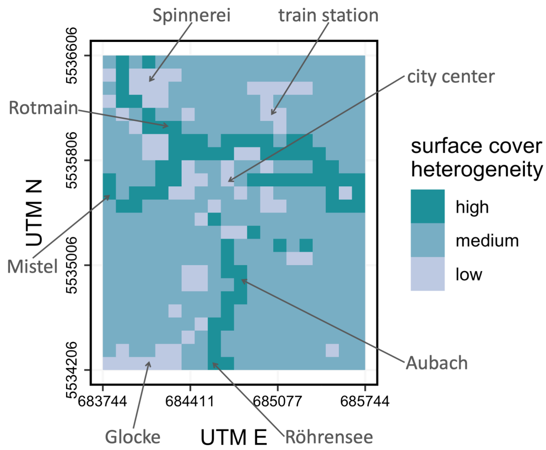

Figure 23: Surface cover heterogeneity of each 100 × 100 m grid cell of the study area. Grid cells with low, medium, or high heterogeneity cover two, three, or four different surface cover types, respectively. The location of features mentioned in the text are marked with grey arrows.

The explanatory power of the building height heterogeneity for the spatial resolution differences was found to be low with R^2 = 0.01, 0.12, 0.02 for potential temperature, water vapor mixing ratio, and wind speed, respectively (Fig. 24). The results do not support that spatial resolution differences are higher at areas of greater building height heterogeneity for any meteorological element. Thus, hypothesis 4 concerning the building height heterogeneity was rejected.

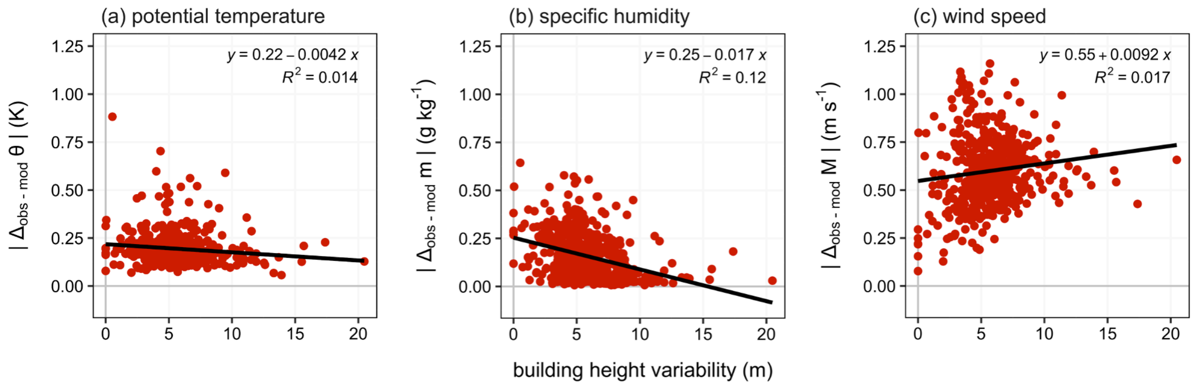

Figure 24: Scatter plots showing the regression of building height heterogeneity σ_{BH} (m) vs. the temporally averaged absolute spatial resolution differences of (a) potential temperature in K ($|\Delta_{5-20m}\ \overline{\theta}|$), (b) water vapor mixing ratio in g kg^{-1} ($|\Delta_{5-20m}\ \overline{m}|$), and (c) wind speed in m s^{-1} ($|\Delta_{5-20m}\ \overline{M}|$).

Concerning the surface cover heterogeneity, higher heterogeneity values were found along the water areas Rotmain river, Mistel river, Röhrensee lake, and Aubach creek while areas with low surface cover heterogeneity were dominantly located in the industrial parks Glocke (southwest) and Spinnerei (northeast), the city center, and the area around the train station north of the city center (Fig. 23).

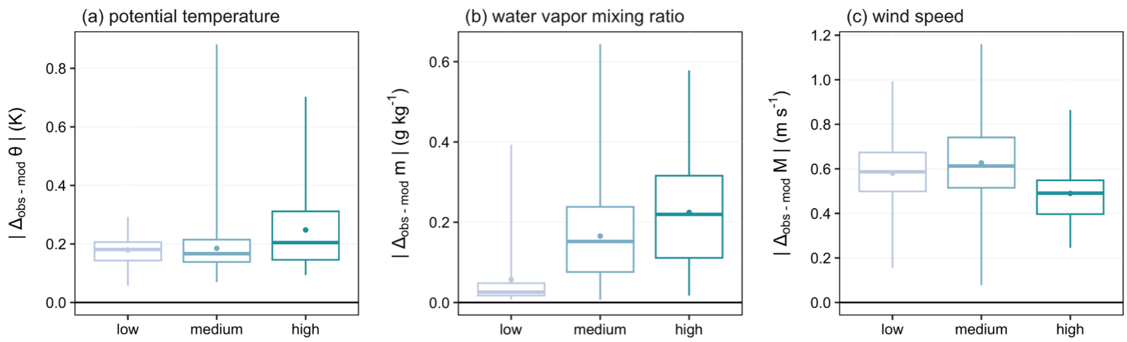

Figure 25: Box plots of the temporally averaged absolute spatial resolution difference of (a) potential temperature in K ($|\Delta_{5-20m}\ \overline{\theta}|$), (b) water vapor mixing ratio in g kg^{-1} ($|\Delta_{5-20m}\ \overline{m}|$), and (c) wind speed in m s^{-1} ($|\Delta_{5-20m}\ \overline{M}|$) for each surface cover heterogeneity category (low, medium, high). The upper and lower border of the boxes mark the 75th and 25th percentile, respectively, while the lowest and highest values are depicted at the bottom and top end of the whiskers, respectively. The horizontal line in the box represents the median and the dot is the position of the data set's mean.

For the potential temperature (Fig. 25a), the mean spatial resolution difference value slightly increased with greater surface cover heterogeneity, however all IQR overlapped. Therefore, no decisive relation could be detected. For the water vapor mixing ratio (Fig. 25b), the mean spatial resolution difference also increased and the IQR showed decisive differences between low and medium, and low and high surface cover heterogeneity. The difference between the medium and high heterogeneity was not decisive. For wind speed (Fig. 25c), all IQR overlapped. Concluding, the results did not support that the differences between the 5 m and 20 m spatial resolution were larger at more heterogeneous areas in terms of building height and surface cover than at more homogeneous areas. Therefore, hypothesis 4 was rejected. The only exception was a decisive difference between low and medium, and low and high surface cover heterogeneity for the water vapor mixing ratio.

5.3 Vertical model-model comparison

The second part of objective 2 was concerned with the vertical differences between the data at the 5 m and the data at the 20 m spatial resolution. Therefore, data of the vertical cross section, covering a 20 m wide strip in north-south direction of the study area was analyzed. Within this cross section the spatial resolution difference Δ_{5-20m} of potential temperature, water vapor mixing ratio, and wind speed were calculated using Equation 29.

5.3.1 Vertical spatial data

For the vertical cross sections, most grid cells showed higher difference between the spatial resolutions within the roughness sublayer (RSL) than at higher levels of the urban boundary layer (UBL) (Fig. 26). The stripes seen in Figure 26 were caused by the comparison methods of the two spatial resolutions as explained with Figure 14 in Chapter 4.4.2.2. For potential temperature, 78 % of the grid cells in the RLS and 99 % of the grid cells in the higher UBL had a difference between −0.1 and 0.1 K. For the water vapor mixing ratio, 66 % of the grid cells in the RLS and 96 % of the grid cells in the higher UBL have a difference between −0.04 and 0.04 g kg^{-1}. For wind speed, 37 % of the grid cells in the RLS and 99 % of the grid cells in the higher UBL have a difference between −0.2 and 0.2 m s^{-1}. For potential temperature and water vapor mixing ratio, the larger differences in the RLS were concentrated in the south above the Röhrensee lake and the adjacent vegetated and lightly build-up area north of the lake. At these areas, the potential temperature at the 5 m spatial resolution was up to 1.3 K warmer than at the 20 m spatial resolution, and the water vapor mixing ratio was up to 0.95 g kg^{-1} higher at the 5 m spatial resolution than at the 20 m spatial resolution. The larger spatial resolution differences of the wind speeds were more distributed throughout the RSL of the whole cross section. Above the Röhrensee and north of the Maximilianstraße, the wind speeds were up to

$1.4\,\mathrm{m\,s^{-1}}$ higher at the 5 m spatial resolution than the 20 m spatial resolution while above the build-up area north of the Röhrensee, the city center, and the build-up area in the north of the study area the wind speeds were up to $1.7\,\mathrm{m\,s^{-1}}$ lower for the 5 m spatial resolution.

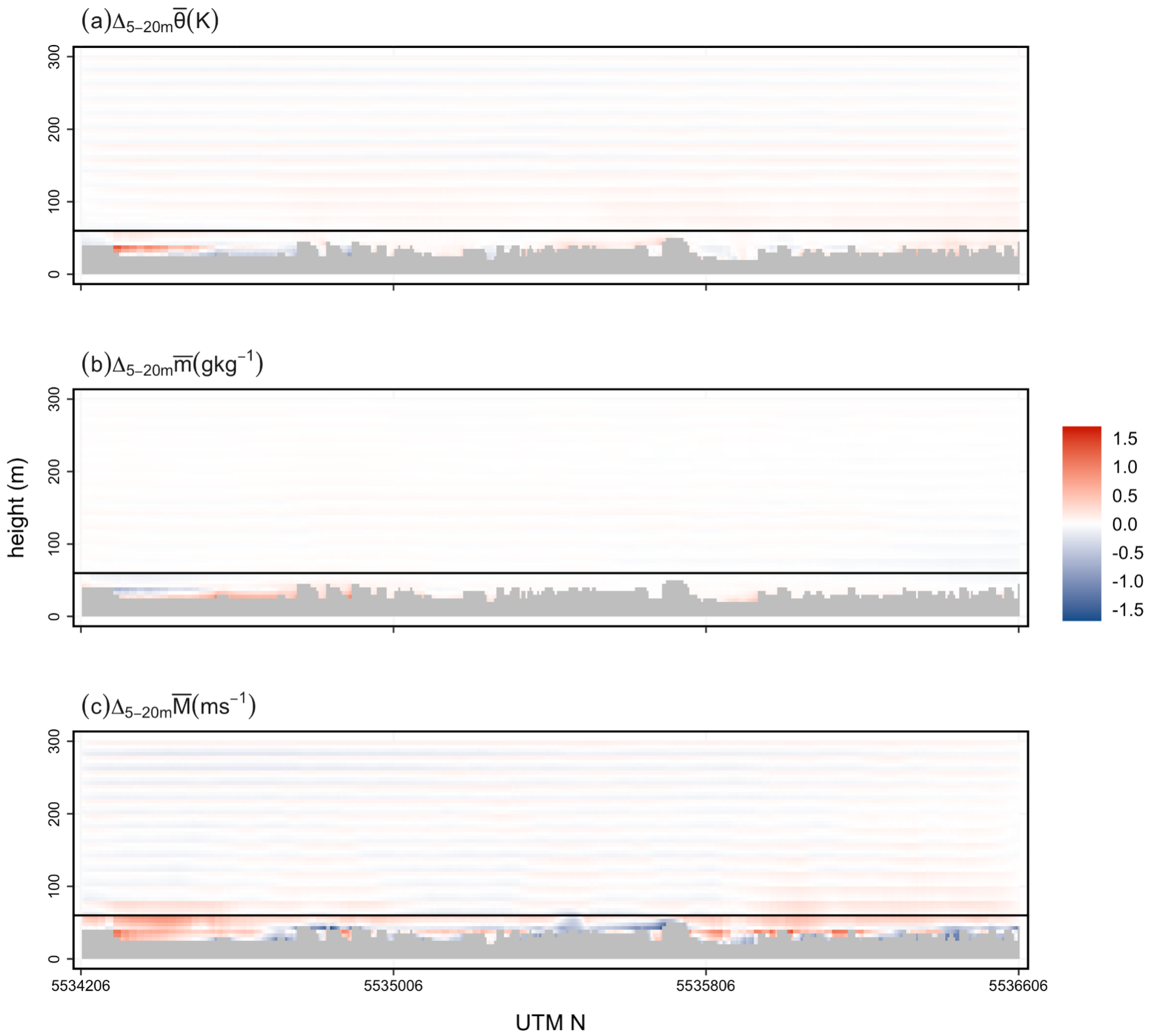

Figure 26: Vertical cross section of the study area showing the temporally averaged spatial resolution differences of (a) potential temperature in K ($\Delta_{5-20m}\ \overline{\theta}$), (b) water vapor mixing ratio in $\mathrm{g\,kg^{-1}}$ ($\Delta_{5-20m}\ \overline{m}$), and (c) wind speed in $\mathrm{m\,s^{-1}}$ ($\Delta_{5-20m}\ \overline{M}$). The cross section intersects the study area from south (left) to north (right) at 684644 – 684664 E covering the Röhrensee and the city center of Bayreuth. The color scale applies to all three plots in their respective units. Red grid cells indicate higher values for the 5 m spatial resolution and blue values indicated lower values for the 5 m spatial resolution. Grey grid cells are 100 % solid grid cells.

5.3.2 Evaluating hypothesis 5

Hypothesis 5 stated that the spatial resolution differences were larger in urban roughness sublayer than at higher layers of the urban boundary layer. For potential temperature and water vapor mixing ratio (Fig. 27a and b, respectively), larger differences appeared solely in the RSL. However, for both meteorological elements, the IQR overlapped, indicating no decisive differences. Therefore, for potential temperature and the water vapor mixing ratio, no substantial spatial resolution difference between the RSL and the higher UBL could be detected. For wind speed (Fig. 27c), the IQR of the RSL did not overlap the IQR of the higher UBL box plot, indicating that more than 75 % of the grid cells in the RSL were higher than 75 % of the higher UBL, describing a decisive difference between these two sections. Consequently, hypothesis 5 was rejected for potential temperature and the water vapor mixing ratio but not for wind speed.

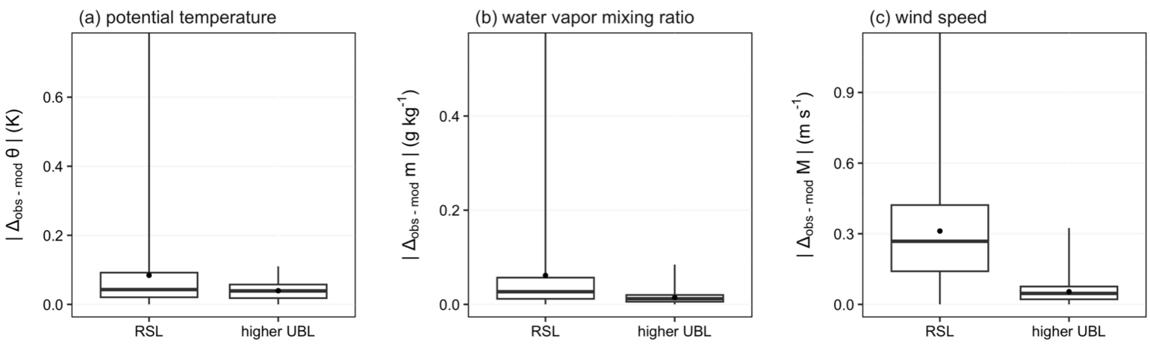

Figure 27: Box plots of the temporally averaged absolute spatial resolution difference of (a) potential temperature in K ($|\Delta_{5-20m}\ \overline{\theta}|$), (b) water vapor mixing ratio in g kg^{-1} ($|\Delta_{5-20m}\ \overline{m}|$), and (c) wind speed in m s^{-1} ($|\Delta_{5-20m}\ \overline{M}|$). In each panel, the left box plot depicts the date within the roughness sublayer (RSL) and the right box plot depicts date within the higher urban boundary layer (UBL). The upper and lower border of the boxes mark the 75th and 25th percentile, respectively, while the lowest and highest values are depicted at the bottom and top end of the whiskers, respectively. The horizontal line in the box represents the median and the dot is the position of the data set's mean. For a better visibility of the box plot displaying the data of the higher UBL layers, the y axis was shortened. Therefore, less than the top 1 % of the RSL data points are not visible in each panel.

6 Discussion

This chapter discusses the results of this thesis and provides possible explanations for the findings. Figure 28 recapitulates the most striking findings of Chapter 5 and assorts them into four discussion topics which structure this chapter. After outlining some general limitations of this study below, the reasons for the overestimation of modeled nighttime air temperature and the delay in the morning increase of the modeled air temperature are discussed in Chapter 6.1. Chapter 6.2 debates possible explanations for the modeled underestimation of specific humidity and Chapter 6.3 examines all findings regarding the relation between wind speed and building height or surface structure. Finally, results concerned with spatial resolution differences of temperature and humidity values are discussed in Chapter 6.4.

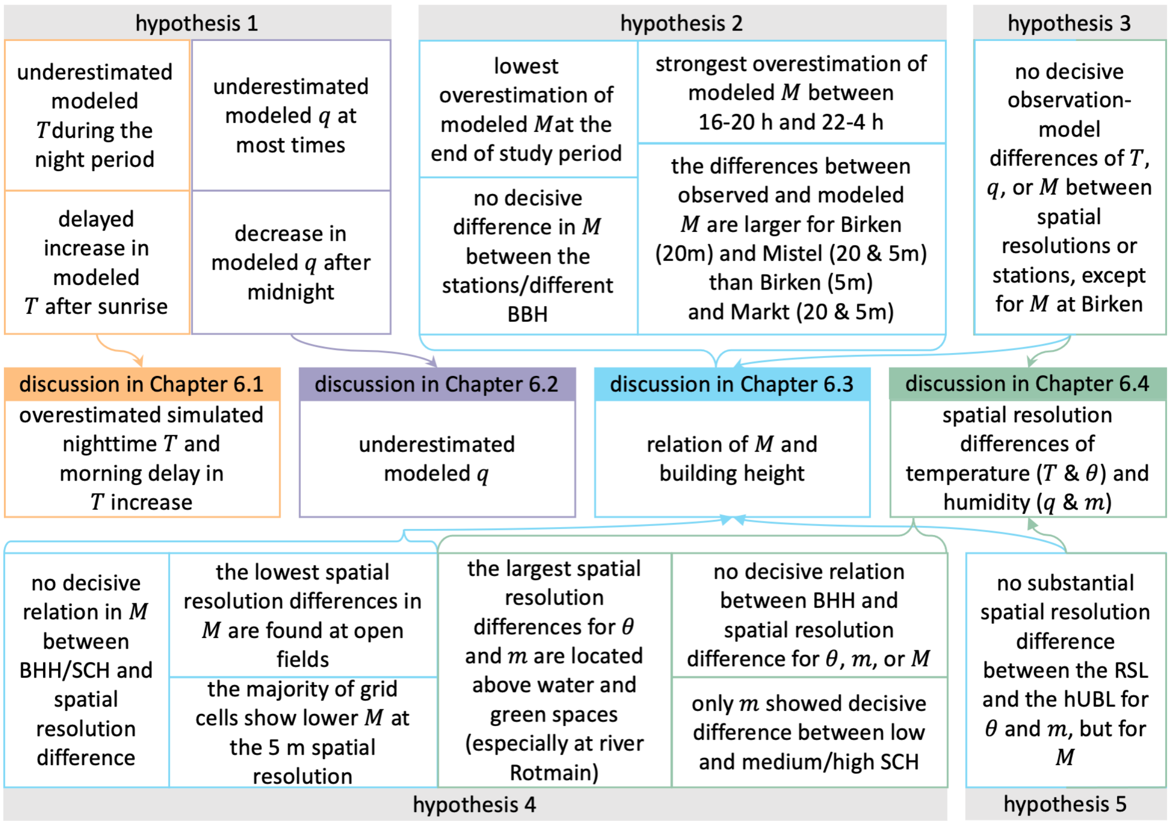

Figure 28: Flow chart of this thesis' most striking findings and the corresponding chapter in which they are discussed (colored boxes in the middle). The abbreviations and symbols are air temperature T, building height heterogeneity (BHH), potential temperature θ, roughness sublayer (RSL), specific humidity q, surface cover heterogeneity (SCH), water vapor mixing ratio m, and wind speed M.

A general uncertainty of the results could exist because the simulation was run without a spin-up period. The surface spin-up mechanism of PALM-4U runs a simulation solely based on the radiation model and the land and building surface model prior the main simulation. Maronga et al. (2020) recommend including a spin-up period because temperature and moisture content of the surface layers might not be sufficiently initialized otherwise, especially for simulations of single diurnal cycles. Initial material temperatures have a strong impact on the simulation output and therefore their realistic initialization is crucial. Because a spin-up period was not included in the simulation process of this thesis, the surface temperature and moisture content might not have been properly initialized. This might have caused a general uncertainty of the modeled data and a subsequent discrepancy between the modeled and observed data.

Another explanation for model-observation differences could be the overestimation of the modeled turbulent kinetic energy (TKE). As described in Chapter 2.4, turbulence causes mixing of air. An overestimated TKE would lead to an amplified mixing of the air's moisture and temperature properties causing lower vertical and horizontal temperature and moisture gradients. Overestimated TKE is a common issue in the PALM-4U model (Gronemeier et al., 2021). Because obstacles are represented on a rectilinear grid which turns smooth vertical and horizontal surfaces into sharp edges, surface roughness is increased causing higher turbulence. The modeled TKE was not further analyzed in this thesis because relevant parameters necessary for the calculation of TKE were not selected as output quantities for the PALM-4U model (compare Tab. 2).

A statistical issue occured when the data set of the 20 m spatial resolution was compared with the data set of the 5 m spatial resolution because the first data set consists of less data points. For the 20 m spatial resolution, the study area comprised $100 \cdot 120 = 12{,}000$ grid cells horizontally and $120 \cdot 15 = 1800$ grid cells vertically while the 5 m spatial resolution comprised $400 \cdot 480 = 192{,}000$ grid cells horizontally and $480 \cdot 60 = 28{,}800$ grid cells vertically. Averaging over a smaller number of data points results in a larger random error. This general statistic issue is not specific to this study and is not further addressed.

6.1 Overestimated modeled nighttime air temperature and morning delay

The results showed that nighttime air temperature was overestimated by the model by up to 9.4 K and that the modeled temperature increase after sunrise was delayed by two hours. According to Equation 14 (Chapter 2.5.1), air temperature change is driven by changes in the flux divergence of longwave radiation, turbulent sensible heat, and advection. To find explanations of the model's temperature deviation, the different drivers of temperature change within the model were examined below.

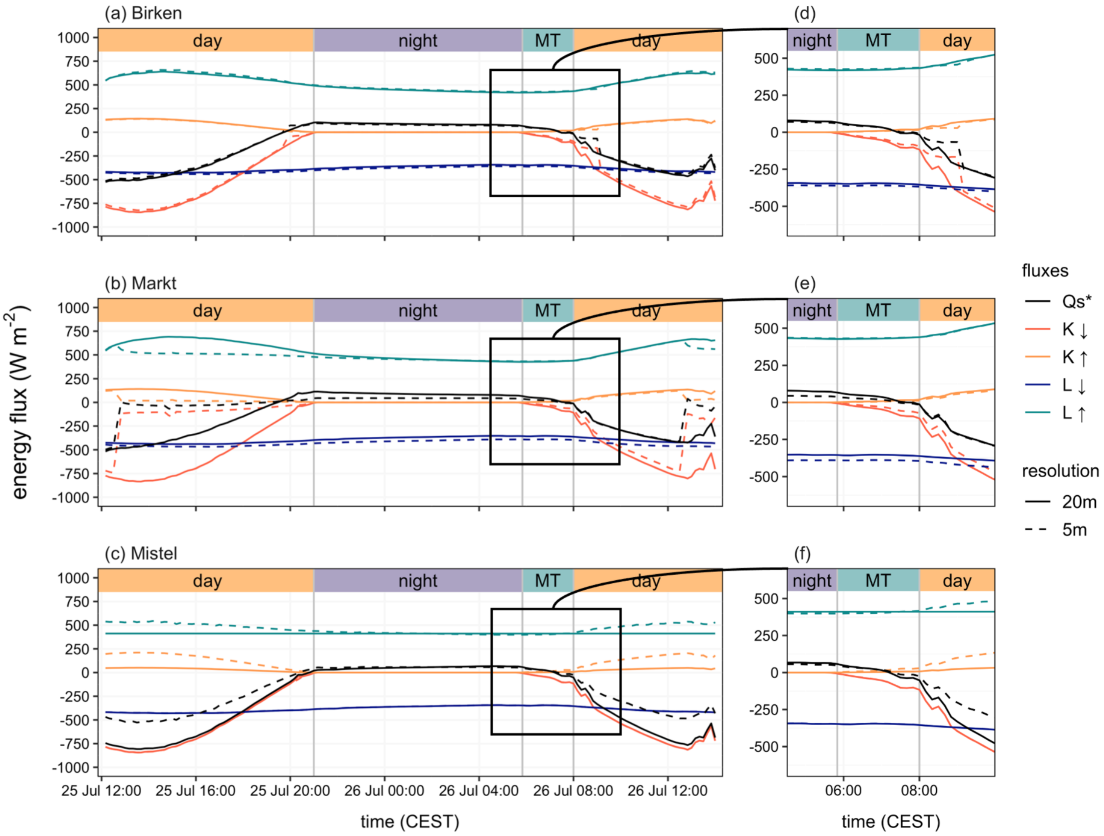

Figure 29: Time series of the modeled radiation fluxes in W m^{-2} at the measurement stations (a) Birken, (b) Markt, and (c) Mistel. The net all-wave radiation Q_S^* is represented by the black line, incoming ($K\downarrow$) and outgoing ($K\uparrow$) shortwave radiation are represented by the red and the yellow lines, respectively. Incoming ($L\downarrow$) and outgoing ($L\uparrow$) longwave radiation are represented by the blue and the green lines, respectively. Solid and dashed lines present values at the 20 m and 5 m spatial resolution, respectively. The three time periods are indicated at the top: day (2019-07-25 12:00 to 20:50 CEST and 2019-07-26 08:10 to 14:00 CEST), night (2019-07-25 21:00 to 2019-07-26 05:50 CEST), and morning transition (MT) (2019-07-26 06:00 to 08:00 CEST). Plots (d), (e), and (f) show a close up of the MT period for the Birken, Markt, and Mistel station, respectively.

Most modeled radiation fluxes at the measurement stations (Fig. 29) followed the expected course (compare Fig. 2a). The sharp decrease of incoming shortwave radiation $K\downarrow$ for the 5 m spatial resolution at the Markt station (Fig. 29b) at 2019-07-25 12:50 and 2019-07-26 12:40 CEST was caused by shading of nearby houses, which were not represented in the 20 m spatial resolution. Subsequently, the outgoing shortwave radiation $K\uparrow$ and the net all-wave radiation Q_S^* decreased for the 5 m spatial resolution. At the Mistel station (Fig. 29c), the $K\downarrow$ was identically for both spatial resolutions but outgoing shortwave and longwave radiation were lower at the 20 m spatial resolution. This can be explained by the different surface covers at the

Mistel station for the spatial resolutions, which differ in surface properties. The water surface cover of the 20 m spatial resolution had a lower albedo than the vegetation grid cell at the 5 m spatial resolution and therefore reflected less radiation. Further, in contrast to other surface types, the water temperature stayed constant during the entire model run, which is default by the PALM-4U model. It was set to 18.8 °C which was lower than the average surface temperature of the vegetated surface cover at the Mistel station at the 5 m spatial resolution (27.5 °C) (Fig. A.4 in the appendix). As the outgoing shortwave radiation at the surface depends on its temperature (Eq. 2), $L\uparrow$ was lower at the 20 m spatial resolution than at the 5 m spatial resolution.

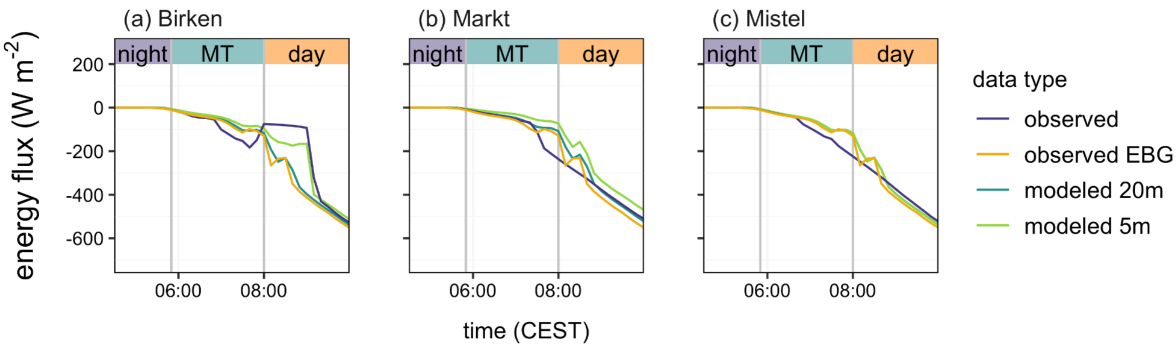

Figure 30: Time series between 2019-07-26 04:30 and 10:00 CEST of the incoming shortwave radiation fluxes in W m^{-2} at the measurement stations (a) Birken, (b) Markt, and (c) Mistel. The purple line represents the observed data at the respective measurement station, the dark and light green lines represent the modeled data at the 20 m and 5 m spatial resolution, respectively. The yellow line represents the observed data at the EBG station. The three time periods day, night, and morning transition (MT) are indicated at the top.

During the morning transition period, the fluxes took an unexpected course (Fig. 29d,e,f). Under cloudless conditions, as it was the case for the study period, the incoming shortwave radiation typically follows a sinusoidal curve (compare Fig. 2a) (Stull, 2017). Here, $K\downarrow$ increased first at a lower and then a sharper rate after 2019-07-26 08:00 CEST. Additionally, the curve had a small bend at 2019-07-26 08:30 CEST at all measurement stations. This unexpected course of $K\downarrow$ was observed across all measurement stations and spatial resolutions hinting at an inconsistency in the model's input data of radiation. The model's input for incoming shortwave radiation was derived from the meteorological measurement station in the EBG. It is noticeable that the observed bend and the slow increase were also measured at the EBG station (Fig. 30). Therefore, it can be concluded that the model followed the input radiation as it should, but the input radiation from the EBG was impacted by shading.

The observed radiation at the measurement stations showed a smooth sinusoidal curve during the morning transition period which the exception of the shading events at Birken between 2019-07-26 08:00 and 09:00 CEST and Markt between 2019-07-26 07:00 and 07:30 CEST (Fig. 30a,b, respectively). The underestimated modeled incoming shortwave radiation during the morning transition period led to an underestimated modeled energy availability, i.e., underestimated Q^*_S. Only at 2019-07-26 08:00 CEST, the sign of Q^*_S changed marking the turn from a net energy deficit to a net energy surplus. The sunrise, i.e., when $K{\downarrow} > 10\,\mathrm{W\,m^{-2}}$, occurred at 2019-07-26 06:00 CEST indicating light availability two hours before the sign change of Q^*_S.

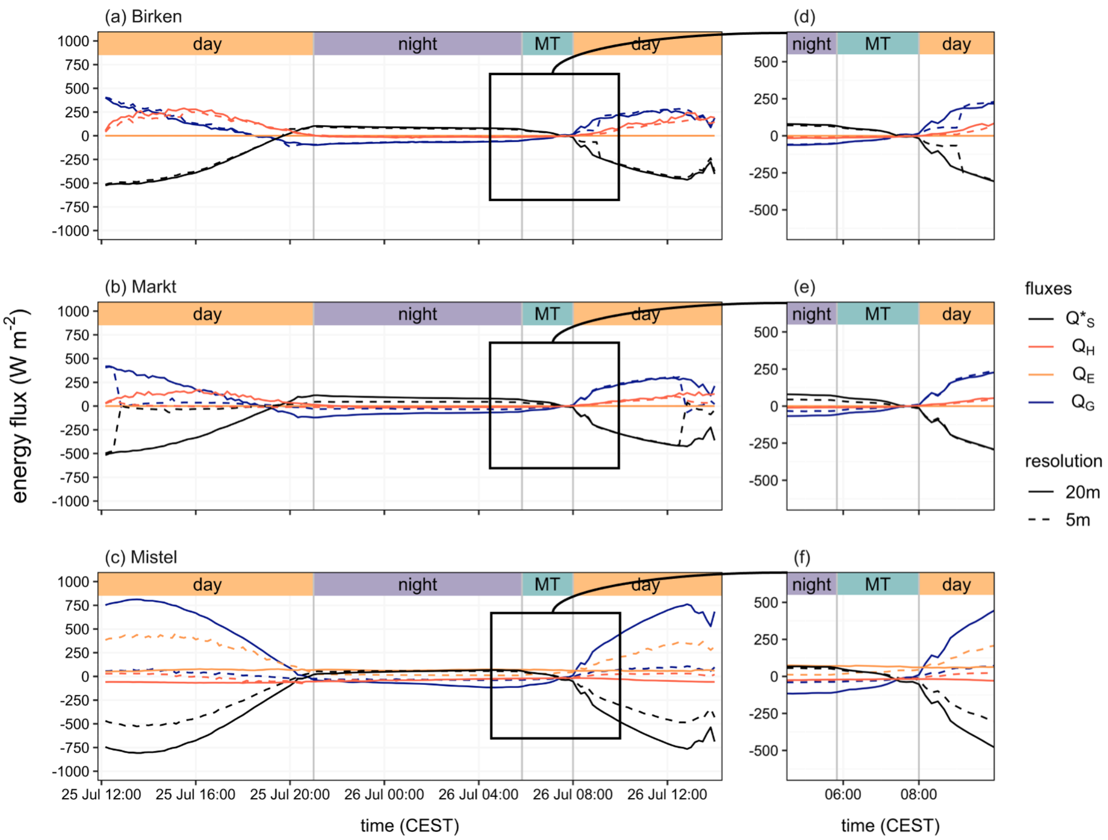

Figure 31: Time series of the modeled energy fluxes in $\mathrm{W\,m^{-2}}$ at the measurement stations (a) Birken, (b) Markt, and (c) Mistel. The net all-wave radiation Q^*_S is represented by the black line, the sensible (Q_H), latent (Q_E), and ground (Q_G) heat fluxes represented by the red, yellow and blue lines, respectively. The heat storage term (ΔQ_S) is represented by the green line. Solid and dashed lines present values at the 20 m and 5 m spatial resolution, respectively. The three time periods are indicated at the top: day (2019-07-25 12:00 to 20:50 CEST and 2019-07-26 08:10 to 14:00 CEST), night (2019-07-25 21:00 to 2019-07-26 05:50 CEST), and morning transition (MT) (2019-07-26 06:00 to 08:00 CEST). Plots (d), (e), and (f) show a close up of the MT period for the Birken, Markt, and Mistel station, respectively.

Temperature changes can also stem from changes in the turbulent sensible heat flux, which is part of the energy balance equation (Chapter 2.3). At the Markt station (Fig. 31b), the energy fluxes at the 5 m spatial resolution were weaker than at the 20 m spatial resolution because the energy availability Q_S^* was lower due to a shading situation at the 5 m spatial resolution seen in Figure 29b. The large differences between the spatial resolutions at the Mistel station (Fig. 31c) stemmed from the different surface cover types. The latent heat flux for the 5 m spatial resolution during the day was much stronger than at the other measurement stations because of the vegetated surface cover which typically shows higher latent heat fluxes than sealed surfaces (Chapter 2). Contrary, the ground heat flux at the vegetated surface was much lower because of a lower diffusivity of vegetated surfaces compared to the water surface (Tab. 4). For the 20 m spatial resolution at the Mistel station (Fig. 31c), the sensible heat flux was constantly negative, meaning that heat was transported from the atmosphere towards the water surface. This happened because the water temperature was constant at 18.8 ℃, which is much lower than the air temperature above the surface. Minimum air temperature of this grid cell was 23.4 ℃ and the mean temperature over the whole study period was 30.4 ℃. The LfU (2023) indicated the measured water temperature of the Rotmain river between 21.3 ℃ and 27.1 ℃ during the time of the study period. This suggests that the set 18.8 ℃ water temperature was set too low, exaggerating the temperature difference between the water surface and the air above. The model offset this large temperature difference by transporting energy from the surface into the ground resulting in an extremely large ground heat flux of up to 813 $W\,m^{-2}$ for the water surface (blue line in Fig. 31c).

Also, the ground heat fluxes at the Birken and Markt stations, which are covered by pavement, were strikingly high. Urban areas are characterized by large ground heat fluxes (Chapter 2.3). However, the ground heat flux exceeded the sensible heat flux by up to over 1300 % which seems overestimated. This high ground heat flux means that during the day, the majority of the available energy was transported into the ground. During the night, the energy deficit at the surface generated by net radiative cooling was mostly compensated by the ground heat flux. Therefore, less energy was available for the sensible heat flux resulting in a small sensible heat transport from the atmosphere to the surface during the night. This represents an explanation for the underestimated modeled nighttime temperature decrease during the night, which was observed in Figure 15.

An overestimated ground heat flux can also explain the delay in the temperature increase after sunrise. The closeup of the morning transition period in Figure 31d-f showed that the energy deficit after sunrise was still mainly compensated by the ground heat flux. The sensible heat flux only slowly increased with sunrise and became increasingly larger when the ground heat flux and the net all-wave radiation change sign at around 2019-07-26 08:00 CEST. This means, from 2019-07-26 08:00 CEST onward net heat was transported from the surface to atmosphere. This warmed the air above the ground and explains the increase in air temperature from 2019-07-26 08:00 CEST onward (Fig. 15).

An explanation for the overestimation of the ground heat flux of the model and a subsequent underestimation of the sensible heat flux could be an overestimated thermal diffusivity of the ground. Thermal diffusivity describes how easily heat is conducted through the ground (Oke et al., 2017). An indication for an overestimated thermal diffusivity was the high responsiveness of the ground heat flux to the net energy flux shown by a close mirroring of both fluxes as seen in Figure 31. However, the thermal diffusivity values of different surface cover types used in the simulation (Tab. 4) agreed with values found in common literature or were even lower.

Table 4: Thermal diffusivity values of different surface cover types as used in the PALM-4U simulation. The thermal diffusivity has been calculated with thermal conductivity k and heat capacity C according to Equation 4. Input values for Equation 4 were taken from the PALM-4U documentation of land surface parameters (PALM LSP, 2023). A description of the calculation of these values is found in the appendix (Chapter A.2).

surface cover type	thermal diffusivity ($m^2 s^{-1} \cdot 10^{-6}$)
pavement (asphalt)	$0.39 \cdot 10^{-6}$
pavement (stone)	$0.52 \cdot 10^{-6}$
vegetation (short grass)	$0.02 \cdot 10^{-6}$
water	$0.14 \cdot 10^{-6}$

The value for asphalt ($0.39 \cdot 10^{-6}\,\mathrm{m^2\,s^{-1}}$) lays at the lower end of the typical ranges from 0.38 to $1.7 \cdot 10^{-6}\,\mathrm{m^2\,s^{-1}}$ (Oke et al., 2017; Pan et al., 2017; Vo et al., 2015). Typical diffusivity values for stone are between 0.64 and $1.21 \cdot 10^{-6}\,\mathrm{m^2\,s^{-1}}$ (Andújar Márquez et al., 2016; Elmannaey et al., 2012; Oke et al., 2017), exceeding the thermal diffusivity of stone in the model ($0.52 \cdot 10^{-6}\,\mathrm{m^2\,s^{-1}}$). The few references indicating values for vegetation cover exceed the here applied value for vegetation of $0.02 \cdot 10^{-6}\,\mathrm{m^2\,s^{-1}}$ significantly. Yaghoobian et al. (2010) indicates $0.39 \cdot 10^{-6}\,\mathrm{m^2\,s^{-1}}$ as a typical thermal diffusivity of grass cover, while Jayalakshmy and Philip (2010) indicates 0.13 to $0.58 \cdot 10^{-6}\,\mathrm{m^2\,s^{-1}}$ for different vegetation types. Only the diffusivity value of water ($0.14 \cdot 10^{-6}\,\mathrm{m^2\,s^{-1}}$) agrees well with the common literature (Gartland, 2011; Oke et al., 2017). Despite the general agreement of the thermal diffusivity values set in the model and the literature values, the high responsiveness of the ground heat flux hints at an overestimation of the thermal diffusivity nevertheless.

The overestimation of the ground heat flux could also be explained by the omitted spin-up period. Without conducting a spin-up period prior the main simulation, a proper initialization of the surface layer temperature could have been prevented. The temperature gradient between the surface and the air above drives the sensible heat flux while the temperature gradient between the surface and the soil below drives the ground heat flux. A missing initialization of a realistic surface layer temperature could therefore have caused unrealistic temperature gradients and subsequent misestimated heat fluxes.

Another explanation for the overestimation of the nighttime temperature would be an overestimation of the modeled turbulent kinetic energy (TKE). During nighttime, an overestimated turbulence would mix warmer air at higher levels with colder air at the ground level, leading to overestimated air temperatures at the ground during night, as observed in Figure 15. However, a thorough analysis of the modeled TKE would be necessary to support this explanation.

The third term of Equation 14 which impacts the change of air temperature in an Eulerian air parcel is heat advection. Advection is the transport of heat, mass or momentum by the mean wind. A temperature increase of a volumetric air parcel through advection occurs if more heat is transported into the parcel than leaves the parcel. To analyze heat advection, the air temperature and the wind velocity components of the grid cells surrounding the measurement stations would need to be analyzed. A thorough analysis of advection was out of the scope of this thesis. This applies for heat advection as well as moisture advection. In the following, advection will be named as a possible impact factor if applicable, but a deeper analysis was not performed.

6.2 Underestimated modeled specific humidity

Figure 17 showed that the modeled specific humidity was mostly underestimated and that its timely course deviated from the course of the observed specific humidity. The humidity in the model was derived from the output of COSMO-DE2 specific humidity which served as input boundary data to the model. Figure 32 shows that the modeled specific humidity followed the course of the COSMO-DE2 specific humidity and that the noted fluctuations after 2019-07-25 16:00 CEST occurred also in the COSMO-DE2 data. This means that the model followed the external forcing well.

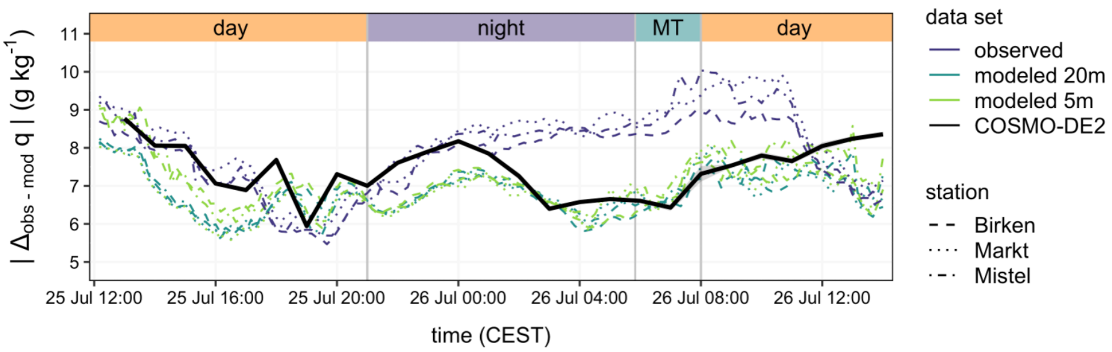

Figure 32: Time series of specific humidity (g kg^{-1}). The black line and the grey shading represent the mean and the standard deviation of the COSMO-DE2 specific humidity, respectively. The mean was taken over all four root domain boundaries (north, east, south, west) at the second and third layer where the measurement stations were located. The other lines represent the observed and measured specific humidity as seen in Figure 15 (see there for further description). The three time periods are indicated at the top: day (2019-07-25 12:00 to 20:50 CEST and 2019-07-26 08:10 to 14:00 CEST), night (2019-07-25 21:00 to 2019-07-26 05:50 CEST), and morning transition (MT) (2019-07-26 06:00 to 08:00 CEST).

The humidity of an Eulerian air parcel can change through advection or turbulence which transports more or less humid air into or out of the parcel (Eq. 17). Latent energy associated with water vapor is transported by the turbulent latent heat flux Q_E from the surface into the air above. As seen in Figures 31a and b, the latent heat flux at the Birken and Markt station stayed zero over the whole study period, which can be explained by the sealed surface covers and a subsequent absence of water availability at both measurement stations. Only at the Mistel station (Fig. 31c), positive turbulent latent heat fluxes occurred. At the 20 m spatial resolution, the latent heat flux stayed mostly constant at around 65 W m^{-2} because the water surface cover supplied the necessary water availability for the latent heat flux. However, due to the constant water temperature of 18.8 °C, the available energy stayed rather constant during the diurnal course. Also, the vegetated surface cover below the grid cell at the 5 m spatial resolution at the Mistel station provided moisture, leading to a positive latent heat flux transporting humidity upwards. This flux was larger during the day because more energy was available due to higher daytime surface temperatures (Fig. A.4 in the appendix). However, while the turbulent fluxes differed between the measurement stations and surface cover types, the specific humidity behaved similarly at all measurement stations and surface covers (Fig. 16). The observed patterns in Figure 16 can therefore not be explained by the turbulent latent heat fluxes at the surface.

The second term of Equation 17 is horizontal moisture advection. Moisture advection is the transport of humidity by the mean wind. An increase in humidity of an air parcel occurs if more moisture enters the parcel via advection than leaves the parcel. As stated above, advection was not further analyzed in this thesis.

6.3 Relation of modeled wind speed and building height

For wind speed, deviations between the modeled and observed data were found. The modeled wind speed exceeded the observed wind speed during the evening of day one by up to 3.8 $m\,s^{-1}$. An increase in modeled wind speed was observed between 2019-07-25 22:00 and 2019-07-26 03:00 CEST which was not noted in the observed data. On day two the differences between the observed and modeled wind speed were notable smaller with a mean difference of 0.1 $m\,s^{-1}$ across all measurement stations and spatial resolutions. The boundary input of wind speed, which was derived from the COSMO-DE2 output, provides an explanation for the discrepancy between the modeled and the observed wind speeds (Fig. 33). Like the modeled wind speed, the COSMO-DE2 wind speed was higher between 2019-07-25 16:00 and 20:00 CEST and 2019-07-25 22:00 and 2019-07-26 04:00 CEST. Interestingly, the COSMO-DE2 wind speeds increased sharply after 2019-07-26 09:00 CEST and reached 4.5 $m\,s^{-1}$ at the end of the study period while the observed and modeled wind speeds only increased slightly and at a similar course towards the end of the study period. That the simulation was run without a spin-up period might explain the decreasing model-observation differences over time as the material layers were not sufficiently set up at the beginning of the study period (Chapter 6.1). At all time steps except two, the COSMO-DE2 wind speeds were higher than the modeled wind speeds. This was expected because there were less roughness elements at the root domain's borders, where the COSMO-DE data was input, than within the child domain. The simulation done by the PALM-4U model was expected to decrease the wind speeds according to the larger amount of roughness elements within the study area. This process seemed to serve as an explanation for the 5 m spatial resolution at Birken and for both spatial resolutions at the Markt station, which all showed lower modeled wind speeds and therefore lower differences between modeled and observed wind speed (Fig. 17). However, for the other measurement stations and spatial resolutions, the modeled wind speeds seemed to be less well influenced by the the local roughness elements as they followed the COSMO-DE2 output more closely, especially showing overestimated wind speeds and the decrease after midnight.

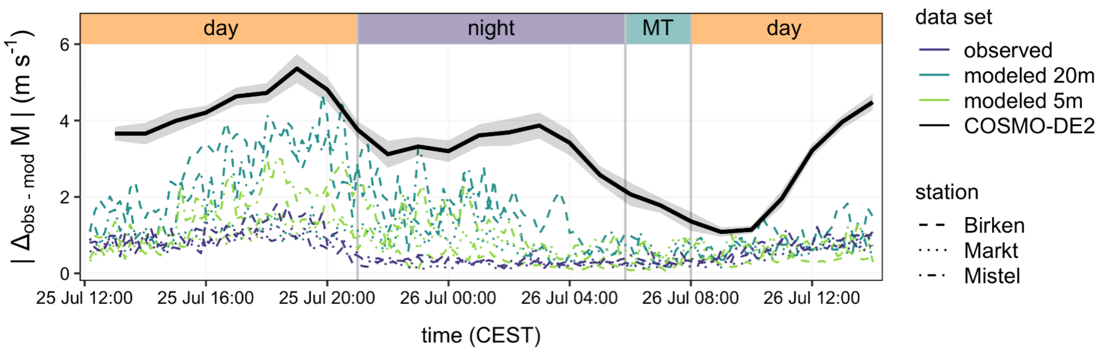

Figure 33: Time series of wind speed (m s^{-1}). The black line and the grey shading represent the mean and the standard deviation of the COSMO-DE2 wind speed, respectively. The mean was taken over all four root domain boundaries (north, east, south, west) at the second and third layer where the measurement stations were located. The other lines represent the observed and measured wind speed as seen in Figure 17 (see there for further description). The three time periods are indicated at the top: day (2019-07-25 12:00 to 20:50 CEST and 2019-07-26 08:10 to 14:00 CEST), night (2019-07-25 21:00 to 2019-07-26 05:50 CEST), and morning transition (MT) (2019-07-26 06:00 to 08:00 CEST).

Why at some measurement stations and spatial resolutions the modeled wind speed was closer to the COSMO-DE2 wind speed while at other measurement stations the wind speed was more influenced by the local roughness elements can be explained by how accurate the local surface structure was represented in the model. For all three measurement stations, the surface height of the 5 m spatial resolution was a closer representation of the actual surface structure (Fig. 5) as most of the buildings and surface structures were visible (Fig. 12). Figures 34d-f show clearly that the wind was channeled through the street canyons at the height of the measurement station for the 5 m spatial resolution. On the other hand, the 20 m spatial resolution (Fig. 34a-c) showed less obstacles and urban structures resulting in less deflected, higher wind speeds. The differences between the representation of the surface structure of both spatial resolutions were especially large at the Birken station (Fig. 34a,d). At the 5 m spatial resolution, single street canyons and building structures were visible, leading to a channeled air flow. In contrast, the modeled surface height at the 20 m spatial resolution was mostly flat with only a few higher obstacles and a lower section in the north (Fig. 34d). Therefore, the wind was less slowed by roughness elements, which explains the larger difference between the observed and modeled wind speed for the 20 m spatial resolution but the smaller difference for the 5 m spatial resolution at the Birken station.

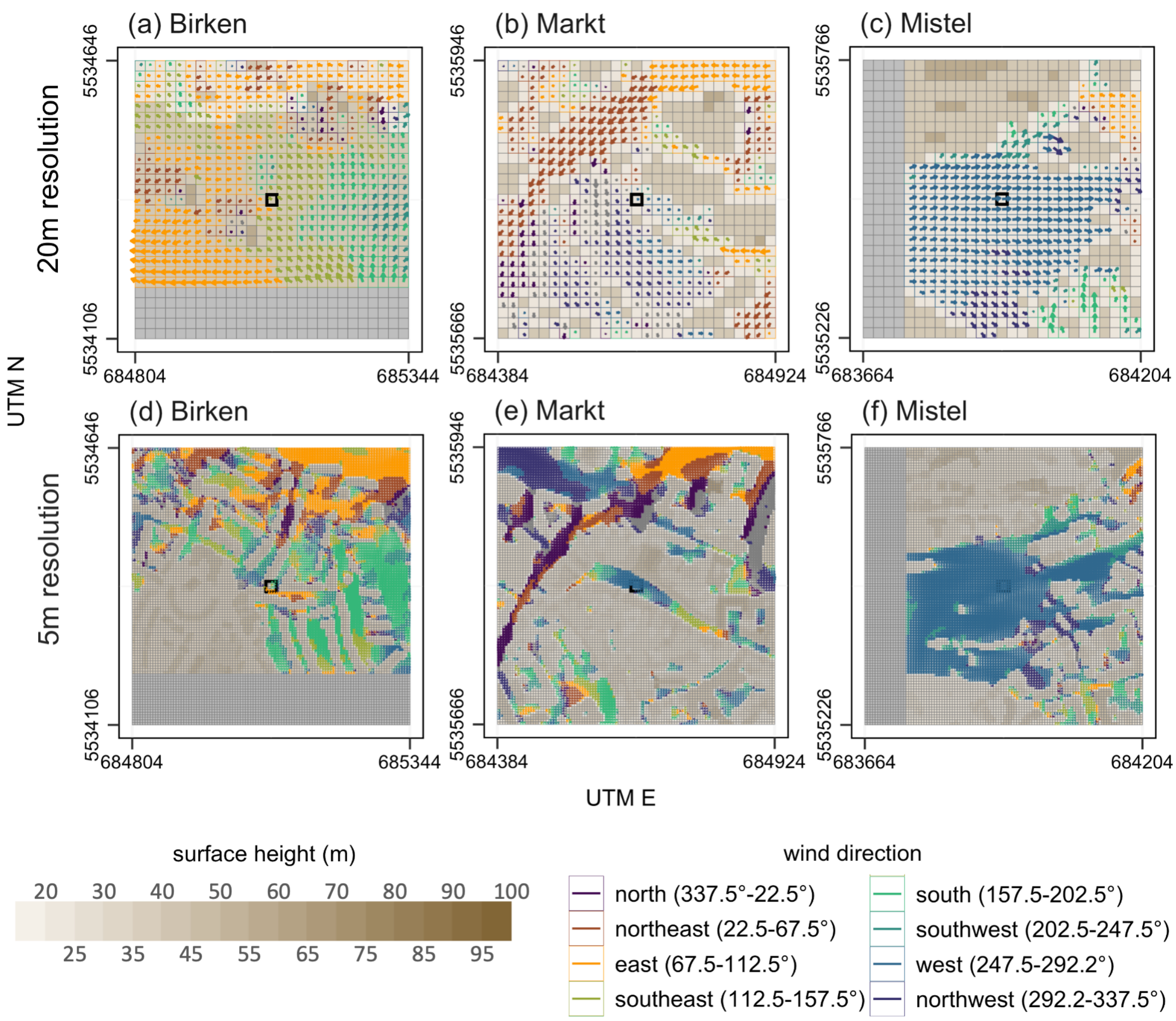

Figure 34: Horizontal cross sections showing the first grid layer above the surface in a square with a side length of 260 m centered at the measurement location of the Birken station (a+d), the Markt station (b+e), and the Mistel station (c+f). The top row shows data at the 20 m spatial resolution while the bottom row shows data at the 5 m spatial resolution. The grid colors represent the modeled surface height in m, i.e., the height of the first 100 % fluid grid cell. The black squares show the location of the 20 grid cell covering the respective measurement station. The arrows represent the velocity components at the respective z layer of the measurement stations' position. The Birken station is located on z layers 3 and 5 for the 20 and 5 m spatial resolution, respectively (compare Tab. 3). Both, Markt and Mistel station are located on z layer 2 and 3 or the 20 and 5 m spatial resolution, respectively. The direction and color of the arrows represent the wind direction. The figure shows the modeled output at 2019-07-26 07:00 CEST.

For the Markt and the Mistel stations, the differences between the modeled surface structure of the 20 m and the 5 m spatial resolution were smaller than at the Birken station. Despite that less obstacles are represented at the 20 m spatial resolution of the Markt station (Fig. 34b), the street canyon of the Maximilianstraße, in which the measurement station was located, was visible. The air flow was channeled into the street canyon and the speed was slowed down, leading to low differences between the observed and modeled wind speeds for both spatial resolutions. The Mistel station was surrounded by mostly vegetation and water and no near-by houses within a 13 m radius (figure in Tab. 1). This was well represented in both spatial resolutions which showed no close-by obstacles and a mostly flat surface which led to an unhindered air flow and explained the lower differences between the spatial resolutions (Fig. 34c,f). However, as the photo in Table 1 shows, there were close-by trees and bushes which were smaller than 5 m and were therefore not included in the static driver. Thus, these obstacles can still have an effect of slowing down the wind speed measured at the measurement station, which can explain the larger but similar $\Delta_{obs-mod\_20m}$ and $\Delta_{obs-mod\_5m}$ at the Mistel station compared to the other measurement stations.

The gathered information supports the rejection of hypothesis 2. The differences between the observed and modeled wind speeds are not explained by the building height heterogeneity surrounding the measurement stations but rather by how well the surface structure was represented in the model. The more accurate the actual surface structure was represented, the smaller were the differences between observed and modeled wind speeds. Also, the wind speed differences between the 20 m and 5 m spatial resolution can be better explained by the accuracy of modeled surface representation rather than the building height heterogeneity (hypothesis 4). How well the surface structure is represented in the model, depends on the height of the single obstacles. As described in Chapter 4.3, the modeled surface height was calculated by approximating the building or topography height to the nearest grid level. This means, that only buildings with a height taller than the spatial resolution are represented in the model with certainty. Whether smaller buildings were represented, depended on the underlying topography height and the bottom domain height. The majority (63 %) of the buildings in the study area were taller than 5 m but smaller than 20 m and were therefore well represented in the 5 m spatial resolution and less well represented in the 20 m spatial resolution (Fig. 12). As the individual roughness elements, i.e., buildings, were not represented well in the 20 m spatial resolution, the wind flowed mostly unhindered at higher speeds. At the 5 m spatial resolution, the wind was slowed by the represented buildings, explaining the overall lower wind speeds in the 5 m spatial resolution. Only at open fields, the surface representation of both spatial resolutions was similar as no buildings or obstacles were present. Here, the spatial resolution differences of wind speed were small (Fig. 21c).

Relating spatial resolution differences of wind speed to the surface representation also explains the results of the vertical cross section. The spatial resolution differences in the RSL were decisively larger than the differences in the higher UBL (Fig. 27c). In the RSL, where the wind speed is highly influenced by the surface structure, the spatial resolution differences in the surface structure led to larger differences between the modeled wind speeds in the two spatial resolutions. At higher layers of the urban boundary layer, the wind speed was less influenced by the surface so the differences between the spatial resolutions were smaller. Finally, it can be concluded that in areas and at spatial resolutions where the surface structure was represented well in the model, the difference between observed and modeled wind speeds as well as the differences between the modeled wind speeds at both spatial resolutions were smaller than at areas and spatial resolutions where the surface structure was not represented well.

6.4 Spatial resolution differences of temperature and humidity

Spatial temperature and humidity differences are offset by heat and humidity transport down the gradient thriving for a thermal and moisture equilibrium (Stull, 2017). With an overestimated modeled TKE, the mixing of air would also be overestimated causing more homogeneous temperature and moisture profiles. This could explain why temperature and humidity differences between the measurement stations were small and non-decisive. The influence of building height and surface structure on spatial resolution differences of temperature and humidity was found to be negligible. However, decisive difference between a low land cover heterogeneity and medium or high heterogeneity has been found for the water vapor mixing ratio (Fig. 25b).

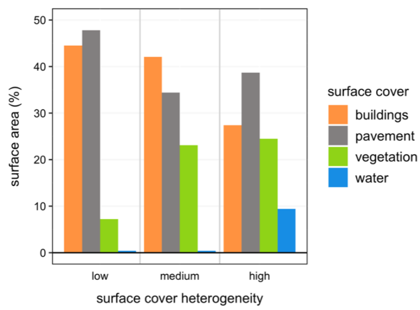

Figure 35: Share of surface cover types of areas with low, medium, and high surface cover heterogeneity (in %).

From Figure 35 it became apparent that the three heterogeneity classes also differed in terms of the surface cover types they comprise. While the low heterogeneity class consisted of over 90 % sealed surface types, the medium and high heterogeneity class comprised 24 % and

34 % vegetated and water surface covers, respectively. Therefore, it can be argued that the decisive difference between $\Delta_{5-20m}\ m$ at different heterogeneity classes did not stem from the heterogeneity itself but rather from the type of surface cover at these areas.

The water vapor mixing ratio above vegetation and water surfaces was decisively lower at the 20 m than the 5 m spatial resolution (Fig. 36). According to Equation 17, the water vapor mixing ratio of an Eulerian air parcel above the surface can change due to horizontal moisture advection and the vertical turbulent moisture flux divergence. Regarding the latter, the humidity of the air parcel increases if the ingoing moisture flux exceeds the outgoing moisture flux. Above vegetation and water surfaces, a positive turbulent latent heat flux was observed (Fig. 31c) indicating that moisture was transported upwards from the surface. As the modeled quantities were defined at the grid cell center (Fig. 11), the output of the 5 m spatial resolution was given closer to the ground than for the 20 m spatial resolution. In concrete numbers this means, that for the first 5 m grid cell above the surface, the output height was at 2.5 m above the surface while for the 20 m spatial resolution the output was given at 10 m above the surface. Being further away from the surface, the water vapor mixing ratio at the 20 m spatial resolution was less influenced by moisture availability at the surface and the subsequent vertical moisture transport. This can explain the found decisive spatial resolution difference for water vapor mixing ratio above vegetation and water surfaces (Fig. 36a).

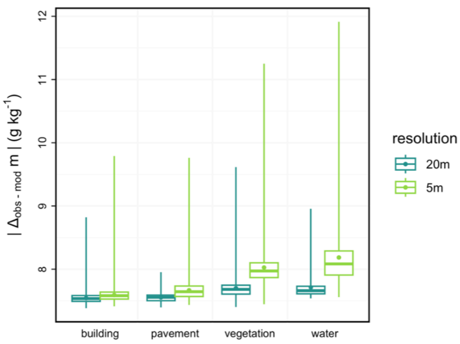

Figure 36: Box plots of the (a) modeled potential temperature θ (K) and (b) water vapor mixing ratio m (g kg^{-1}) above different surface cover types. Dark green plots represent data at the 20 m spatial resolution and light green plots represent data at the 5 m spatial resolution. The upper and lower border of the boxes mark the 75th and 25th percentile, respectively, while the lowest and highest values are depicted at the bottom and top end of the whiskers, respectively. The horizontal line in box represents the median and the dot is the position of the data set's mean.

A decisive difference in water vapor mixing ratio between the spatial resolutions was not observed above buildings and paved surfaces (Fig. 36). Above sealed surfaces, the turbulent latent heat flux was found to be zero over the course of the study period (Fig. 31c). Therefore, the water vapor mixing ratio above these surfaces could not be impacted by a vertical turbulent moisture flux divergence. This leaves horizontal moisture advection as a driver for the water vapor mixing ratio (Eq. 17) which was not analyzed in this thesis.

7 Conclusion

In this thesis, a simulation of the LES model PALM-4U was validated with an observation network, and secondly the model's spatial resolution was analyzed in a model-model comparison of two spatial resolutions (Δx,y,z = 5 and 20 m). The study area was in Bayreuth, a mid-sized city in Bavaria, Germany, and the study period covered 26 hours during a heat wave in July 2019 (2019-07-25 12:00 to 2019-07-26 14:00 CEST). A general uncertainty of the modeled data could stem from an overestimated modeled turbulent kinetic energy (TKE) and a missing spin-up period. The overestimation of TKE in meteorological simulations is a common source of uncertainty. Due to the rectangular grid in PALM-4U, horizontal and vertical surfaces of buildings and topography are sharp-edged. The thereby caused increased surface roughness enhances turbulence. Subsequently, air experiences more mixing leading to more homogeneous vertical and horizontal temperature and humidity profiles. The TKE in the modeled domain was not analyzed due to missing modeled quantities. It is recommended to include the relevant quantities in future simulations and to inspect the modeled TKE for possible overestimation.

Secondly, without conducting a spin-up period prior the main simulation, the temperature and moisture content of the surface layers might have not been initialized sufficiently. The surface temperature and moisture content have a strong impact on the meteorological processes above the surface where the model-observed comparison took place. Therefore, insufficiently initialized surface properties might be a strong cause for the found deviations between the observed and modeled values. This applies especially for the found overestimated modeled ground heat flux and a subsequent underestimated modeled sensible heat flux. The misestimation of these fluxes could explain the found overestimation of the modeled nighttime air temperature by up to 9.4 K. Including a spin-up period and a proper initialization of the surface temperature and moisture content might result in more realistic ground and sensible heat fluxes. It is therefore recommended to include a spin-up period prior the main simulation. The markedly overestimated ground heat fluxes are also suggesting an overestimated thermal diffusivity of the surface material. Despite finding that the thermal diffusivity values of the model agreed with literature values, a thorough evaluation of the accuracy of these values is recommended, especially if the ground heat flux does not adjust with a spin-up period.

The delayed morning air temperature increase by two hours was traced back to a shading event in the incoming shortwave radiation data which served as a boundary input to the model.

The radiation data was taken from the meteorological measurement station at the Ecological Botanical Garden (EBG) in Bayreuth which experienced a shading event in the early morning, reducing the incoming shortwave radiation reaching the measurement station. Therefore, it is recommended to check the incoming shortwave radiation input for local shading effects before integrating it as the model's initial boundary data.

The temporal course of modeled specific humidity showed a similar pattern to the initial boundary data of specific humidity suggesting that the model responds well to the given input data. To further explore the causes of the detected deviations between the modeled and observed specific humidity, a thorough analysis of advection should be performed. The modeled advection was not analyzed as it was out of the scope of this thesis. Nevertheless, advection is a crucial factor not only for humidity but also for temperature changes and might provide further insights on model-observation differences.

By analyzing the wind speed, it was found that at areas in which the surface structure was represented well in the model, the model-observed differences were smaller while the differences were larger at areas where the actual surface structure was not visible in the modeled surface. How well the surface structure was represented in the model depends on the building height and the chosen spatial resolution. Buildings and topography height differences which were smaller than the chosen spatial resolution were represented well, while obstacles taller than the spatial resolution were not always represented. Therefore, choosing a spatial resolution smaller than the height of most buildings and obstacles could lead to a more accurate simulation of the wind speed. In areas without buildings or obstacles, the differences between the spatial resolutions were small. Lower model-observation differences of wind speed have been found for the second part of the study period at all measurement stations ($\Delta_{obs-mod}\ \overline{M}$ = 0.1 $m\,s^{-1}$). This could indicate that the simulation improves over time and that simulating a spin-up period preceding the main model run could lead to improved modeled results from the start of the study period.

Substantially higher water vapor mixing ratios above vegetation and water surfaces for the 5 m spatial resolution compared to the 20 m spatial resolution could be explained by smaller distance to the surface of the output position at the 5 m than the 20 m spatial resolution. The output of the near-surface grid cell at the 5 m spatial resolution was defined at 2.5 m while the 20 m spatial resolution was defined at 10 m above the surface. Above sealed surfaces the turbulent latent heat flux was found to be zero as no moisture was available at the surfaces.

The water temperature in the simulation was found to be defined too cool leading to constant negative sensible heat fluxes above water surfaces and an exaggerated ground heat flux. It is therefore recommended to increase the modeled water temperature to a more realistic temperature between 21.3 ℃ and 27.1 ℃ for the time of the study period. Further, making the modeled water temperature variable over the course of the day like it is the case for the surface temperature of other cover types might enhance the results.

The aim of this thesis was to identify possible enhancements to the PALM-4U model. This thesis provided a number of recommendations through which the simulation results are expected to become more accurate. How the suggested alternation actually affect the simulated output should be tested before formulating recommendations for city planning based urban development scenarios simulated with PALM-4U. The number of recommendations does not claim to be exhaustive and fields of further analysis have been pointed out. With the discussed results and concluding recommendations, this thesis hopes to contribute to an enhanced application of the PALM-4U model.

References

Andújar Márquez, J., Martínez Bohórquez, M., & Gómez Melgar, S. (2016). Ground thermal diffusivity calculation by direct soil temperature measurement. Application to very low enthalpy geothermal energy systems. *Sensors*, *16*(3), 306. https://doi.org/10.3390/s16030306

Angevine, W. M., Klein Baltink, H., & Bosveld, F. C. (2001). Observations of the morning transition of the convective boundary layer. *Boundary-Layer Meteorology*, *101*, 209–227. https://doi.org/10.1023/A:1019264716195

Bayerische Vermessungsverwaltung. (2018). *Tatsächliche Nutzung (Kreisfreie Stadt Bayreuth)* [Lizenz cc by 4.0 (https://creativecommons.org/licenses/by/4.0/deed.de)]. www.geodaten.bayern.de

BBSR. (2017). *Laufende Stadtbeobachtung - Raumabgrenzungen*. Bundesinstitut für Bau-, Stadt- und Raumforschung. Retrieved March 21, 2023, from https://www.bbsr.bund.de/BBSR/DE/forschung/raumbeobachtung/Raumabgrenzungen/deutschland/gemeinden/StadtGemeindetyp/StadtGemeindetyp.html

Beare, R. J. (2008). The role of shear in the morning transition boundary layer. *Boundary-Layer Meteorology*, *129*(3), 395–410. https://doi.org/10.1007/s10546-008-9324-8

Brandsma, T., & Wolters, D. (2012). Measurement and statistical modeling of the urban heat island of the city of Utrecht (the netherlands). *Journal of Applied Meteorology and Climatology*, *51*(6), 1046–1060. https://doi.org/10.1175/JAMC-D-11-0206.1

Cardoso, R., Dorigon, L., Teixeira, D., & Amorim, M. (2017). Assessment of urban heat islands in small- and mid-sized cities in Brazil. *Climate*, *5*(1), 14. https://doi.org/10.3390/cli5010014

Cheng, H., & Castro, I. P. (2002). Near wall flow over urban-like roughness. *Boundary-Layer Meteorology*, *104*, 229–259. https://doi.org/10.1023/A:1016060103448

Djongyang, N., Tchinda, R., & Njomo, D. (2010). Thermal comfort: A review paper. *Renewable and Sustainable Energy Reviews*, *14*(9), 2626–2640. https://doi.org/10.1016/j.rser.2010.07.040

Elmannaey, A. S., El-Nahhas, F. M., & El-Mossallamy, Y. (2012). Experimental and analytical investigation of the effect of groundwater flow on the thermal characteristics of soil. *ZEC Infrastructure 2012*. https://doi.org/10.13140/2.1.4085.6969

Foken, T. (2017). *Micrometeorology*. Springer Berlin Heidelberg. https://doi.org/10.1007/978-3-642-25440-6

Gartland, L. (2011). *Heat islands: Understanding and mitigating heat in urban areas*. Earthscan. https://doi.org/10.4324/9781849771559

Geiger, R., Aron, R. H., & Todhunter, P. (2009). *The climate near the ground* (7th ed.). Rowman & Littlefield Publishers, Inc. https://doi.org/10.1007/978-3-322-86582-3

GeoBasis-DE/BKG. (2022). *NUTS-Gebiete 1:250 000, Stand 31.12.* [Dl-de/by-2-0 (www.govdata.de/dl-de/by-2-0)]. Retrieved November 10, 2022, from http://www.bkg.bund.de

Graham, E. (1993). The urban heat island of Dublin city during the summer months. *Irish Geography*, *26*(1), 45–57. https://doi.org/10.1080/00750779309478717

Gronemeier, T., Surm, K., Harms, F., Leitl, B., Maronga, B., & Raasch, S. (2021). Evaluation of the dynamic core of the PALM model system 6.0 in a neutrally stratified urban environment: Comparison between LES and wind-tunnel experiments. *Geoscientific Model Development*, *14*(6), 3317–3333. https://doi.org/10.5194/gmd-14-3317-2021

Howard, L. (1833). *The climate of London: Deduced from meteorological observations made in the metropolis and at various places around it (vol. 3).* Harvey and Darton; J. and A. Arch; Longman and Co.; Hatchard and Son; S. Highley; R. Hunter.

Hung, T., Uchihama, D., Ochi, S., & Yasuoka, Y. (2006). Assessment with satellite date of the urban heat island effects in Asian mega cities. *International journal of applied Earth observation and Geoinformation*, *8*(1), 34–48. https://doi.org/10.1016/j.jag.2005.05.003

IPCC. (2021). Summary for policymakers: In: Climate change 2021: The physical science basis. [Contribution of working group i to the sixth assessment report of the intergovernmental panel on climate change]. *Intergovernmental Panel on Climate Change*.

Jauregui, E. (1997). Heat island development in Mexico City. *Atmospheric Environment*, *31*(22), 3821–3831. https://doi.org/10.1016/S1352-2310(97)00136-2

Jayalakshmy, M. S., & Philip, J. (2010). Thermophysical properties of plant leaves and their influence on the environment temperature. *International Journal of Thermophysics*, *31*(11-12), 2295–2304. https://doi.org/10.1007/s10765-010-0877-7

Kim, Y.-H., & Baik, J.-J. (2002). Maximum urban heat island intensity in Seoul. *Journal of Applied Meteorology and Climatology*, *41*(6), 651–659. https://doi.org/10.1175/1520-0450(2002)041<0651:MUHIII>2.0.CO;2

LfStat. (2019). *Genesis-Online Datenbank*. Bayerisches Landesamt für Statistik. https://www.statistikdaten.bayern.de

LfU. (2023). *Wassertemperatur: Aktuelle Messwerte Bayreuth / Roter Main*. Bayerisches Landesamt für Umwelt. Retrieved February 22, 2023, from https://www.gkd.bayern.de/de/fluesse/wassertemperatur/elbe/bayreuth-24123000/messwerte?zr=woche&beginn=25.07.2019&ende=26.07.2019

Li, D., & Bou-Zeid, E. (2013). Synergistic interactions between urban heat islands and heat waves: The impact in cities is larger than the sum of its parts. *Journal of Applied Meteorology and Climatology*, *52*(9), 2051–2064. https://doi.org/10.1175/JAMC-D-13-02.1

Li, X., Zhou, Y., Asrar, G. R., Imhoff, M., & Li, X. (2017). The surface urban heat island response to urban expansion: A panel analysis for the conterminous United States. *The Science of the total environment*, *605-606*, 426–435. https://doi.org/10.1016/j.scitotenv.2017.06.229

Liu, Z., He, C., Zhou, Y., & Wu, J. (2014). How much of the world's land has been urbanized, really? A hierarchical framework for avoiding confusion. *Landscape Ecology*, *29*, 763–771. https://doi.org/10.1007/s10980-014-0034-y

Maronga, B., Banzhaf, S., Burmeister, C., Esch, T., Forkel, R., Fröhlich, D., Fuka, V., Gehrke, K. F., Geletič, J., Giersch, S., Gronemeier, T., Groß, G., Heldens, W., Hellsten, A., Hoffmann, F., Inagaki, A., Kadasch, E., Kanani-Sühring, F., Ketelsen, K., . . . Raasch, S. (2020). Overview of the PALM model system 6.0. *Geoscientific Model Development*, *13*, 1335–1372. https://doi.org/10.5194/gmd-13-1335-2020

Maronga, B., Gross, G., Raasch, S., Banzhaf, S., Forkel, R., Heldens, W., Kanani-Sühring, F., Matzarakis, A., Mauder, M., Pavlik, D., Pfafferott, J., Schubert, S., Seckmeyer, G., Sieker, H., & Winderlich, K. (2019). Development of a new urban climate model based on the model PALM – Project overview, planned work, and first achievements. *Meteorologische Zeitschrift*, *28*(2), 105–119. https://doi.org/10.1127/metz/2019/0909

Maronga, B., Gryschka, M., Heinze, R., Hoffmann, F., Kanani-Sühring, F., Keck, M., Ketelsen, K., Letzel, M. O., Sühring, M., & Raasch, S. (2015). The parallelized Large-Eddy Simulation model (PALM) version 4.0 for atmospheric and oceanic flows: Model formulation, recent developments, and future perspectives. *Geoscientific Model Development*, *8*, 2515–2551. https://doi.org/10.5194/gmd-8-2515-2015

Martilli, A., & Santiago, J. L. (2009). How to use computational fluid dynamics models for urban canopy parameterizations. In A. Baklanov, C. Grimmond, M. Alexander, & M. Athanassiadou (Eds.), *Meteorological and air quality models for urban areas* (pp. 31–37). Springer Berlin Heidelberg. https://doi.org/10.1007/978-3-642-00298-4_4

Meade, R. D., Akerman, A. P., Notley, S. R., McGinn, R., Poirier, P., Gosselin, P., & Kenny, G. P. (2020). Physiological factors characterizing heat-vulnerable older adults: A narrative review. *Environment international*, *144*, 105909. https://doi.org/10.1016/j.envint.2020.105909

Mills, G. (2008). Luke Howard and the climate of London. *Weather*, *63*(6), 153–157.

MiSKOR. (2021). Schlussbericht zum Forschungsvorhaben Minderung Städtischer Klima- und OzonRisiken (MiSKOR) (C. Thomas, C. Samimi, J. Lüers, & S. O. Nabavi, Eds.).

Oke, T. R. (1987). *Boundary layer climates* (2nd ed.). Meuthen & Co. Ltd. https://doi.org/10.4324/9780203407219

Oke, T. R., Mills, G., Christen, A., & Voogt, J. A. (Eds.). (2017). *Urban climates*. Cambridge University Press. https://doi.org/10.1017/9781139016476

PALM LSP. (2023). *PALM documentation: Land surface parameter*. Retrieved March 22, 2023, from https://palm.muk.uni-hannover.de/trac/wiki/doc/app/land_surface_parameters

PALM RP. (2023). *PALM documentation: Runtime parameter*. Retrieved March 22, 2023, from https://palm.muk.uni-hannover.de/trac/wiki/doc/app/runtime_parameters

Palme, M., & Salvati, A. (Eds.). (2021). *Urban microclimate modelling for comfort and energy studies*. Springer International Publishing. https://doi.org/10.1007/978-3-030-65421-4

Pan, P., Wu, S., Hu, X., Liu, G., & Li, B. (2017). Effect of material composition and environmental condition on thermal characteristics of conductive asphalt concrete [PII: ma10030218]. *Materials*, *10*(3), 218. https://doi.org/10.3390/ma10030218

Raabe, A., & Foken, T. (2003). Die Höhe der internen Grenzschicht im Windfeld nach einer sprunghaften Änderung der aerodynamischen Rauhigkeit der Unterlage - Beispiel Küste: In: Beiträge zur klima- und meeresforschung (F.-M. Chmielewski & T. Foken, Eds.).

Robaa, S. M. (2003). Urban-suburban/rural differences over Greater Cairo, Egypt. *Atmósfera*, *16*(3), 157–171.

Spies, I. (2019). *Urban climate just warm streets and cool parks? Investigating the variabilities of heat at street-canyon and city-wide scale in Bayreuth* (Master Thesis). University of Bayreuth. Bayreuth, Germany.

Stone, B., Vargo, J., & Habeeb, D. (2012). Managing climate change in cities: Will climate action plans work? *Landscape and Urban Planning*, *107*(3), 263–271. https://doi.org/10.1016/j.landurbplan.2012.05.014

Stull, R. B. (2017). *Practical meteorology: An algebra-based survey of atomspheric science* (v1.02b). UBC. https://doi.org/10.14288/1.0300441

Sungur, L. (2021). *Mitigating heat accumulation in a mid-size urban area: Applying micrometeorological flow-resolving simulations to assess climate effects of urban planning measures* (Master thesis). University of Bayreuth. Bayreuth, Germany.

Thomas, C. (2023). *Klimastatistiken der Messungen im botanischen Garten*. Mikrometeorology Group, University of Bayreuth. Retrieved February 24, 2023, from http://www.bayceer.uni-bayreuth.de/meteo/de/klimastati/gru/html.php?id_obj=140009

Thomas, C., Linhardt, T., Schneider, J., & Olesch, J. (2019). Field evaluation of the micro-weather station MA-4100 (ATMOS-41): Comparison of the observational device used in the trans-african hydrometeorological observatory (tahmo) against wmo-grade instruments at the ecological botanical gardens, university of bayreuth, germany (C. Thomas, Ed.). *University of Bayreuth, Mikrometeorology*.

Toparlar, Y., Blocken, B., Maiheu, B., & van Heijst, G. (2017). A review on the CFD analysis of urban microclimate. *Renewable and Sustainable Energy Reviews*, *80*, 1613–1640. https://doi.org/10.1016/j.rser.2017.05.248

UN DESA. (2019). World urbanization prospects – the 2018 revision. *United Nations, Department of Economic and Social Affairs, Population Division*.

Vo, H. V., Park, D. W., Seo, W. J., & Im, J. S. (2015). Effect of conductive filler size and type on thermal properties of asphalt mixtures. *Innovative Materials and Design for Sustainable Transportation Infrastructure*. https://doi.org/10.1061/9780784479278.001

WMO. (2021). Guide to meteorological instruments and methods of observation: Wmo-no. 8. *World Meteorological Organization*.

Yaghoobian, N., Kleissl, J., & Krayenhoff, E. S. (2010). Modeling the thermal effects of artificial turf on the urban environment. *Journal of Applied Meteorology and Climatology*, *49*(3), 332–345. https://doi.org/10.1175/2009JAMC2198.1

Zhao, L., Oppenheimer, M., Zhu, Q., Baldwin, J. W., Ebi, K. L., Bou-Zeid, E., Guan, K., & Liu, X. (2018). Interactions between urban heat islands and heat waves. *Environmental Research Letters*, *13*(3), 034003. https://doi.org/10.1088/1748-9326/aa9f73

Acknowledgments

First and foremost, I like to thank Prof. Dr. Christoph Thomas for his valuable support during this project. He provided me with insightful feedback and advice which guided me from defining the objectives of this thesis through the analysis and to the interpretation and finalization of this work. I am truly grateful for the opportunity to have extended my knowledge about micrometeorological processes in an urban setting. Further, I like to thank Dr. Wolfgang Babel for supporting me with technical insights as well as with the interpretation of the results. A huge thanks goes to Layla Sungur for her continuous support. She patiently introduced me to the PALM-4U model and shared her extensive knowledge and experiences with me. She further conducted the PALM-4U simulations and provided me with the necessary data for this thesis. I am especially grateful that she always found time to help me with my small and large day-to-day questions and concerns. Furthermore, I would like to thank the whole Micrometeorology group for the supportive feedback and practical suggestions to my work during the biweekly meetings. This thesis is an extension to the MiSKOR project which was supported by the Bayerisches Landesamt für Gesundheit und Lebensmittelsicherheit. I highly benefited by the work and research which has been done for the MiSKOR project and therefore I like to thank everyone who contributed to this project. Overall, I like to thank everyone who supported me by contributing to my thesis in any way.

Appendix

A.1 Additional figures and tables

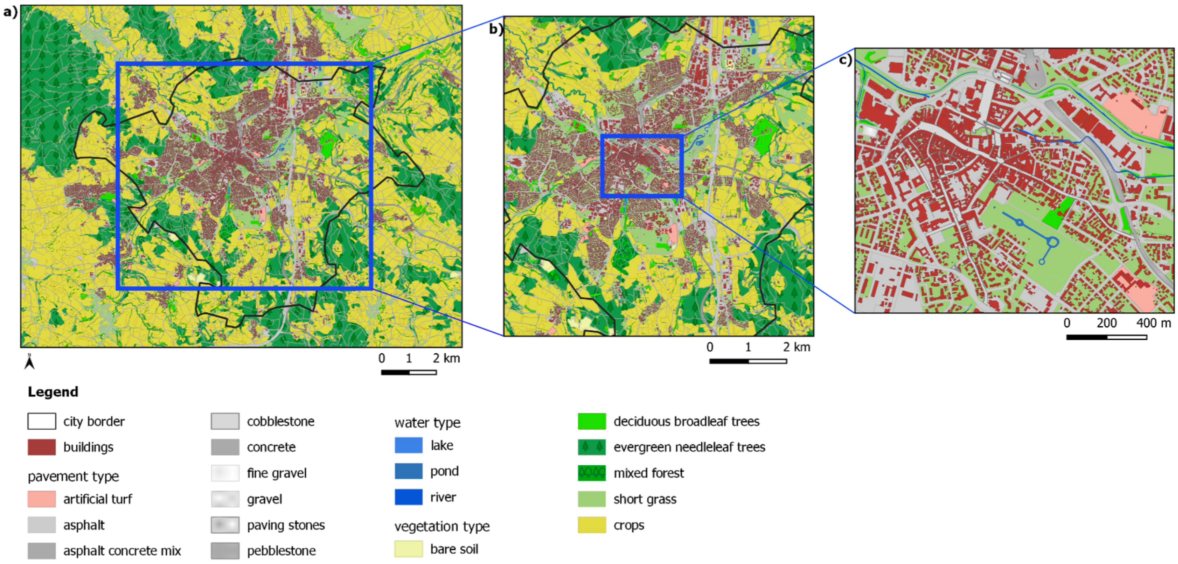

Figure A.1: Map representing the (a) root domain covering an area of 16.2 x 13.5 km encompassing the whole city of Bayreuth and (b+c) the intended inner domain by Sungur (2021). The figure was reprinted from Sungur (2021).

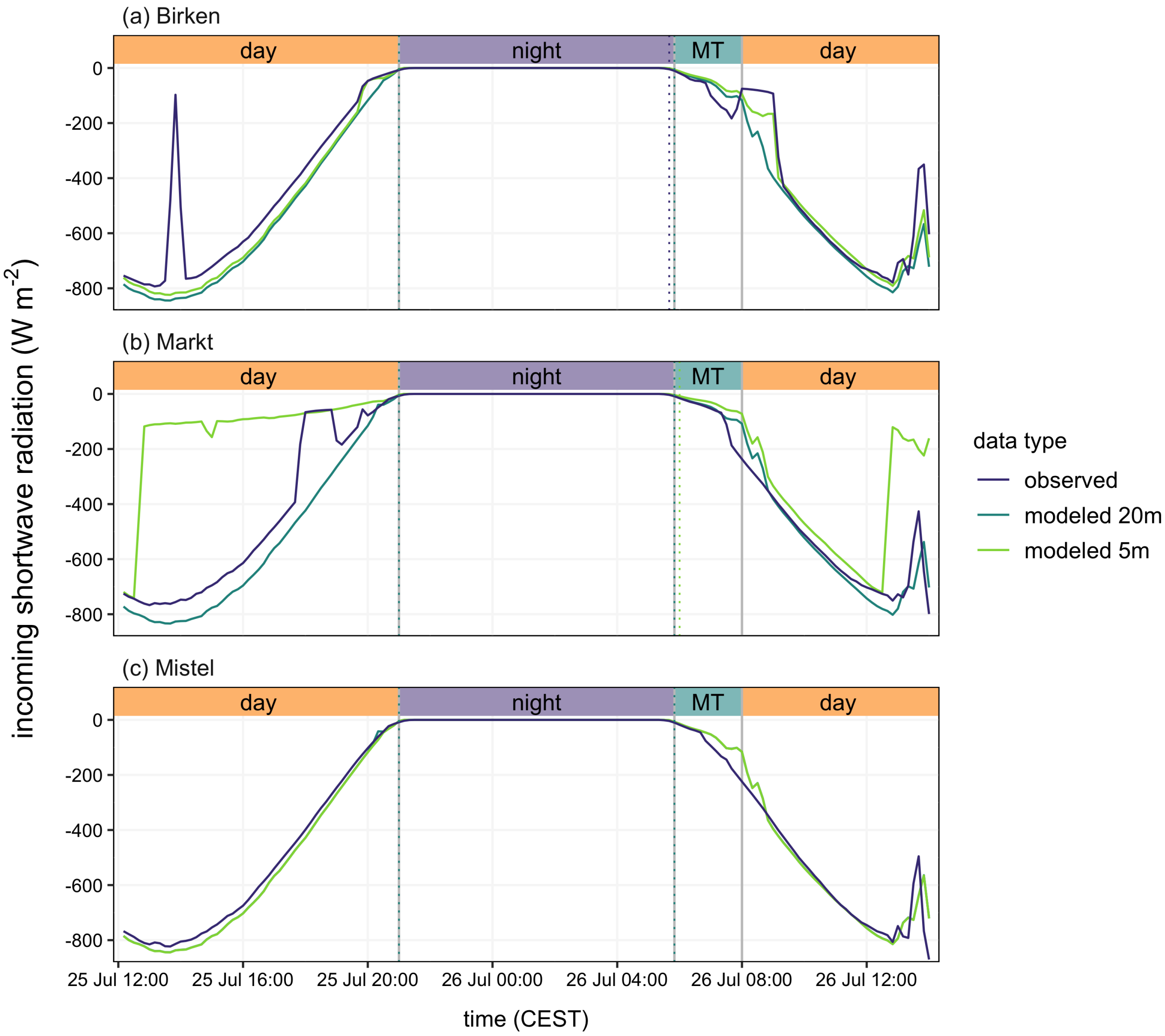

Figure A.2: Time series of incoming shortwave radiation ($W\,m^{-2}$) at the measurement stations (a) Birken, (b) Markt, and (c) Mistel. Observed values are purple and measured at a height of 3.5 m. Modeled values of the respective grid cell at the 20 m spatial resolution are dark green, and modeled values of the respective grid cell at the 5 m spatial resolution are light green. The three time periods are indicated at the top: day (2019-07-25 12:00 to 20:50 CEST and 2019-07-26 08:10 to 14:00 CEST), night (2019-07-25 21:00 to 2019-07-26 05:50 CEST), and morning transition (MT) (2019-07-26 06:00 to 08:00 CEST). The dotted vertical lines indicate the time of the sign change for the respective data type.

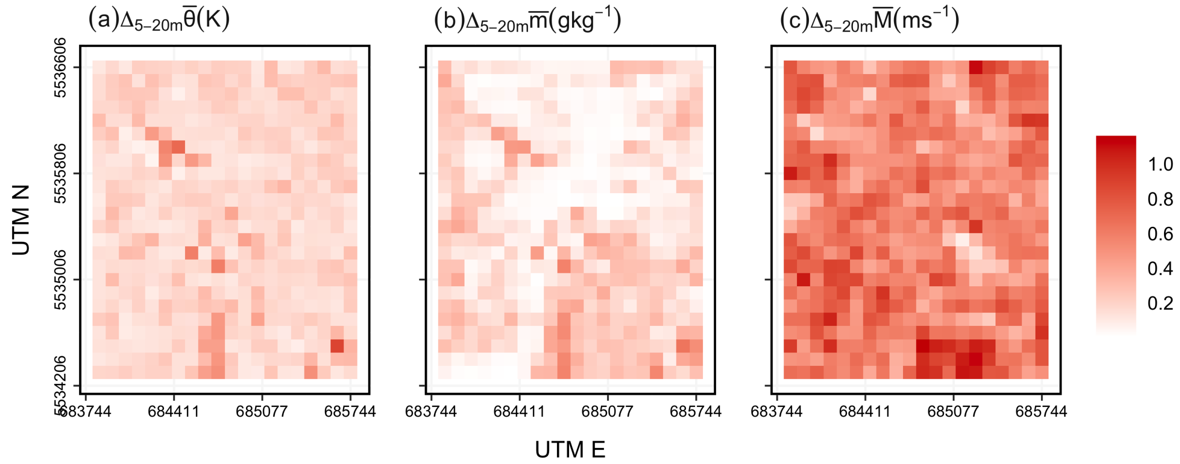

Figure A.3: Horizontal cross section of the first grid level above the surface, i.e., the first 100 % fluid grid cell, covering the study area in a 100 x 100 m spatial resolution. Each grid cell shows the temporally averaged absolute spatial resolution differences of (a) potential temperature in K ($\Delta_{5-20m}\ \overline{\theta}$), (b) water vapor mixing ratio in g kg^{-1} ($\Delta_{5-20m}\ \overline{m}$), and (c) wind speed in m s^{-1} ($\Delta_{5-20m}\ \overline{M}$). The color scale applies to all three plots in their respective units.

Table A.1: This table gives an overview of the maximum (max), minimum (min), and mean values of the observed and modeled data sets for both spatial resolutions (5 m and 20 m). The table shows the data separated for the three different measurement stations Birken, Markt, and Mistel and the three distinct time periods day, night and morning transition (MT), and for the three meteorological elements air temperature, specific humdidity, and wind speed. The whole data sets are displayed graphically in Figures 15, 16, and 17.

			observed			modeled 20 m			modeled 5 m		
			max	min	mean	max	min	mean	max	min	mean
air temperature	day	Birken	36.7	23.3	33.2	36.4	23.5	32.6	36.1	23.7	32.7
		Markt	37.7	24.4	34.3	37.0	22.9	33.0	36.3	22.7	32.8
		Mistel	36.9	23.1	33.4	36.4	23.4	32.6	36.0	23.2	32.4
	night	Birken	31.5	18.4	23.1	32.5	24.3	28.3	32.4	24.0	28.1
		Markt	32.8	19.8	25.1	32.8	24.1	28.8	32.5	23.9	28.7
		Mistel	31.4	16.2	21.2	32.6	24.3	28.6	32.3	23.0	27.9
	MT	Birken	22.7	18.3	19.8	23.8	23.5	23.7	23.7	23.3	23.5
		Markt	23.5	19.8	20.9	24.3	22.9	23.8	24.7	22.8	24.0
		Mistel	22.2	16.4	18.5	24.2	23.4	23.7	23.6	22.6	22.9
specific humidity	day	Birken	9.0	5.5	7.4	8.2	5.8	6.9	9.1	6.2	7.3
		Markt	9.9	6.0	8.0	8.1	5.6	6.8	8.1	5.6	6.8
		Mistel	10.0	5.7	7.7	8.2	5.6	7.0	9.1	5.9	7.4
	night	Birken	8.5	6.8	7.9	7.3	5.8	6.6	7.3	5.9	6.7
		Markt	8.9	7.0	8.3	7.4	5.9	6.7	7.3	5.8	6.7
		Mistel	8.6	6.6	8.2	7.4	6.0	6.7	7.5	6.1	6.8
	MT	Birken	9.0	8.3	8.6	7.2	6.3	6.6	7.6	6.4	6.9
		Markt	9.4	8.7	9.0	7.8	6.4	6.9	7.9	6.4	6.9
		Mistel	10.0	8.6	9.2	7.4	6.3	6.8	7.8	6.4	7.1
wind speed	day	Birken	1.8	0.2	0.9	4.7	0.4	2.0	2.1	0.2	0.8
		Markt	1.2	0.2	0.7	1.8	0.3	0.9	1.6	0.3	0.9
		Mistel	1.4	0.3	0.8	4.5	0.1	1.7	3.1	0.2	1.3
	night	Birken	0.4	0.1	0.3	3.4	0.5	1.6	1.3	0.1	0.4
		Markt	0.7	0.1	0.2	2.2	0.3	0.9	1.4	0.4	0.8
		Mistel	0.5	0.2	0.3	3.3	0.2	1.3	2.4	0.2	1.1
	MT	Birken	0.3	0.2	0.3	1.0	0.2	0.6	0.4	0.1	0.2
		Markt	0.4	0.1	0.2	0.8	0.2	0.4	1.0	0.3	0.6
		Mistel	0.6	0.2	0.4	1.1	0.2	0.5	0.9	0.2	0.5

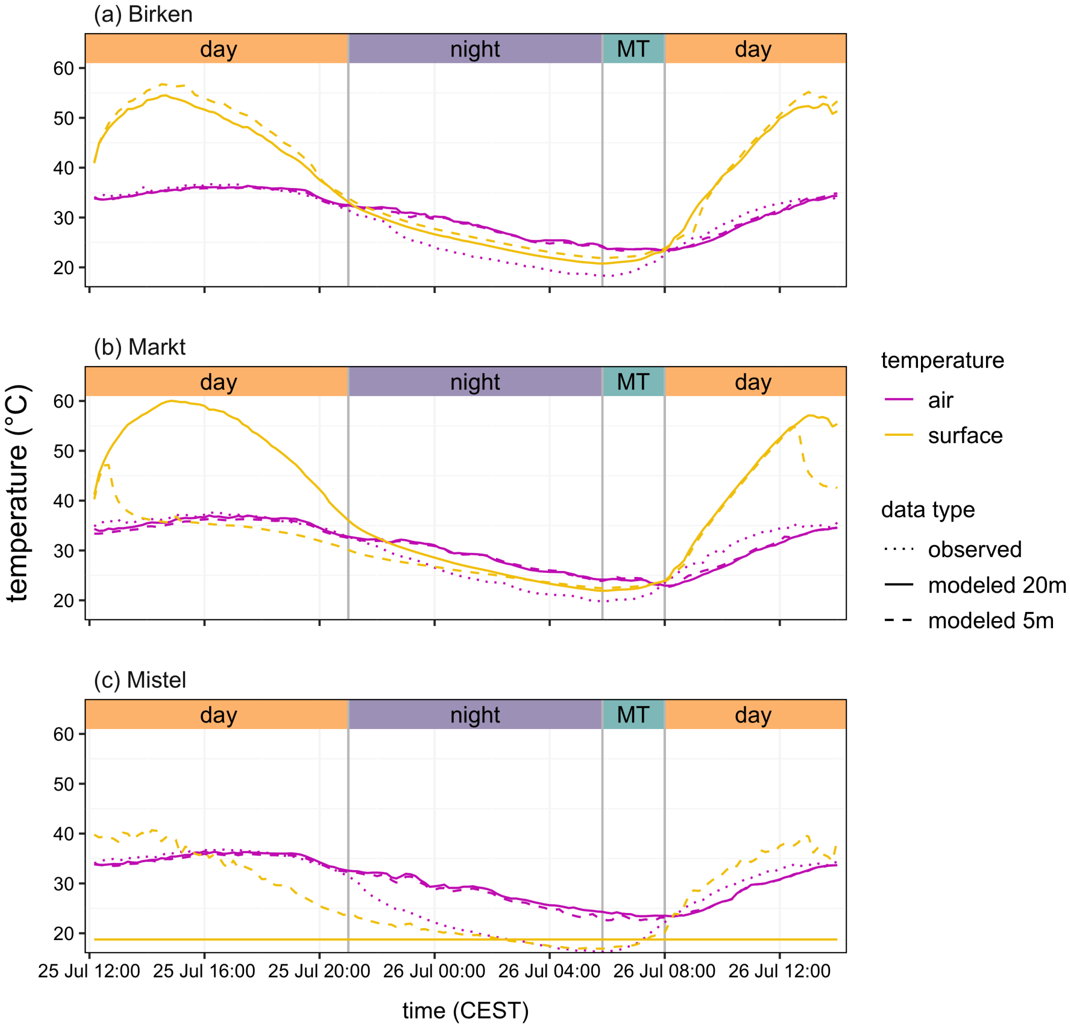

Figure A.4: Time series of air temperature (pink lines) and surface temperature (yellow lines) (℃) at the measurement stations (a) Birken, (b) Markt, and (c) Mistel. Lines of observed values are dotted, lines of modeled values at the 20 m spatial resolution are solid, and lines of modeled values at the 5 m spatial resolution are dashed. The three time periods are indicated at the top: day (2019-07-25 12:00 to 20:50 CEST and 2019-07-26 08:10 to 14:00 CEST), night (2019-07-25 21:00 to 2019-07-26 05:50 CEST), and morning transition (MT) (2019-07-26 06:00 to 08:00 CEST).

A.2 Thermal diffusivity calculations

The thermal diffusivity a ($10^{-6}\,\mathrm{m^2\,s^{-1}}$) for Table 4 was calculated as the thermal conductivity k ($\mathrm{W\,m^{-1}\,K^{-1}}$) divided by the heat capacity C ($10^6\,\mathrm{J\,m^{-3}\,K^{-1}}$) (Eq. 4). For the pavement and water surface cover, k ($\mathrm{W\,m^{-1}\,K^{-1}}$) and C ($10^6\,\mathrm{J\,m^{-3}\,K^{-1}}$) are directly defined in the PALM-4U source code i.e., (PALM LSP, 2023). At vegetated surface covers, a vegetation skin layer lies on top of the uppermost soil level. In this case, k ($\mathrm{W\,m^{-1}\,K^{-1}}$) was calculated as follows:

$$k = \frac{k_{skin} \cdot k_{soil}}{k_{skin} + k_{soil}} \quad (\mathrm{W\,m^{-1}\,K^{-1}}), \tag{A.1}$$

where k_{skin} ($\mathrm{W\,m^{-1}\,K^{-1}}$) is the thermal conductivity of the skin layer and k_{soil} ($\mathrm{W\,m^{-1}\,K^{-1}}$) is the thermal conductivity of the uppermost soil layer. While k_{soil} ($\mathrm{W\,m^{-1}\,K^{-1}}$) was defined in the source code, k_{skin} ($\mathrm{W\,m^{-1}\,K^{-1}}$) was calculated with

$$k_{skin} = k_s \cdot 0.5dz_1 \quad (\mathrm{W\,m^{-1}\,K^{-1}}). \tag{A.2}$$

The thermal conductivity between the atmosphere and the soil k_s ($\mathrm{W\,m^{-1}\,K^{-1}}$) is multiplied with half the thickness of the topsoil layer dz_1 (m).

Declaration of authorship

Hereby, I declare that I have authored the master thesis titled

"Simulating an extreme heat event in a mid-sized city in Europe with Large Eddy Simulation: investigating the impact of spatial resolution and validation with an observation network"

independently based on my own work. All direct or indirect sources used are acknowledged as references. This thesis has not been published or previously submitted to any other examination board. This work does not claim to be complete.

Bayreuth, March 31, 2023

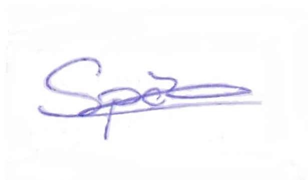

Eva Späte